

ANL-76-41

ANL-76-41

**PLEASE RETURN TO
MFC BRANCH LIBRARY**

INL Technical Library



403125

AN EXPERIMENTAL AND ANALYTICAL STUDY OF THE SPUTTERING PHENOMENA

by

Paul A. Howard

BASE TECHNOLOGY



U of C-AUA-USERDA

ARGONNE NATIONAL LABORATORY, ARGONNE, ILLINOIS

**Prepared for the U. S. ENERGY RESEARCH
AND DEVELOPMENT ADMINISTRATION
under Contract W-31-109-Eng-38**

The facilities of Argonne National Laboratory are owned by the United States Government. Under the terms of a contract (W-31-109-Eng-38) between the U. S. Energy Research and Development Administration, Argonne Universities Association and The University of Chicago, the University employs the staff and operates the Laboratory in accordance with policies and programs formulated, approved and reviewed by the Association.

MEMBERS OF ARGONNE UNIVERSITIES ASSOCIATION

The University of Arizona	Kansas State University	The Ohio State University
Carnegie-Mellon University	The University of Kansas	Ohio University
Case Western Reserve University	Loyola University	The Pennsylvania State University
The University of Chicago	Marquette University	Purdue University
University of Cincinnati	Michigan State University	Saint Louis University
Illinois Institute of Technology	The University of Michigan	Southern Illinois University
University of Illinois	University of Minnesota	The University of Texas at Austin
Indiana University	University of Missouri	Washington University
Iowa State University	Northwestern University	Wayne State University
The University of Iowa	University of Notre Dame	The University of Wisconsin

NOTICE

This report was prepared as an account of work sponsored by the United States Government. Neither the United States nor the United States Energy Research and Development Administration, nor any of their employees, nor any of their contractors, subcontractors, or their employees, makes any warranty, express or implied, or assumes any legal liability or responsibility for the accuracy, completeness or usefulness of any information, apparatus, product or process disclosed, or represents that its use would not infringe privately-owned rights. Mention of commercial products, their manufacturers, or their suppliers in this publication does not imply or connote approval or disapproval of the product by Argonne National Laboratory or the U. S. Energy Research and Development Administration.

Printed in the United States of America
Available from
National Technical Information Service
U. S. Department of Commerce
5285 Port Royal Road
Springfield, Virginia 22161
Price: Printed Copy \$5.00; Microfiche \$2.25

ANL-76-41

ARGONNE NATIONAL LABORATORY
9700 South Cass Avenue
Argonne, Illinois 60439

AN EXPERIMENTAL AND ANALYTICAL STUDY
OF THE SPUTTERING PHENOMENA

by

Paul A. Howard

Reactor Analysis and Safety Division

March 1976

Based on a dissertation submitted to the
Faculty of the Graduate School,
Marquette University, Milwaukee, Wisconsin,
in partial fulfillment of the requirements
for the degree of
Doctor of Philosophy

TABLE OF CONTENTS

	<u>Page</u>
NOMENCLATURE	8
ABSTRACT	9
I. INTRODUCTION	10
II. LITERATURE.	15
III. EXPERIMENT	22
A. Experiment Apparatus.	22
B. Test Section and Heater Assembly.	23
C. Measurements of Surface Temperature	23
D. Sputtered Water Temperature.	27
E. Water Temperature and Condensation Heat Flux	27
F. Measurements of Water Flow Rate	27
G. Experimental Procedure	29
IV. MATHEMATICAL MODEL OF SPUTTERING	31
A. One-dimensional Energy Equation of the Liquid.	31
B. One-dimensional Energy Equation of the Rod.	32
C. Two-dimensional Analysis of the Rod.	33
V. SPUTTERING PHENOMENA	35
A. Falling-film Heat Transfer	36
B. Incipient Boiling.	38
C. Region 2--Nucleate Boiling	39
D. Approach to CHF	43
E. The Critical Heat Flux	44
F. Sample Calculation.	46
VI. EXPERIMENTAL DATA AND COMPARISON WITH ANALYSIS. . .	49
A. Sputtering-front Temperature.	49
B. Comparison of Experimental Data and Calculations	51

TABLE OF CONTENTS

	<u>Page</u>
C. Sensitivity Studies	63
D. Simplified Analysis.	64
E. Analysis of a Moving Sputtering Front	68
VII. CONCLUSIONS	73
APPENDIXES	
A. Relation between a Stationary Sputtering Front and a Moving Sputtering Front	74
B. Stationary-sputtering-front Data	77
C. Estimate of Contact Temperature Error	79
D. Estimate of the Condensation Heat Flux.	80
E. Numerical Methods	81
F. Statistical Definitions and Methods	85
1. Linear Least-squares Regression Line.	85
2. Standard Error of Estimate	85
3. Coefficient of Correlation.	86
G. Two-dimensional Analysis of a Moving Sputtering Front.	89
ACKNOWLEDGMENTS	95
REFERENCES.	96

LIST OF FIGURES

<u>No.</u>	<u>Title</u>	<u>Page</u>
1.	Illustration of a Moving Sputtering Front and Associated Temperature Profiles.	10
2.	Normal Pool-boiling Curve and the Leidenfrost Phenomena.	12
3.	Modes of Film Breakdown.	14
4.	Comparison of Sputtering Models for Water	18
5.	Test Section, Shields, and Heater	24
6.	Assembled Test Section	24
7.	Cross-sectional View of Test Section and Shields	25
8.	Thermocouple Probe and Mixing Cup.	25
9.	Interior of Hood.	26
10.	Test Facility.	28
11.	Effect of Photoflo-200 on Surface Tension	29
12.	One-dimensional Model of Sputtering.	31
13.	Two-dimensional Model of Sputtering	34
14.	Three Heat-transfer Regions	35
15.	Falling-film Heat Transfer for Water at 100°F	37
16.	Falling-film Heat Transfer for Water at 150°F	37
17.	Superposition and Bubble Nucleation	39
18.	Pool-boiling Correlations	40
19.	Subcooled Forced-convection Boiling Heat Flux up to CHF	46
20.	Least-squares Correlation for Runs 7A and 7B.	49
21.	Comparison of Measured Sputtering-front Temperatures and Jens-Lottes Correlation	51
22.	Range of Experimental Data.	52
23.	Calculated and Measured Temperature Profiles for Run 3.	52
24.	Calculated and Measured Temperature Profiles for Run 5.	53
25.	Calculated and Measured Temperature Profiles for Run 6.	53
26.	Calculated and Measured Temperature Profiles for Run 10.	54
27.	Calculated and Measured Temperature Profiles for Run 11.	54
28.	Two-dimensional Temperature Profiles for Run 3.	55

LIST OF FIGURES

<u>No.</u>	<u>Title</u>	<u>Page</u>
29.	Two-dimensional Temperature Profiles for Run 5	55
30.	Two-dimensional Temperature Profiles for Run 6	56
31.	Two-dimensional Temperature Profiles for Run 10	56
32.	Two-dimensional Temperature Profiles for Run 11	57
33.	Two-dimensional Temperature Gradients for Run 3	57
34.	Two-dimensional Temperature Gradients for Run 5	58
35.	Two-dimensional Temperature Gradients for Run 6	58
36.	Two-dimensional Temperature Gradients for Run 10	59
37.	Two-dimensional Temperature Gradients for Run 11	59
38.	Heat-transfer Coefficient as a Function of Surface Temperature for Run 3	60
39.	Heat-transfer Coefficient as a Function of Surface Temperature for Run 5	60
40.	Heat-transfer Coefficient as a Function of Surface Temperature for Run 6	61
41.	Heat-transfer Coefficient as a Function of Surface Temperature for Run 10	61
42.	Heat-transfer Coefficient as a Function of Surface Temperature for Run 11	61
43.	Calculated and Measured Temperature Gradients	63
44.	Model Sensitivity to Pool-boiling Correlation	64
45.	Model Sensitivity to Breakpoint	64
46.	Average Heat-transfer Coefficient as a Function of Flow Rate and Subcooling.	67
47.	Variation of Sputtering Temperature with Flow Rate and Subcooling	68
48.	Comparison of One-dimensional Analysis, Two-dimensional Analysis, and Data.	68
49.	Calculated Results of Two-dimensional Moving-sputtering- front Analysis.	71
50.	Measured and Calculated Rewetting Velocity.	71

LIST OF FIGURES

<u>No.</u>	<u>Title</u>	<u>Page</u>
C.1.	Thermocouple Response.	79
E.1.	Two-dimensional Temperature Grid.	84
F.1.	Statistical Methods	86
G.1.	Two-dimensional Analytic System	89

LIST OF TABLES

<u>No.</u>	<u>Title</u>	<u>Page</u>
I.	Comparison of Experimental and Calculated Sputtering Temperatures	50
II.	Comparison of Measured and Calculated Dry-zone Temperature Gradients.	62
III.	Calculated and Experimentally Measured Dimensionless Rewetting Velocities.	72

NOMENCLATURE

A	area	ft ²	x	quality	dimensionless
Bi	Biot number, $h_c \delta / k$	dimensionless	y	direction normal to surface	ft
C	arbitrary constant	dimensionless	z	axial direction	ft
c	specific heat	Btu/lb _m -°F	α	thermal diffusivity	ft ² /hr
CHF	critical heat flux	Btu/hr-ft ²	β	coefficient of thermal expansion	°F ⁻¹
D	diameter	ft	β_L	dimensionless coefficient	[Eq. 33]
\dot{E}	time rate of change of energy	Btu/hr	Γ	mass flow rate per unit wetted periphery	lb _m /hr-ft
G	mass flux ($G = \rho u$)	lb _m /hr-ft ²	δ	liquid-film thickness	ft
g	gravitational acceleration	32.2 ft/sec ²	ϵ	tube or cladding thickness	ft
g_c	conversion factor	32.2 lb _m -ft/sec ² -lb _f	ζ	dimensionless axial distance	
h_c	local heat-transfer coefficient	Btu/hr-ft ² -°F	η	dimensionless radial distance	
\bar{h}_c	average heat-transfer coefficient	Btu/hr-ft ² -°F	μ	viscosity	lb _m /hr-ft
h_{fg}	latent heat of vaporization	Btu/lb _m	ρ	density	lb _m /ft ³
k	thermal conductivity	Btu/hr-ft-°F	σ	surface tension	dynes/cm
l	length	ft	τ	dimensionless temperature	
\dot{m}	mass flow rate	lb _m /hr	τ_0	dimensionless surface temperature	
N	number of data points		τ_0^*	dimensionless sputtering temperature	
n	constant		φ	heat flux	
Nu	Nusselt number $h_c \delta / k$	dimensionless	<u>Subscripts</u>		
Pr	Prandtl number $c \mu / k$	dimensionless	b	boiling	mea measured
\dot{Q}_{total}	total heat-removal rate of a sputtering front	Btu/hr	bi	incipient boiling	out outer
Q^+	defined in Eq. G.2	dimensionless	con	condensation	pb pool boiling
Q^-	defined in Eq. G.3	dimensionless	eff	effective	rod rod
r	correlation coefficient		est	estimated	sat saturation
Re	Reynolds number $4 \rho u \delta / \mu$	dimensionless	fc	forced convection	sf surface fluid
ΔT_x	excess temperature ($T_{sur} - T_{sat}$)	°F	i	interface	sput sputtering
T_∞	initial tube temperature	°F	in	inner	sub subcooling
ΔT_{liq}	liquid temperature change	°F	incip	incipient	sur surface
u	velocity	ft/hr	liq	liquid	t tube
\bar{u}_{liq}	average liquid velocity	ft/hr			

AN EXPERIMENTAL AND ANALYTICAL STUDY OF THE SPUTTERING PHENOMENA

by

Paul A. Howard

ABSTRACT

One form of the sputtering phenomena, the heat-transfer process that occurs when an initially hot vertical surface is cooled by a falling liquid film, was examined from a new experimental approach. The sputtering front is the lowest wetted position on the vertical surface and is characterized by a short region of intense nucleate boiling. The sputtering front progresses downward at nearly a constant rate, the surface below the sputtering front being dry and almost adiabatic. This heat-transfer process is of interest in the analysis of some of the performance aspects of emergency core-cooling systems of light-water reactors.

An experimental apparatus was constructed to examine the heat-transfer characteristics of a sputtering front. In the present study, a heat source of sufficient intensity was located immediately below the sputtering front, which prevented its downward progress, thus permitting detailed measurements of steady-state surface temperatures throughout a sputtering front. Experimental evidence showed the sputtering front to correspond to a critical heat-flux (CHF) phenomenon. Data were obtained with water flow rates of 350-1600 lb_m/hr-ft and subcoolings of 40-140°F on a 3/8-in. solid copper rod at 1 atm.

A two-dimensional analytical model was developed to describe a stationary sputtering front where the wet-dry interface corresponds to a CHF phenomena and the dry zone is adiabatic. This model is nonlinear because of the temperature dependence of the heat-transfer coefficient in the wetted region and has yielded good agreement with data. A simplified one-dimensional approximation was developed which adequately describes these data. Finally, by means of a coordinate transformation and additional simplifying assumptions, this analysis was extended to analyze moving sputtering fronts, and reasonably good agreement with reported data was shown.

I. INTRODUCTION

A radioactive release following a nuclear accident during the normal operation of a Light Water Reactor (LWR) can only happen when the energy production exceeds the energy-removal rate, for which there are only two possibilities: an excursion (a nuclear power transient) or a Loss-of-coolant Accident (LOCA).⁷⁵ Since the successful operation of the Emergency Core Cooling System (ECCS) after a LOCA would prevent any radioactive release, it is the adequacy of these systems upon which much of the controversy is focused. The phenomena of sputtering, a heat-transfer process which has not yet been fully identified, will occur during the operation of the ECCS.^{17,71} Elaborate quantitative studies have been conducted during the operation of simulated ECCS's,^{10,20,21,29,57,80,81} but because of the confined geometry the nature of the sputtering process has not yet been understood. In this first chapter, the heat-transfer characteristics of sputtering will be related to other boiling processes. Then the hydraulic aspects of sputtering will be related to three other processes of dry-patch formation. With the perspective of this background information, this chapter will be concluded with the purpose and approach of this study.

The phenomenon of sputtering occurs when a falling liquid film is used to cool a surface which is initially much hotter than the saturation temperature of the liquid. Figure 1 illustrates this process on a vertical tube. The intense boiling which takes place at the sputtering front lifts the water film from the

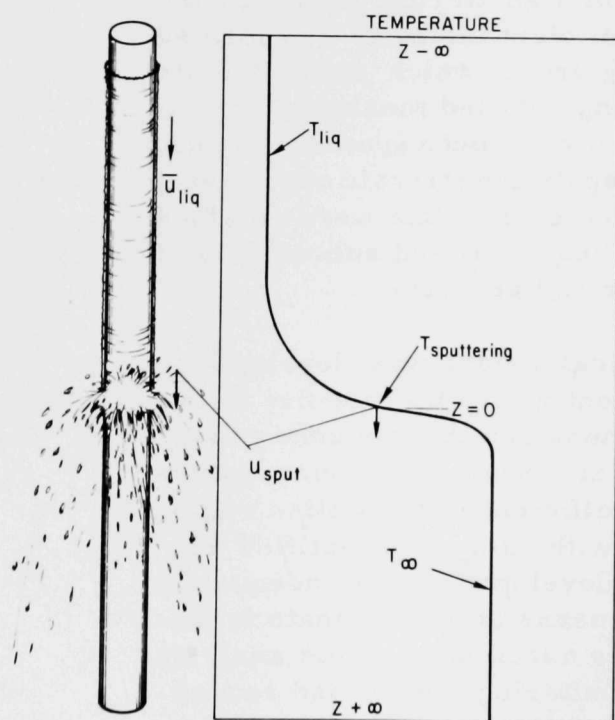


Fig. 1. Illustration of a Moving Sputtering Front and Associated Temperature Profiles.
ANL Neg. No. 900-75-861.

surface. Once the cooling water film has been pushed from the surface, it does not return because the only force acting on it is gravity. In a vertical orientation, the sputtering-front velocity is less by an order of magnitude than the average liquid velocity in the falling film above the front. Falling liquid-film velocities range from 3000 to 15,000 ft/hr (1000-5000 m/hr), whereas sputtering-front velocities have been reported from 30 to 3000 ft/hr (10-1000 m/hr). The velocity at which a front progresses downward has been shown experimentally to be proportional to the water subcooling and inversely proportional to the initial temperature of the surface.⁶¹ However, conflicting data on the effect of coolant flow rate has been reported.^{5,20}

Consider a sputtering front moving down a vertical tube as shown in Fig. 1. Assume the tube was initially

isothermal and that the water temperature and flow rate are constant during the rewetting. To transform this unsteady heat-transfer problem to one of steady state, let the coordinate system move with the sputtering front. The tube temperature near the sputtering front is shown qualitatively in Fig. 1, where the origin is at the sputtering front and the positive z direction is down. Let the sputtering front be defined as the lowest wetted position on the surface, and let the sputtering temperature be the surface temperature at this wet-dry interface. Above the sputtering front energy is transferred to the liquid by convection as the tube temperature decreases from T_{sput} to T_{liq} . In the coordinate system moving with the sputtering front, this same energy can be viewed as the sum of two components:

1. The thermal energy removed in cooling the tube from T_{sput} to T_{liq} .
2. The thermal energy conducted upward in the rod by the temperature gradient immediately below the front in the dry zone.

Any cooling of the rod below the sputtering front is by radiation or convection to the surroundings. In some practical cases, this heat flux can be significant. However, much can be learned from experiments and analysis where this heat flux is small and can be neglected:

$$\int_0^{\infty} h_c \pi D_t (T_t - T_{\text{surroundings}}) dz \approx 0. \quad (1)$$

Since the net effect of rewetting is the cooling of the tube from T_{∞} to T_{liq} , a simple energy balance can relate the rewetting velocity to the total heat-removal capacity of the rewetting liquid:

$$u_{\text{sput}} = \frac{\dot{Q}_{\text{total}}}{\rho_t c_t \pi D_t \epsilon (T_{\infty} - T_{\text{liq}})}, \quad (2)$$

where \dot{Q}_{total} is the heat flux integrated over the wetted surface:

$$\dot{Q}_{\text{total}} = \int_{-\infty}^0 h_c \pi D_t (T_t - T_{\text{liq}}) dz. \quad (3)$$

This is also equal to the rates of energy increase of the water and steam released from the falling liquid film:⁵³

$$\dot{Q}_{\text{total}} = \dot{m}(1 - x)c_{\text{liq}}\Delta T_{\text{liq}} + \dot{m}x(h_{\text{fg}} + c_{\text{liq}}\Delta T_{\text{sub}}). \quad (4)$$

Since sputtering is a boiling heat-transfer process, let us consider a typical pool-boiling curve (see upper half of Fig. 2) and relate sputtering to other boiling phenomena. Pool boiling is a process where a heated surface is totally submerged in a stagnant body of liquid. If the liquid temperature is less

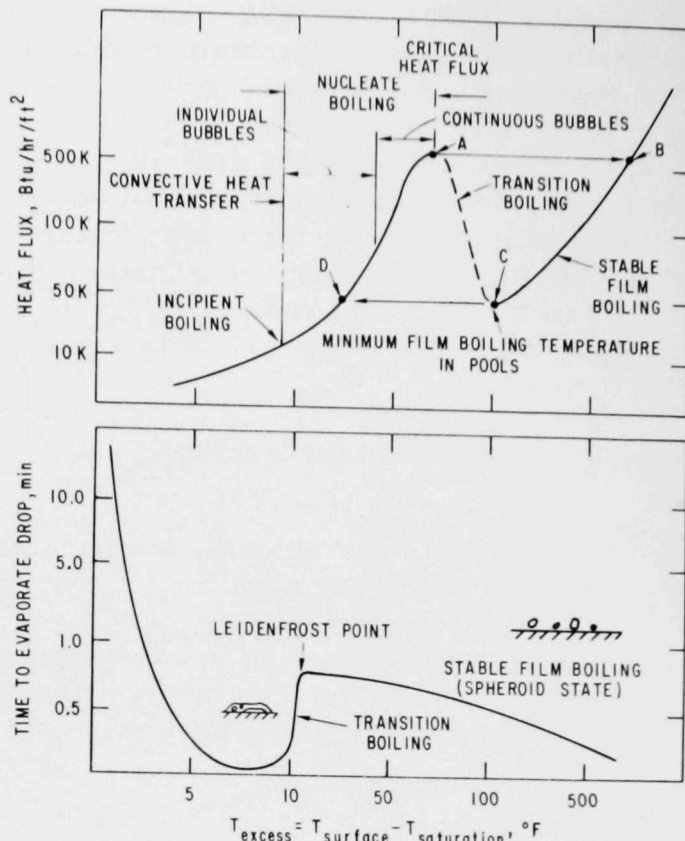


Fig. 2. Normal Pool-boiling Curve and the Leidenfrost Phenomena. ANL Neg. No. 900-75-862.

Heat Flux (CHF) or Departure from Nucleate Boiling (DNB) will be used here. If the heated surface is heat-flux controlled, such as a electrically heated rod or reactor fuel rod, and if the flux were increased to a value above the CHF, the temperature would quickly rise to the point B which might be above the melting point. This is the reason why point A is sometimes called the burn-out point. A heat flux greater than this might result in the melting or "burnout" of the heater.

If the surface were temperature-controlled, such as a surface heated by another liquid, the heat flux would follow the path from point A to point C. In the region A to C, which is known as transition boiling, the fraction of the surface which is wetted by the liquid decreases, thus decreasing the average heat-transfer coefficient and the heat flux. At point C, the minimum surface temperature for stable film boiling, the surface is not wetted by the liquid. Heat is transferred by conduction and radiation through the vapor blanket between the liquid and the surface. Point C is sometimes confused with the Leidenfrost temperature, which applies to individual drops of liquid on a heated surface. During stable film boiling on a heat-flux-controlled surface, if the heat flux were reduced to a value slightly less than the amount at point C, the surface temperature would quickly change to the value at point D and the film-boiling regime would change to nucleate boiling.³²

than the saturation temperature, the process is subcooled pool boiling, while if the temperature is equal to the saturation temperature, the process is saturated pool boiling. When the heated surface temperature is slightly higher than the liquid temperature, thermal energy is transferred to the liquid at a rate which is proportional to the temperature difference. Increasing the surface temperature will eventually cause bubbles to nucleate at the surface; this is known as incipient boiling. Heat transfer is enhanced by the movement of these bubbles at the surface and the heat flux begins to increase sharply. Increasing the surface temperature increases the rate of bubble nucleation and the number of nucleation sites. The first critical point on the boiling curve is reached at point A, which is described by many names all of which have a slightly different meaning.³³ The terms Critical

The lower half of Fig. 2 shows how the Leidenfrost temperature is defined for spherical drops of liquid on a horizontal heated surface.² It is the minimum temperature needed to prevent the wetting of the heated surface by the liquid. Vapor produced at the bottom of the drop forms a thin vapor blanket beneath the drop, thus supporting it. For carefully controlled conditions, the minimum surface temperature has been found to be slightly above the saturation temperature.¹ For larger amounts of liquid covering a heated surface (film boiling of puddles), the minimum surface temperature has been found to be a function of the thermal properties of the heated surface and liquid.³² In this situation, there is intermittent wetting and, hence, the formation of short-lived cold spots. If the surface cannot recover from the wetting before it is contacted again by the liquid, the cold spot will grow; eventually the heated surface will cool and become entirely wetted. As a consequence of these hydraulic differences, the minimum temperature for stable film boiling is different for these different situations. For water at atmospheric pressure, the minimum temperature for stable film boiling of a pool is about 160°F greater than saturation and can be considerably higher if the heated surface is a poor thermal conductor. This contrasts to the Leidenfrost temperature, which has a lower limit of the saturation temperature.

For a confined geometry, the sputtering process has been considered to be the opposite of the dryout process.²⁶ In dryout, the wetted surface area is reduced instead of increased as in sputtering. The transition region is included in the dryout process; if the two processes were truly opposite, the same boiling phenomena would occur in the sputtering zone. In order to determine the actual physical processes at the sputtering front, the sputtering-front temperature must be known. Present estimates of the sputtering temperature cover the range from the CHF temperature to the stable film-boiling temperature. Analytical models of the sputtering-front velocity predict that the front moves downward as fast as the surface temperature is reduced to a low enough temperature to allow rewetting. The surface temperature ahead of the sputtering front is reduced by axial conduction from the dry region to the wetted region. Therefore, an accurate prediction of the rewetting velocity requires that the heat flux in the wetted zone be known.

Sputtering can be characterized as the disruption of a falling liquid film by intense boiling at the leading edge. There are other processes whereby a falling liquid film can be disrupted by a combination of geometry and/or heat transfer. Consider the following processes, shown schematically in Fig. 3. Progressive evaporation is the complete evaporation of a falling liquid film as a result of heat transfer from the tube to the liquid. This typically occurs when the water is nearly saturated, the flow rate is low, and the heat flux from the tube is low. Another mode of film breakdown is dry-patch formation, which occurs when a highly subcooled liquid film at a low flow rate flows down a heated tube. If a hot spot in the heated surface should develop, for example from an irregularity in the heated tube, the water temperature flowing over that hot spot would increase. At a point diametrically opposite it,

the water would be cooler; because surface tension is higher for colder water, the surface tension in the cold region would pull the water away from the hot spot. This skewing of the water flow away from the hot spot would eventually

cause the hot spot to dry up. The third mode of film breakdown, already described, is sputtering. The last mode is flooding, which can occur only in a confined geometry. In this countercurrent flow system, the falling liquid film is stripped from the walls by the high-velocity ($\approx 100,000$ ft/hr or $30,000$ m/hr) upward-moving vapor. This is an extremely difficult situation to analyze if the vapor were produced by evaporation of the falling liquid film. An oscillating behavior would result because the flooding would interrupt the falling liquid film; hence vapor production would cease, which, in turn, would stop the flooding, and so on. The vapor velocity required to strip the liquid from the walls is known as the flooding velocity and decreases with increasing liquid-film thickness.²⁷

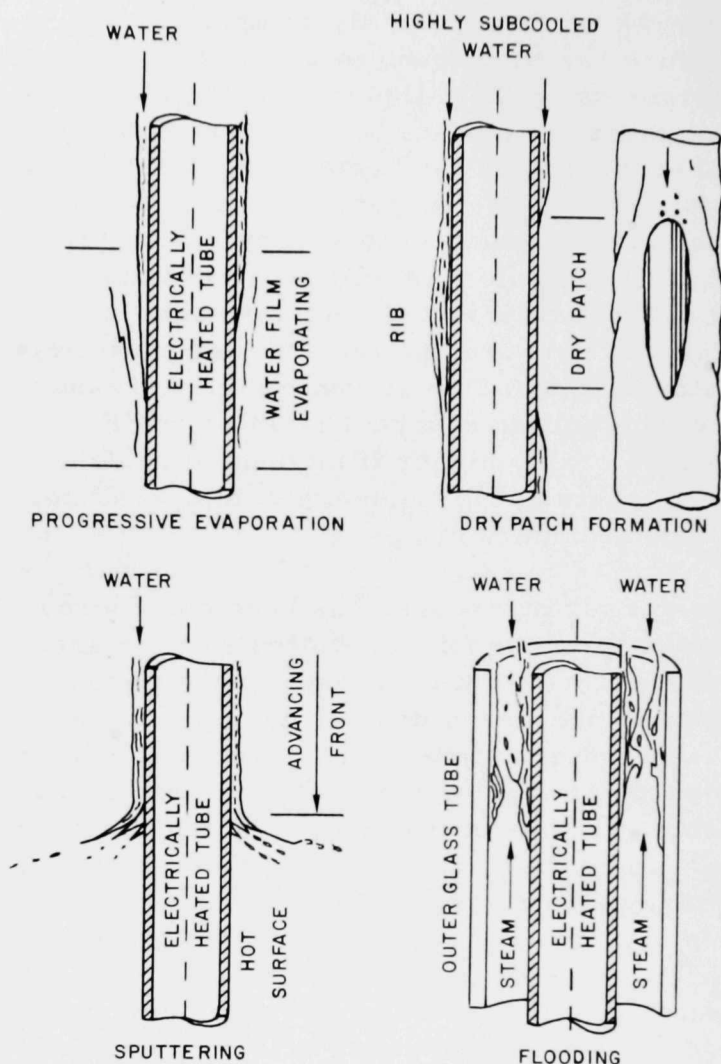


Fig. 3. Modes of Film Breakdown. ANL
Neg. No. 900-75-863.

evidence that the sputtering-front temperature corresponds to a CHF phenomena will be presented. The data were obtained by a series of unique experiments in which a sputtering front was held at a fixed location. (Appendix A shows how these stationary-sputtering-front data can be related to moving-sputtering-front data.) Experimental surface-temperature profiles through sputtering fronts for various flow conditions will be modeled with analysis developed here. An engineering approach to this problem will be taken; various heat-transfer correlations from the literature will be considered and the most applicable used in the modeling. Finally, by means of a suitable coordinate transformation, this model will be extended to describe reported moving-sputtering-front data.

II. LITERATURE

Sputtering is not a phenomenon that is associated exclusively with the cooling of reactor fuel rods after an LOCA. Continuous casting, quenching, and water curtains also involve sputtering. Therefore, the literature contains references to sputtering (but under the name of quenching) long before the advent of ECCSs. However, the data are of a gross qualitative nature and are not concerned with quenching itself, but with the results of quenching. From a metallurgical point of view, the property changes within the quenched metal were of more importance than the sputtering that brought these new properties about. In comparison, references to sputtering by the nuclear industry are concerned with the heat-transfer process at the sputtering front, where there is much ongoing work. It is for this reason that the literature cited here is from the latter source (up to 1974). Emphasis is placed on the identification of the sputtering phenomenon by previous investigators. It will be shown that a wide range of sputtering-front temperatures have been reported; hence, the heat-transfer mechanism (the location of sputtering on the boiling map, Fig. 2) at the sputtering front has yet to be determined.

In 1964, Shires⁶¹ conducted experimental sputtering tests on heated vertical surfaces. Water was used to cool an initially hot, Inconel tube at atmospheric pressure in both confined and unconfined geometries. Shires measured rewetting velocities from 112 to 1700 ft/hr (40-600 m/h) for water flow rates up to 3000 lb_m/hr-ft (4470 kg/hr-m). Data were recorded for single-pin and seven-pin heated assemblies for initial temperatures of 300-900°F (150-480°C). In addition to the four modes of film breakdown described in Ch. I, Shires observed the following trends with regard to sputtering:

1. Increasing the water flow rate increases the rewetting velocity.
2. Increasing the water subcooling increases the rewetting velocity.
3. Increasing the initial rod temperatures decreases the rewetting velocity.

An interesting approach was used by Shires to estimate the sputtering temperature. A series of tests was conducted for different initial rod temperatures but at a constant water temperature and flow rate. By extrapolating the data, an infinite rewetting velocity was calculated for an initial rod temperature of 280°F (140°C). Shires concluded that this is the sputtering temperature.

Yamanouchi^{80,81} considered the rewetting of a simulated reactor fuel subassembly where water was used to cool 36 electrically heated tubes in a confined geometry. Data⁸⁰ were reported showing the conditions when rewetting was not possible. These conditions were a combination of high electric power supplied to the tubes, low water subcooling and low water flow rates. Either progressive evaporation or flooding prevented the water from penetrating to the bottom of the heater assembly. The sputtering-front temperature was measured to be 300°F (150°C). Yamanouchi⁸¹ proposed a model for predicting the

sputtering-front velocity. Since this model has been widely used,^{15,16,29,57} the basic assumptions will be presented here.

1. The rewetting-front velocity is constant. This reduces the problem to steady state. (Bukur and Isbin have shown that the time required to reach a steady rewetting velocity for the Yamanouchi system is insignificant compared to the time to rewet the tubes.⁹)

2. Only axial conduction in the rod is significant, and the rewetting is axisymmetric.

3. The dry zone is adiabatic.

4. The heat-transfer coefficient in the wetted zone is a constant.

5. The water-film temperature is constant at T_{sat} .

6. The tube wall thickness is thin compared to the tube diameter so that a rectangular coordinate system is adequate.

An energy balance on an element of the tube yielded a linear second-order differential equation relating the temperature to axial position. This differential equation was solved in both the dry zone ($h_c = 0$) and the wetted zone ($\overline{h_c} = \text{constant}$). The solutions were joined at the sputtering front by requiring that the calculated temperature equal the sputtering temperature and that the temperature gradients at that interface be equal. (A similar approach is taken in Appendix A.) The sputtering velocity can be explicitly written as a function of the initial tube temperature, the saturation temperature of the water, the heat-transfer coefficient in the wetted zone, and the sputtering temperature:

$$u_{\text{sput}}^{-1} = \frac{\rho_t c_t}{2} \sqrt{\frac{\epsilon_t}{h_c k_t}} \sqrt{\left[\frac{2(T_\infty - T_{\text{sput}})}{T_{\text{sput}} - T_{\text{sat}}} + 1 \right]^2 - 1}. \quad (5)$$

If

$$\frac{T_\infty - T_{\text{sput}}}{T_{\text{sput}} - T_{\text{sat}}} \gg 1,$$

Equation 5 can be approximated as

$$u_{\text{sput}}^{-1} = \rho_t c_t \sqrt{\frac{\epsilon_t}{h_c k_t}} \frac{T_\infty - T_{\text{sput}}}{T_{\text{sput}} - T_{\text{sat}}}. \quad (6)$$

The magnitude of $\overline{h_c}$ was determined by measuring the rewetting rates on an unconfined vertical tube and solving Eq. 6 for $\overline{h_c}$. The sputtering temperature was considered to be 300°F (150°C), and the sputtering velocities were successfully correlated when the heat-transfer coefficient was assumed to vary with flow rate as

$$\overline{h_c} = 4288\sqrt{\Gamma}; \quad 150 \leq \Gamma \leq 2682.$$

This is a straightforward analysis and will be discussed again in Ch. VI; however, some additional comments are appropriate here. From Eq. 7, h_c ranges from 58,000 to 223,000 Btu/hr-ft²-°F (33 to 127 W/cm²-°C). These values seem high when compared to subcooled-forced-convection nucleate boiling, which leads to values that are typically 10,000 Btu/hr-ft²-°F (5.6 W/cm²-°C). It can be seen from Eq. 6 that decreasing \bar{h}_c decreases u_{sput} because u_{sput} varies with the square root of \bar{h}_c . Thus, by decreasing h_c by a factor of 10 to bring it into a range of more commonly observed values, the predicted rewetting velocity decreases by a factor of 3 below the measured values. (It will be shown in Ch. VI that a major cause of the underprediction of u_{sput} by a factor of 3 can be related to the accuracy of the estimates of the surface and effective liquid temperature at the sputtering front. By knowing these temperatures, one can determine the boiling mechanism and heat flux. Other investigators examined sputtering after Yamanouchi, and all had the same problem of guessing at the sputtering-front temperature. More sophisticated models have been proposed, but all are based on best estimates of sputtering-front conditions.)

Yoshioka^{82,83} examined sputtering on a vertical, stainless steel, unconfined, electrically heated test section. Rewetting velocities of 57-3000 ft-hr (20-1000 m/hr) for water flow rates of 500-5000 lb_m/hr/ft (750-7500 kg/hr-m) and water temperatures of 70-160°F (20-70°C) were measured. These data were obtained at atmospheric pressure, where initial test section temperatures ranged from 570 to 940°F (300-500°C). The test section was a tube of 0.51-in. (13-mm) outside diameter with a pair of thermocouples mounted on the outside, 3.9 in. (10 cm) apart, and a pair located opposite each other, one on the inside surface and one on the outside surface. One set was used to measure rewetting velocity and the other to detect two-dimensional effects at the sputtering front. The electric power supplied to the test section was interrupted during the sputtering event. Since the tube had a small thermal capacity, it began to cool immediately. At an initial temperature of 750°F (400°C), the tube cooled at a rate of 38°F/s (20°C/s). Since the rewetting velocity was measured over a 3.93-in. (10-cm) length, this meant a cooling of at least 45°F (25°C) of the tube surface before the front approached. Yoshioka reported the temperature at the sputtering front to be 374°F (190°C) and observed that only a thin layer of the falling liquid film took part in the boiling. Yoshioka concluded that increasing the water flow rate above the amount needed to form this thin layer has no effect on the rewetting velocity.

Yoskioka proposed a two-region, two-dimensional model for the rewetting phenomena. The dry zone was assumed to be adiabatic while the wetted zone had a constant heat-transfer coefficient. As with the Yamanouchi model, the front progressed downward as fast as the surface could be cooled to the sputtering temperature. One of the shortcomings of the Yoskioka model was the choice of boundary conditions at the sputtering front. At this location, the radial temperature gradient was assumed to be zero. This assumption greatly reduces the mathematical difficulties, but cannot be justified for the sputtering process.

A one-dimensional, three-region model of the sputtering phenomena was proposed by Sun et al.⁶³ The model is based on three distinctly observed regions:

1. A dry adiabatic region below the sputtering front.
2. A wetted region where intense boiling occurs.
3. A continuous falling liquid-film region above the sputtering front (see Fig. 4).

Each of the two regions in the wetted zone has a constant heat-transfer coefficient. The assumed value for the falling film region was 100 Btu/hr-ft²-°F (0.05 W/cm²-°C), and for the boiling region the value was 3000 Btu/hr-ft²-°F (1.7 W/cm²-°C). The boiling region is bounded by incipient boiling and stable film boiling; by referring to Fig. 2, one sees that this includes the entire nucleate-boiling and transition-boiling zones. The temperature at the wet-dry interface was assumed to be 500°F (260°C), which corresponds to stable film-boiling temperatures.

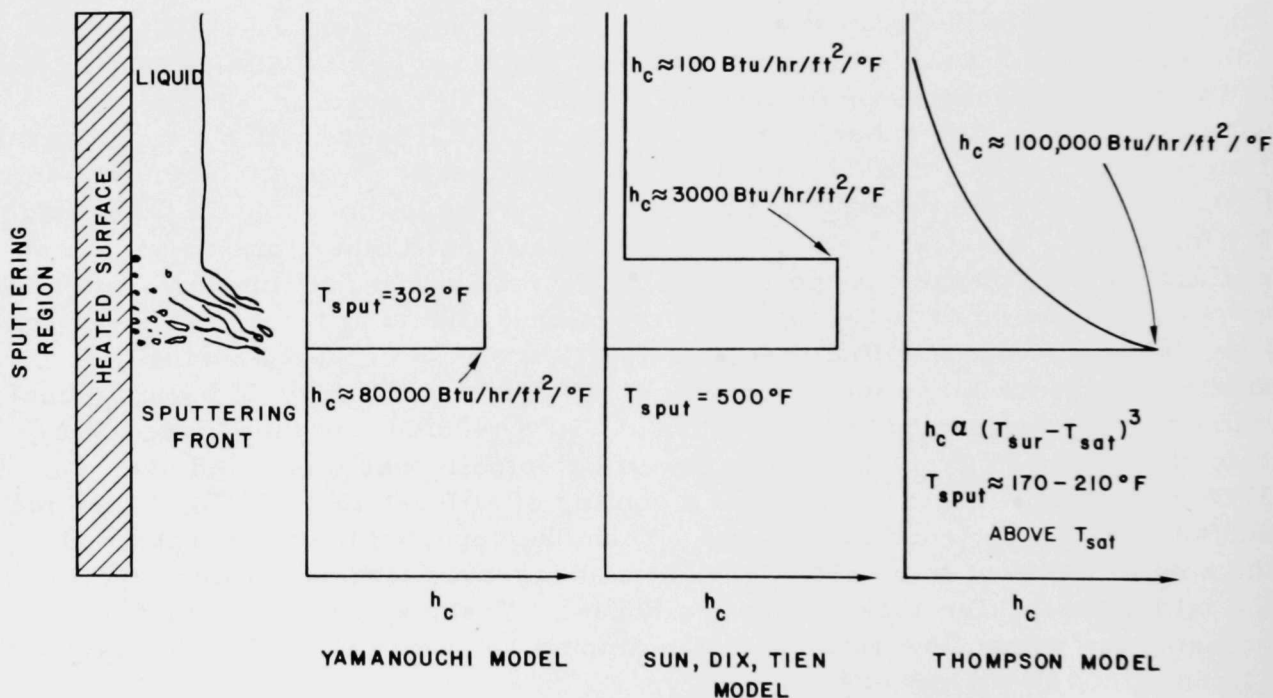


Fig. 4. Comparison of Sputtering Models for Water. ANL Neg. No. 900-75-864.

An experimental and analytical study of rewetting was conducted by Duffey and Porthouse.^{18,19} Experiments with electrically heated stainless steel test sections from 573 to 1472°F (300-800°C) showed rewetting phenomena to be identical for both falling films and bottom flooding. These tests were conducted at atmospheric pressure with water flow rates of 24-7250 lb_m/hr-ft (36-10,800 kg/hr-m). The axial length of the nucleate-boiling zone above the wet-dry interface was reported to be 0.198 in. (0.5 cm).

Two models of the sputtering process were proposed:

1. A two-region, one-dimensional model similar to the Yamanouchi model, valid for Biot numbers $h_c \epsilon_t / k_t < 1$.
2. A two-region, two-dimensional model for large Biot numbers, which reduces to the one-dimensional model as the Biot number becomes small.

Duffey and Porthouse used a macroscopic energy balance such as Eq. 2 as a boundary condition to find u_{sput} . This differs from the approach of Yamanouchi, who required a smoothly continuous temperature profile. The resulting one- and two-dimensional solutions are, respectively,

$$u_{\text{sput}}^{-1} = \rho_t c_t \sqrt{\frac{\epsilon_t}{h_c k_t}} \frac{(T_\infty - T_{\text{liq}})^{1/2} (T_\infty - T_{\text{sput}})^{1/2}}{T_{\text{sput}} - T_{\text{liq}}} \quad (8)$$

and

$$u_{\text{sput}}^{-1} = \frac{\pi \rho_t c_t}{2 h_c} \frac{T_\infty - T_{\text{liq}}}{T_{\text{sput}} - T_{\text{liq}}} \quad (9)$$

The authors were not sure if the proper liquid temperature at the sputtering front was the initial liquid temperature or the saturation temperature. If the initial liquid temperature was used, the suggested value for the sputtering temperature was 374°F (190°C); if the saturation temperature was used, $T_{\text{sput}} = 482^\circ\text{F}$ (250°C). It is found that in order for these models to predict measured rewetting velocities accurately, the heat-transfer coefficient must vary by a factor of 200; the range was 1760-352,000 Btu/hr-ft²-°F (1-200 W/cm²-°C).

Bennett⁵ obtained sputtering data with saturated water on a stainless steel test section at various pressures (100, 200, 300, 500, 1000 psia) (6.8, 13.6, 20.4, 34, 68 atm). The sputtering-front temperature was measured to be 170-208°F (95-115°C) above the saturation temperature. The rewetting rate was found to be inversely proportional to the initial temperature of the rod and independent of the water flow rate. The data of Bennett were analyzed by Thompson⁶⁴ with a two-region model (see Fig. 4). The wet-side heat-transfer coefficient was proportional to $(T_{\text{surface}} - T_{\text{sat}})^3$, while the dry region below the sputtering front was assumed to be adiabatic. This heat-transfer coefficient makes the rod energy equation nonlinear; hence Thompson used numerical methods to obtain a solution. Both one-dimensional and two-dimensional models were used with calculated heat-transfer coefficients up to 100,000 Btu/hr-ft² (56.7 W/cm²-°C) and heat fluxes up to 20,000,000 Btu/hr-ft² (1500 W/cm²). These high heat-transfer coefficients are justified by citing Refs. 30 and 69 where these very high values were observed. However, the flow conditions in the references, high subcooling and velocity, are not similar to the conditions of Bennett, and the applicability of these references is questionable.

The early BWR FLECHT* tests^{20,21,31,47,54} were conducted with 49 electrically heated rods at pressures of 15-300 psia (1-20.4 atm). Test results with stainless steel and Zircaloy were similar. Considerable scatter in the data was evident, with the peak clad temperature varying with rod position in the array. The rods adjacent to the stainless steel enclosure, which usually cooled first, had a lower peak temperature than the interior rods. No dependence on water flow rate or initial conditions could be established. However, it was reported that the rewetting rate increased with pressure.

Numerous tests were conducted during the PWR FLECHT program,¹⁰ which simulated LOCA conditions in order to evaluate PWR ECCS performance. Simulated reactor fuel subassemblies in 7 x 7 and 10 x 10 arrays of stainless and Zircaloy clad rods were used. The ECCS of a PWR is primarily a "bottom flooding" device where the large quantities of water are injected into the reactor vessel through the inlet piping. The PWR tests showed liquid entrainment to be an effective heat-transfer mechanism in the region above the rising liquid pool. The effectiveness of the liquid entrainment increased with water temperature. This is a result of larger quantities of steam being generated and, hence, entraining more water. Heat-transfer coefficients between the rod and mist were reported to be 30-100 Btu/hr-ft²-°F (0.017-0.056 W/cm²-°C). As with the BWR FLECHT, the performance of a PWR ECCS is enhanced by increased pressure. The temperature at the quenching front was reported to be 600-1200°F (315-650°C). However, the accuracy of this measurement was poor since data were recorded once every 4 s. Also, the quench-front temperature was not the sputtering-front temperature, but that point where the temperature began to drop rapidly as the rewetting front approached.

By reviewing the literature through 1974, we can conclude that sputtering is a heat-transfer process that has not yet been unambiguously located on the boiling map given by Fig. 2. As the subject of intensive investigations, sputtering has been observed (1) in a wide variety of geometries, (2) on material with different thermal properties, (3) at different pressures, and (4) for a wide range of flow rates and subcoolings. The data have been correlated with one- and two-dimensional models by assigning values to two of the unknowns (such as the sputtering temperature and effective water temperature at the sputtering front), and by varying the third parameter (such as the heat-transfer coefficient) to allow the correlation to fit the data. Some of the pertinent questions about sputtering are:

1. What is the sputtering-front temperature? This temperature is important in identifying the heat-transfer process. Presently, this temperature has been estimated to be 280-500°F (140-260°C). A range this wide will not identify the heat-transfer process.

*Most commercial reactors are presently Boiling Water Reactors (BWR's) or Pressurized Water Reactors (PWR's). Performance of ECCS's were tested in the Full Length Emergency Cooling Heat Transfer (FLECHT) tests for each type of reactor.

2. What is the heat-transfer coefficient? Two-dimensionality can be related to the heat-transfer coefficient, which is reported to vary by a factor of 200.

3. Does water flow rate affect the rewetting velocity? Shires⁶¹ and Yamanouchi^{80,81} indicate that rewetting velocity increases with flow rate; Yoshioka^{82,83} and Bennett⁵ reported no effect.

4. Experimental data have been reported showing the rewetting velocity to increase with water subcooling. At present, no consistent method exists for incorporating this observation in analysis.

III. EXPERIMENT

It was shown in Ch. II that sputtering has been the subject of extensive investigations. Up to the present, all studies of sputtering have been concerned with a moving sputtering front on a vertical rod or tube. The reason for the wide range of experimental sputtering-front temperatures is more easily understood by examining Fig. 1. The rod length where the temperature drops from T_{∞} to T_{liq} is very short, that is, a steep temperature gradient exists in this region. Since investigators have tried to measure the temperature where a steep temperature gradient exists, a slight error in the axial direction would result in considerable temperature error. To further complicate the problem, the sputtering front is moving. In this case not only must the exact location be known, but the temperature must be measured at the instant the sputtering front arrives. Realizing these problems, a different approach to the investigation was undertaken.

With a moving sputtering front, a steep temperature gradient exists at a fixed location for only a short time. The intense boiling at the sputtering front takes place as the falling liquid film progressively moves downward cooling the rod. If a heat source of sufficient intensity were available to sustain the temperature gradient, the downward progress would cease. With a stationary sputtering front, the temperature measurements can be made with much greater accuracy than the previously reported range of 280-500°F (137-260°C). The cooling action in the nucleate-boiling zone lowers the surface temperature independent of the sputtering-front velocity because the water velocity is at least greater by an order of magnitude than the rewetting velocity. The difference between a moving and a stationary sputtering front is that in a moving sputtering front the tube is cooled from an initial temperature to a final temperature at a constant velocity; in a stationary sputtering front thermal energy is supplied at a constant rate. By moving with a rewetting front, it appears to be a steady-state process with the tube surface being cooled from T_{∞} to T_{liq} at a velocity of u_{sput} (see Fig. 1). The stationary sputtering front is truly steady state with the temperature at the same physical location remaining constant. The remainder of this chapter is used to describe the experimental apparatus used. All data obtained with a stationary sputtering front are tabulated in Appendix B.

A. Experiment Apparatus

Up to the present, most test sections have been fabricated from stainless steel or materials with similar thermal properties. With a stationary sputtering front, all the thermal energy must be conducted to the front by a temperature gradient in the test section. If a material of high thermal conductivity is chosen, a lower temperature gradient is required. Copper, which has a conductivity about 20 times greater than stainless steel, was chosen. This choice of material necessitated that all experiments be conducted in an inert atmosphere because of the rapid oxidation of copper at elevated temperatures.

A hood about 40 x 40 x 30 in. (100 x 100 x 75 cm) was purged with argon typically for one day prior to conducting experiments. Manipulation of the test section and other instruments within the hood was accomplished with gloves while observing through the front window, a 1/2-in.-thick Plexiglas plate.

B. Test Section and Heater Assembly

The test section (see Fig. 5) was fabricated from three pieces of copper bar stock and welded together. The entire test section was 25 in. (63 cm) long.

1. The top, of 3/8-in. OD by 17 in. (0.95-cm OD x 43 cm), most of which is not shown in Fig. 5, is where the falling water film flowed and was eventually sputtered off near the bottom. Sputtering usually occurred within 1 in. of the top-body junction.

2. The body, of 2-in. OD by 2 in. (5-cm OD x 5 cm), was the region where thermal energy entered the test section by radiation. The upper lip of the body made an electrical connection with the graphite heater.

3. The stem, of 1/2-in. OD by 6 in. (1.27-cm OD x 15.24 cm), protruded from the body downward into the water bath and functioned as a temperature-moderating device. If the body temperature climbed too high, the stem temperature gradient increased, thus increasing the heat loss to the water bath, and vice versa. The stem also functioned as an electrical connection.

The heat source for these experiments was a graphite sleeve which fit around the test-section body and radiated thermal energy. The graphite was heated by low-voltage, high-current ac power to an estimated 3000°F during normal operation. The top of the heater made electrical contact with the test-section body, and the bottom of the heater made electrical contact with the brass platform. Both the top and bottom of the heater were copper plated to reduce contact voltage drop. Because equal amounts of thermal energy were radiated both inwardly and outwardly, a shielding arrangement had to be constructed. These shields (see Fig. 5) were arranged concentrically by alignment rings in the brass platform. When fully assembled, the apparatus appeared as shown in Fig. 6; a cross-sectional view is shown in Fig. 7.

C. Measurements of Surface Temperature

The Chromel and Alumel leads of the thermocouple probe were located at the end of a modified pair of seizers (see Fig. 8). By grasping the copper test section with the seizers, two thermocouple junctions were formed on the heater surface: a Chromel-copper, and directly opposite it on the vertical copper rod a copper-Alumel. Since both junctions were located at the surface, the signal produced by this type of probe was proportional to the surface temperature at a given elevation. The tips of the seizers including all but the ends

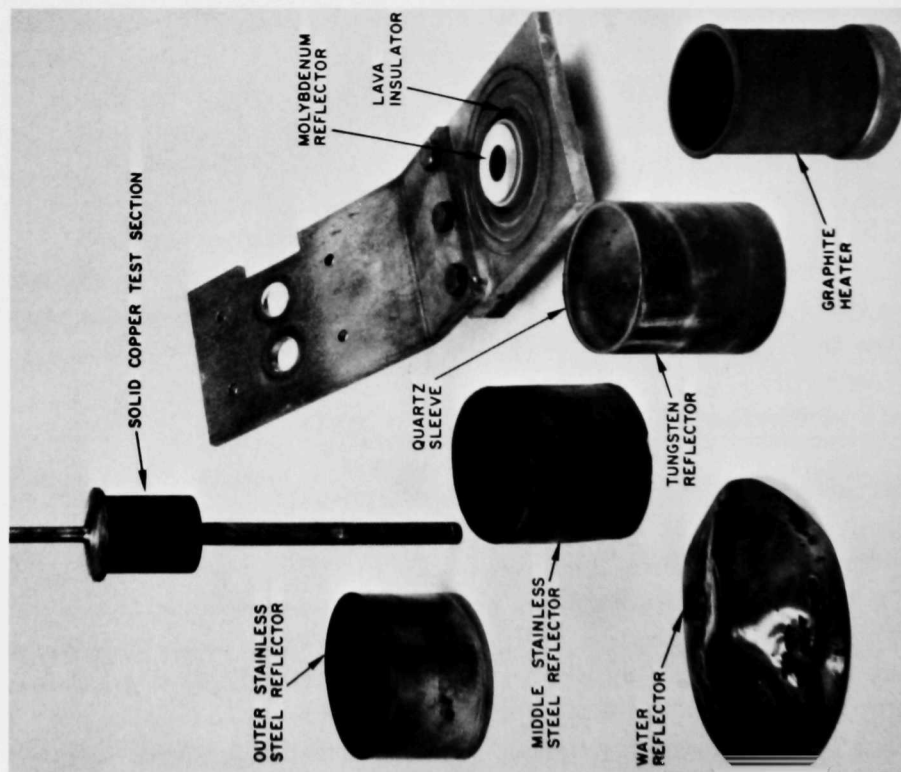


Fig. 5. Test Section, Shields, and Heater. ANL Neg. No. 900-4481A.

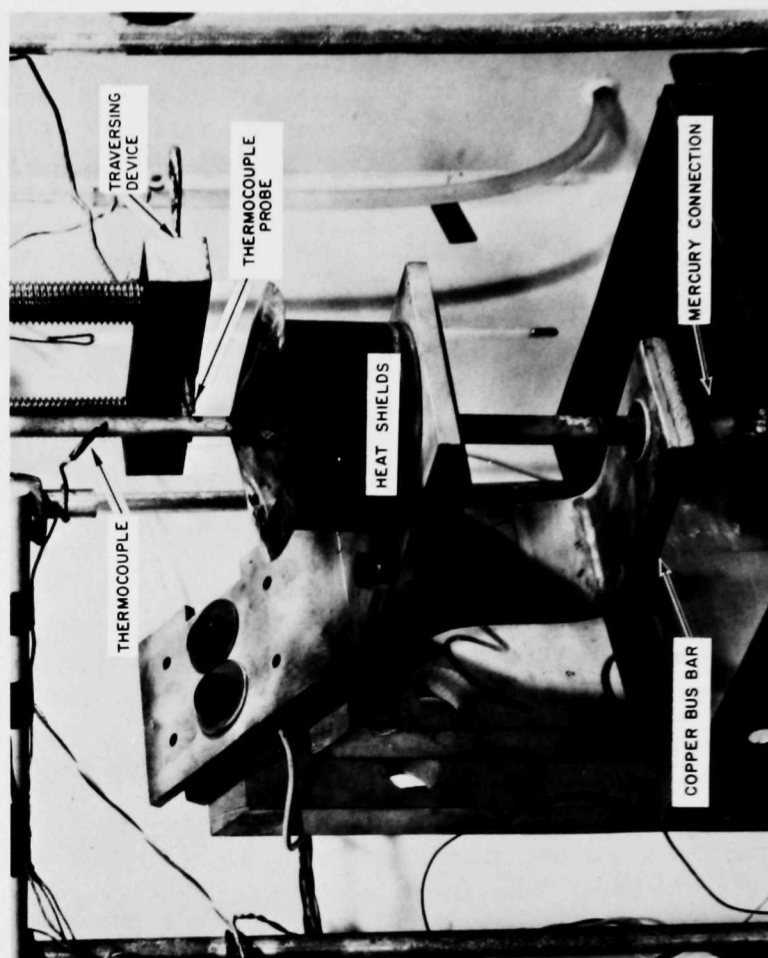


Fig. 6. Assembled Test Section. ANL Neg. No. 900-4506A.

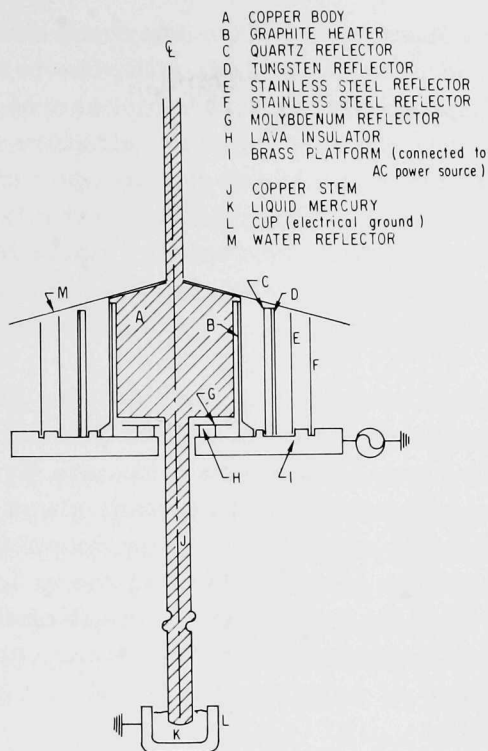


Fig. 7

Cross-sectional View of Test Section and Shields. ANL Neg. No. 900-75-865.

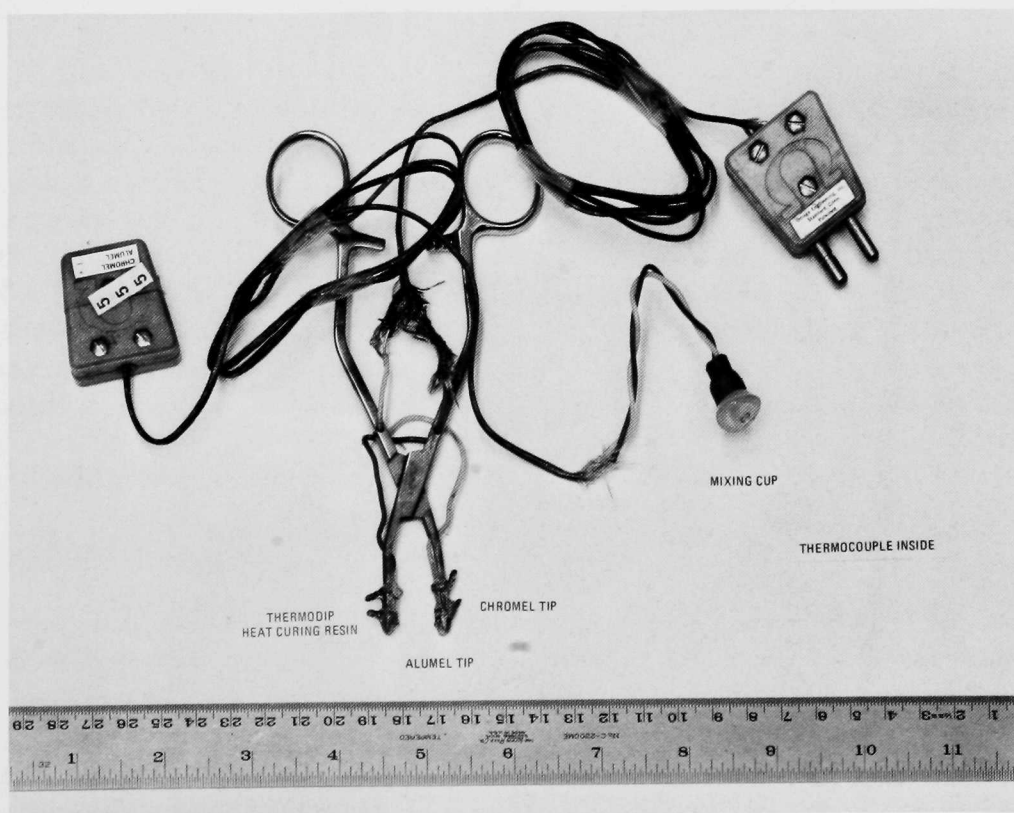


Fig. 8. Thermocouple Probe and Mixing Cup. ANL Neg. No. 900-4504.

of the Chromel and Alumel wires were insulated with a thermal-curing resin. This was done to prevent water from coming in contact with the leads and lowering the junction temperature. Good accuracy and response of the thermocouple probe (see Appendix C) was obtained at reference temperatures (32 and 212°F) (0 and 100°C). The electrical resistance of the probe upon making a circuit with the test section was found to be insignificantly higher than the electrical resistance of a Chromel-Alumel thermocouple of equal length and gauge, indicating good electrical contact with the test section. All temperatures were recorded with a Doric Digitrend 210.

The thermocouple probe was positioned along the vertical rod by a traversing device (see Fig. 9). The probe was inserted into a milled slot in a solid brass block which was moved by twin lead screws. A cam arrangement, located at the top of the lead screws, permitted fixed vertical steps of 0.100, 0.050, and 0.020 in. (0.254, 0.127, and 0.058 cm). This experimental arrangement permitted measurement of the surface temperature at many locations without the constant disruption of the film by permanently positioned thermocouples. The cam arrangement provided constant vertical steps; however, the clearance in the milled slot was a source of error. The tip of the thermocouple

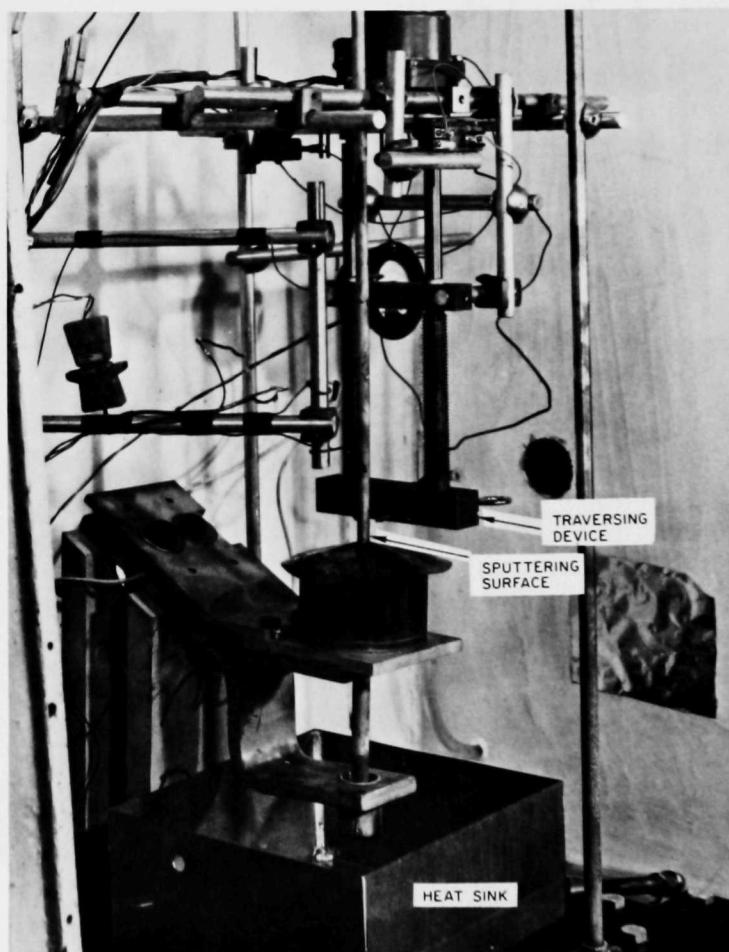


Fig. 9. Interior of Hood. ANL Neg. No. 900-4507A.

probe could move vertically 0.040 in. (1 mm) because of clearance in the milled slot. Normally during testing, the probe was held firmly against one side so there was only negligible movement. However, because of the clearance, the vertical measurement should be considered to be ± 0.020 in. (± 0.051 cm). The temperature error is the total of all the error sources. A tolerance of $\pm 4^\circ\text{F}$ (2°C) should be associated with the thermocouple junction and Digitrend 210. The error due to the clearance in the traversing device is a function of test-section temperature gradient. For example, with a temperature gradient of $1000^\circ\text{F}/\text{in.}$ ($141^\circ\text{C}/\text{cm}$), the error would be $\pm 20^\circ\text{F}$ ($\pm 11^\circ\text{C}$).

D. Sputtered Water Temperature

The temperature of the water sputtered from the rod was initially measured with a Chromel-Alumel thermocouple held near the sputtering front. However, these data had considerable scatter, of the order of 30°F (17°C). This scatter was reduced by using the mixing cup shown in Fig. 8. This cup, which had a negligible thermal capacity, held a Chromel-Alumel thermocouple which measured the average or bulk sputtered water temperature. Data obtained in this manner did not have as much scatter as obtained from the original, bare-thermocouple bead. Even with this improvement, the spray temperature (sputtered water) should be considered $\pm 5^\circ\text{F}$ ($\pm 2.8^\circ\text{C}$).

E. Water Temperature and Condensation Heat Flux

Water was introduced onto the copper rod approximately 17 in. above the sputtering front. A phenol-fiber distributing block held a thermocouple for measuring the water temperature and for distributing the flow around the test-section periphery. This block, shown in Fig. 10, was located at the top of the copper test section. Sleeves of 160-mesh Monel screen were also used to insure the entire periphery was wetted by the falling liquid film. Since there was usually some steam inside the hood, condensation occurred on the film, which increased the film temperature. The film temperature was monitored with thermocouples located 7, 4, and 2 in. above the sputtering front. A linear extrapolation from these three thermocouples was used to estimate the temperature of the liquid entering the sputtering front. Appendix D illustrates how the heat flux due to condensation was determined.

F. Measurements of Water Flow Rate

Demineralized, degassed water was used as a test fluid which was supplied at constant flow rate from a 12.1-gal pressurized reservoir (see Fig. 10). This reservoir was maintained at constant temperature by a water bath. The flow rate was controlled by adjusting a valve on the reservoir and measured by a 3/8-in. Fischer and Porter flowmeter. Flow rates were verified by measuring the volume of water flow during 100 s immediately after a test. The flow-rate data of Appendix B should be considered to be $\pm 5\%$.

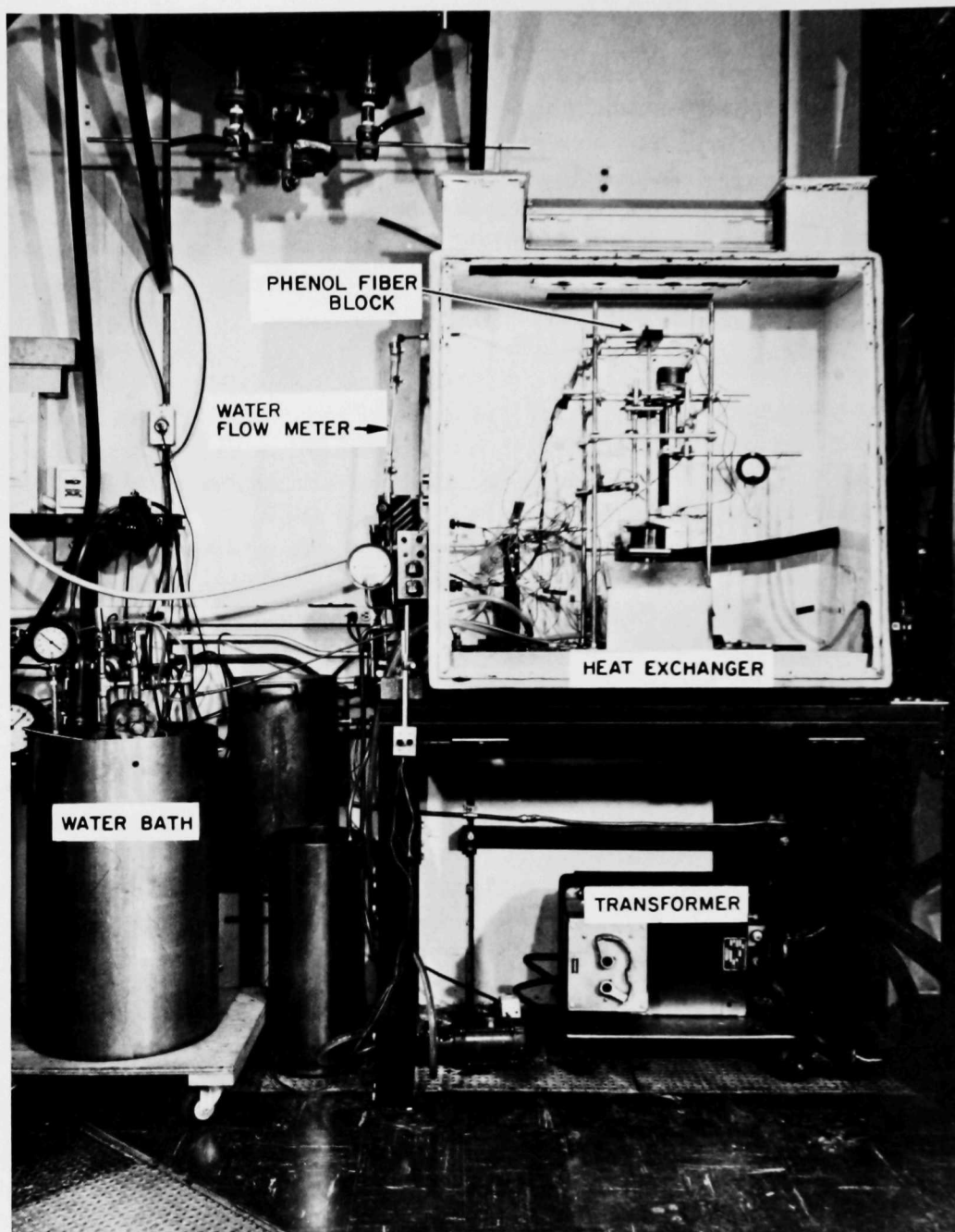


Fig. 10. Test Facility. ANL Neg. No. 900-4508A Rev. 1.

A surfactant, Photoflo-200, was added to the test water to improve the wetting of the copper rod.⁷⁸ This water-surfactant mixture gave a uniform sputtering front with the entire periphery at the sputtering front. The effect of surfactant concentration on the surface tension of water was measured by capillary action with 5- λ pipettes at 70°F. The effect of surfactant was assumed constant with temperature; Fig. 11 shows how the surface tension was estimated as a function of temperature. Surface tension was measured because it is a parameter in boiling correlations. The change in surface tension is given in Appendix B for each test case.

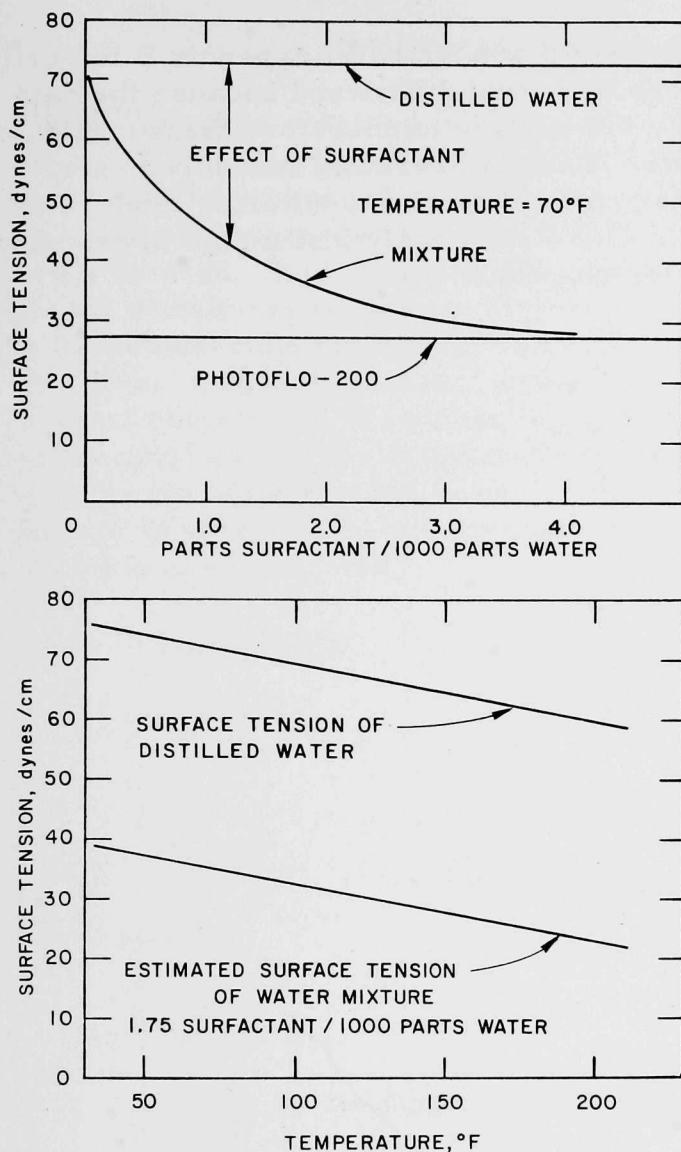


Fig. 11. Effect of Photoflo-200 on Surface Tension.
ANL Neg. No. 900-75-866.

G. Experimental Procedure

All the data were obtained in a hood which had been purged with argon. A minimum of 300 ft³ (8.5 m³), ten times the volume of the hood, was used for purging, which usually took 24 hr. Demineralized, degassed water was used for testing and kept in a water bath to insure that its temperature did not change during testing. If surfactant was to be added to the water, it was added prior to degassing. Also, prior to degassing the desired water temperature was obtained by heating the test water and water bath with low-pressure steam. Condensation within the hood was reduced by means of a heat exchanger using a closed-circuit ethylene glycol loop. The ethylene glycol was cooled with dry ice.

Eighteen temperatures were monitored during testing. Among these was the test-section body temperature, which was maintained constant by equalizing the heat losses and gains. The two methods of controlling the body temperature during sputtering were by altering the electric power

to the heater or by moving the water bath to change the heat loss down the test-section stem to the water bath. When a steady test-section body temperature in the 700-800°F (371-427°C) range was obtained with a stationary sputtering front, surface measurements were taken. Measurements of sputtering surface temperature were obtained by stepping the traversing device and grasping the test section with the thermocouple probe for approximately 2 s at each step. Data were obtained by stepping either upward or downward; the direction was arbitrary and did not affect the data or the time required to record these data ~1 min.

The experimental apparatus described in this chapter performed well, providing data for stationary sputtering fronts for water flow rates varying by a factor of four and subcoolings from 40 to 140°F (22-77°C). The data were

reproducible; runs 7A and 7B and 8A and 8B are listed in Appendix B to verify this fact. The experimental procedure was straightforward because the data were taken at steady state. Normally the surface temperature measurements were taken at a rate of 30 per minute. These temperature measurements were plotted to show the temperature profile through a sputtering front. Examples of these profiles are shown in Ch. VI; the analytical model to describe these data is developed in the following chapter.

IV. MATHEMATICAL MODEL OF SPUTTERING

The data obtained in this study were steady-state data and can be analyzed using a steady-state energy balance. If the test section were considered to be composed of numerous vertically stacked disks and the water as vertically stacked rings (see Fig. 12), a one-dimensional energy balance could be used. The resulting differential equations are coupled and nonlinear; hence, simultaneous numerical solutions are appropriate. A possible problem with the one-dimensional approach is the existence of two-dimensional effects; therefore, a two-dimensional model will also be developed. Since the computational burden of a two-dimensional calculation can be greatly reduced by a good initial guess, the calculated one-dimensional temperature profile will be used as the starting conditions. It will be shown in Ch. VI that two-dimensional effects do exist but do not dominate for these data; hence, a one-dimensional model is adequate here.

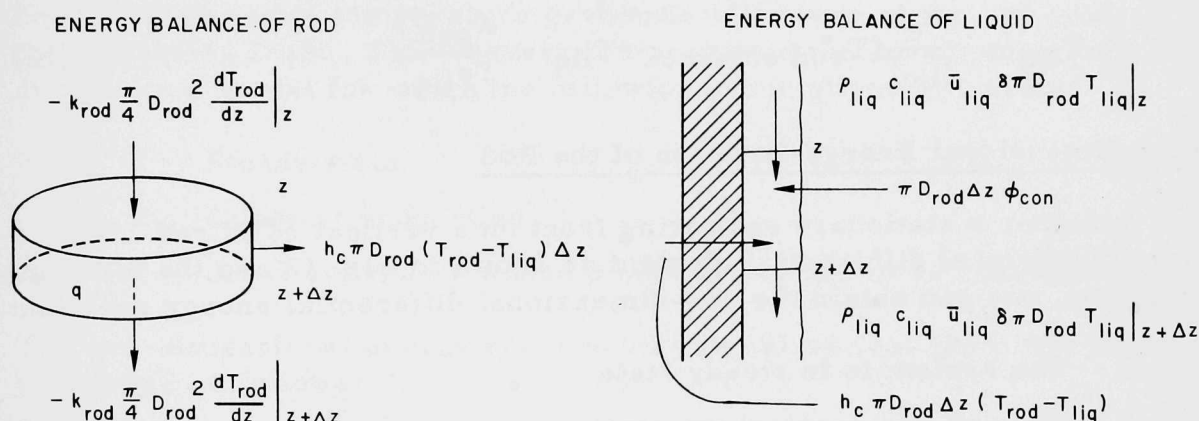


Fig. 12. One-dimensional Model of Sputtering. ANL Neg. No. 900-75-867.

A. One-dimensional Energy Equation of the Liquid

The differential element for the one-dimensional energy equation for the falling liquid film is shown in Fig. 12. The following assumptions are made:

1. The kinetic and potential energies of the liquid film are negligible.
2. There is no axial heat transfer in the liquid.
3. Mass flow rate due to condensation is negligible compared to the mass flow rate of the film.
4. The film thickness is small compared to the rod radius and, hence, a rectangular coordinate system can be used.
5. The film can be modeled adequately by one-dimensional analysis.
6. Steady state is assumed.

The energy equation of the liquid becomes

$$\begin{aligned} \frac{d}{dz} T_{\text{liq}} = & \frac{h_c}{\delta \rho_{\text{liq}} c_{\text{liq}} \bar{u}_{\text{liq}}} (T_{\text{rod surface}} - T_{\text{liq}}) \\ & + \frac{\varphi_{\text{con}}}{\rho_{\text{liq}} c_{\text{liq}} \bar{u}_{\text{liq}} \delta}, \end{aligned} \quad (10)$$

where the condensation heat flux φ_{con} is estimated as shown in Appendix D. Introducing the variable Γ , which is the mass flow rate per unit periphery:

$$\Gamma = \rho_{\text{liq}} \bar{u}_{\text{liq}} \delta, \quad (11)$$

Eq. 10 becomes

$$\frac{d}{dz} T_{\text{liq}} = \frac{h_c}{c_{\text{liq}} \Gamma} (T_{\text{rod surface}} - T_{\text{liq}}) + \frac{\varphi_{\text{con}}}{\Gamma c_{\text{liq}}}. \quad (12)$$

B. One-dimensional Energy Equation of the Rod

Consider a stationary sputtering front on a vertical solid rod. With the one-dimensional differential element as shown in Fig. 12 and the following assumptions, one can obtain the one-dimensional differential energy equation:

1. The system is in steady state.
2. The rod has constant properties.

The resulting equation is

$$\frac{d^2}{dz^2} T_{\text{rod}} = \frac{4h_c}{k_{\text{rod}} D_{\text{rod}}} (T_{\text{rod}} - T_{\text{liq}}). \quad (13)$$

The one-dimensional temperature profiles for the rod and liquid can be obtained by the simultaneous solution of Eqs. 10 and 13.

The characteristic distance for a cylindrical geometry is one-quarter of the diameter. By introducing the dimensionless parameter

$$\zeta = \frac{z}{D_{\text{rod}}/4}, \quad (14)$$

Eq. 13 can be rewritten as

$$\frac{d^2}{d\zeta^2} T_{\text{rod}} = \frac{h_c D_{\text{rod}}}{4k_{\text{rod}}} (T_{\text{rod}} - T_{\text{liq}}). \quad (15)$$

The term $h_c D_{rod}/4k_{rod}$ is a dimensionless number known as the Biot number, which can be considered as

$$\text{Biot number} = \frac{\text{internal thermal resistance}}{\text{surface thermal resistance}}. \quad (16)$$

If the Biot number is much larger than one, the internal resistance determines the heat transfer; conversely, if the Biot number is much less than one, the heat transfer is determined at the surface. In one-dimensional analysis, there is no distinction between the rod surface temperature and the interior temperature. This is not the case for two-dimensional analysis of the rod.

C. Two-dimensional Analysis of the Rod

Nucleate boiling has been observed with sputtering fronts. Heat fluxes of the order of 1,000,000 Btu/hr-ft² are associated with nucleate boiling and, hence, steep radial temperature gradients will occur at the rod surface near the sputtering front. This observation prompted the development of a two-dimensional model for which the following assumptions are made:

1. Steady state.
2. Constant properties.
3. Axial symmetry where a one-radian sector is considered.

The two-dimensional energy equation in this cylindrical geometry (see Fig. 13) is handled as follows:

$$\begin{aligned} & -k_{rod} \frac{1}{8} (D_{out}^2 - D_{in}^2) \frac{\partial T_{rod}}{\partial z} \Big|_z - \left[-k_{rod} \frac{1}{8} (D_{out}^2 - D_{in}^2) \frac{\partial T_{rod}}{\partial z} \Big|_{z+\Delta z} \right] \\ & - k_{rod} D_{in} \frac{\Delta z}{2} \frac{\partial T_{rod}}{\partial r} \Big|_{D_{in}} - \left(-k_{rod} D_{out} \frac{\Delta z}{2} \frac{\partial T_{rod}}{\partial r} \Big|_{D_{out}} \right) = 0. \quad (17) \end{aligned}$$

For the numerical method used here, relaxation, this is approximated as

$$\begin{aligned} & \frac{(D_{out}^2 - D_{in}^2)}{4} \frac{\Delta T_{rod}}{\Delta z} \Big|_{z+\Delta z} - \frac{(D_{out}^2 - D_{in}^2)}{4} \frac{\Delta T_{rod}}{\Delta z} \Big|_z \\ & + D_{out} \Delta z \frac{\Delta T_{rod}}{\Delta r} \Big|_{D_{out}} - D_{in} \Delta z \frac{\Delta T_{rod}}{\Delta r} \Big|_{D_{in}} = 0. \quad (18) \end{aligned}$$

This equation is solved for each z , r location throughout the grid. For the analysis done here, this grid was 450 elements long in the axial direction z ,

each element representing a distance of 0.005 in. The grid was eight elements wide with each element having the same cross-sectional area. It was found that this grid structure, where each element had equal mass, speeded the convergence. Details of the numerical method are given in Appendix E.

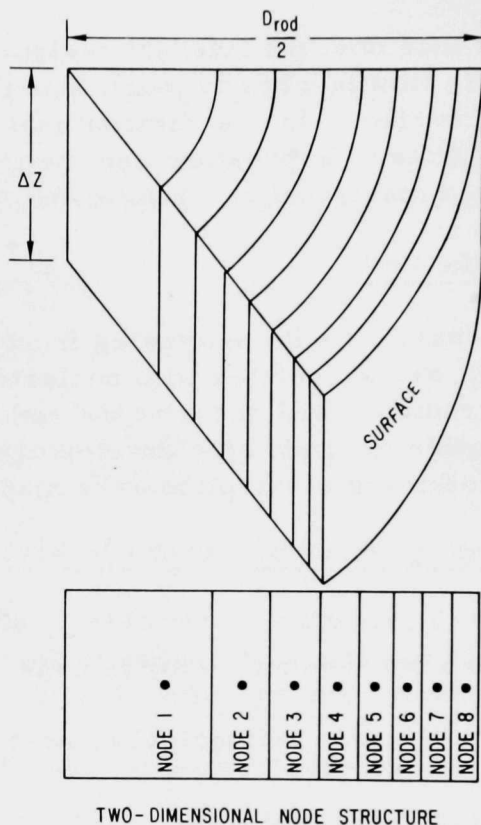


Fig. 13

Two-dimensional Model
of Sputtering. ANL Neg.
No. 900-75-868.

In order to use this model to analyze the stationary-sputtering-front data obtained here, the simultaneous solution of the temperature field within the rod and the liquid film must be obtained. It has already been pointed out that the heat-transfer coefficient h_c is a function of the dependent variables. Because h_c is the key to the sputtering problem and because h_c varies by two orders of magnitude for some flow conditions near a sputtering front, the entire next chapter is devoted to a discussion of it.

V. SPUTTERING PHENOMENA

Consider a device, illustrated in Fig. 14, capable of sustaining a stationary sputtering front. Let the event be examined as a three-region phenomenon as shown in the figure:

1. A quiescent falling film zone extending up from the nucleate boiling zone.
2. A short nucleate boiling zone immediately above the sputtering front.
3. A dry adiabatic zone extending down from the sputtering front.

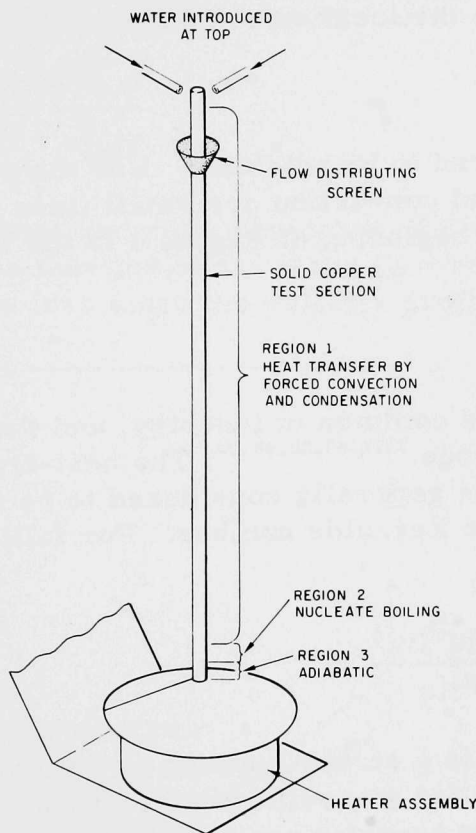


Fig. 14

Three Heat-transfer Regions.
ANL Neg. No. 900-75-869.

This chapter will present numerous heat-transfer correlations from the literature. Those correlations most applicable to sputtering will be selected, and a method will be proposed for calculating the heat-transfer coefficient throughout a sputtering front. This method is based upon the premise that sputtering is a nucleate-boiling process and that the front corresponds to a CHF phenomena. This chapter will be concluded with an example of how to use this method of linking the various heat-transfer correlations together.

If we begin at some location far enough above the sputtering front such that the temperature of the rod and the liquid are unaffected by the sputtering, the different modes of heat transfer are:

Region 1

1. Heat transfer from the rod to the falling film by nonboiling forced convection.

2. Heat transfer from the argon-steam atmosphere inside the hood to the falling film by condensation. This heat flux is considered to be a constant and is evaluated in Appendix D.

Region 2

Forced-convection boiling occurs in Region 2. Local conditions determine if this boiling is saturated or subcooled. The criterion used for determining the beginning of Region 2 is the location of incipient boiling.

Region 3

This region can be considered to be adiabatic. For the present situation, heat fluxes due to radiation and convection are small (less than 1% of Region 2) and can be ignored. The beginning of Region 3 is the location of the CHF point on the rod surface.

A. Falling-film Heat Transfer

Falling-film heat transfer is common in industry, and the literature contains many references to this mode.^{3,12,49,50,59,70} The heat-transfer coefficient between the rod and the film is generally considered to be related to the flow regime as characterized by the Reynolds number. For falling films, the Reynolds number is defined as⁸

$$Re = \frac{\text{inertial forces}}{\text{viscous forces}} = \frac{4\rho_{\text{liq}}\bar{u}_{\text{liq}}\delta}{\mu_{\text{liq}}} \quad (19)$$

Since the viscosity of water is a strong function of temperature,³⁸ the Reynolds number must be evaluated for a specific temperature. Two other dimensionless groups related to heat transfer are the Prandtl number and the Nusselt number:

$$Pr = \frac{\text{kinematic viscosity}}{\text{thermal diffusivity}} = \frac{\nu_{\text{liq}}}{\alpha_{\text{liq}}} \quad (20)$$

and

$$Nu = \frac{\text{temperature gradient at wall}}{\text{reference temperature gradient}} = \frac{h_c \delta}{k_{\text{liq}}} \quad (21)$$

It can be shown by dimensional analysis that these three groups can be related to each other without regard to flow regime as

$$Nu = F(Re, Pr). \quad (22)$$

For falling liquid films, the reported relationships between these three groups vary by a factor of two depending upon the Reynolds number. This discrepancy is a result of the difficulty in defining the flow regime. The appearance of waves or ripples on the free surface enhances the heat transfer before a transition to turbulent flow occurs. Therefore in the transition from laminar to turbulent flow, the appearance of waves expands the heat-transfer problem. If the flow regime were laminar, a momentum balance could be used to relate the flow rate to the film thickness:

$$\delta = \sqrt{\frac{3\mu_{\text{liq}}\Gamma}{\rho_{\text{liq}}g}}. \quad (23)$$

The dashed lines and right ordinates of Figs. 15 and 16 show the laminar film thickness as a function of Γ . If the flow regime were turbulent, the film thickness would be less since the velocity profile is flatter.

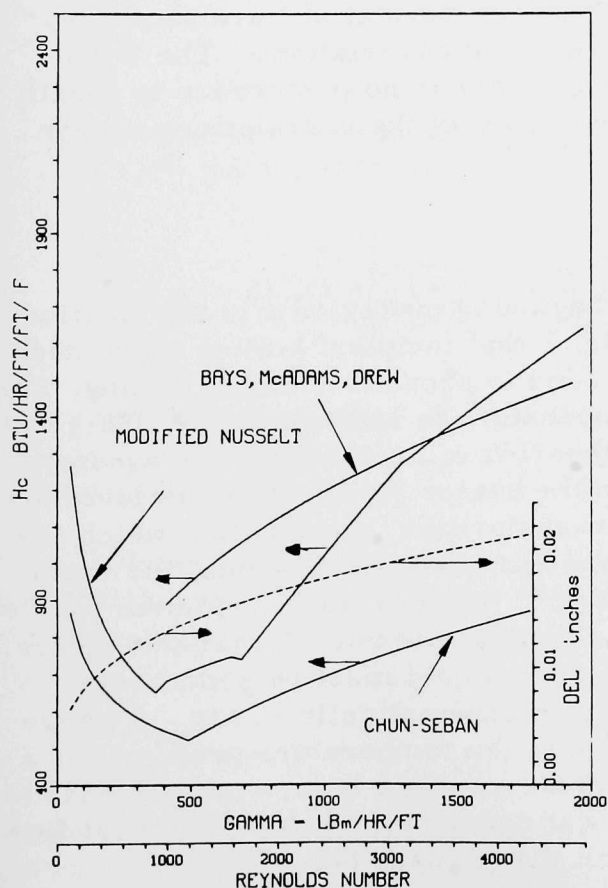


Fig. 15. Falling-film Heat Transfer for Water at 100°F. ANL Neg. No. 900-75-870 Rev. 1.

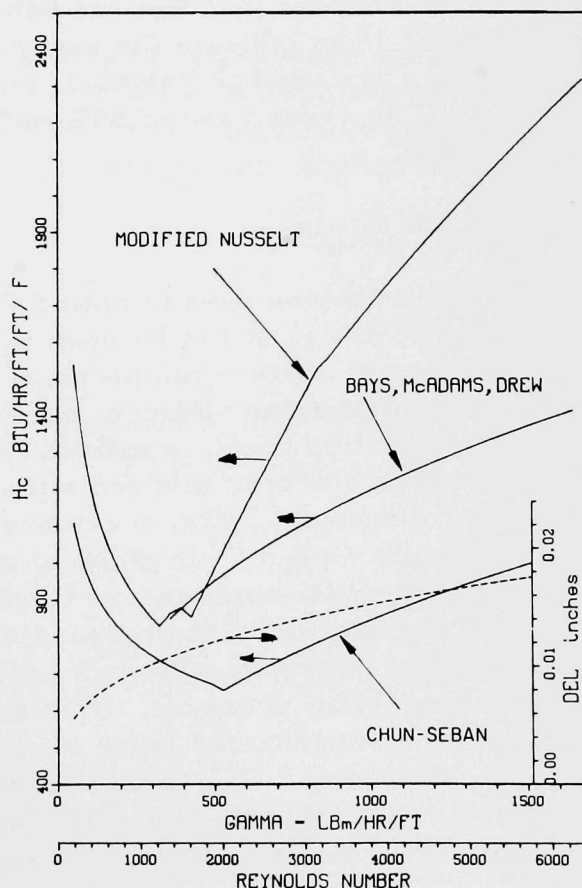


Fig. 16. Falling-film Heat Transfer for Water at 150°F. ANL Neg. No. 900-75-871 Rev. 1.

These differences in flow regimes for the same apparent conditions have led to the wide range of reported heat-transfer coefficients. Figures 15 and 16 compare three correlations for water at 100 and 150°F. The original Nusselt correlation⁵² was modified by Wilke⁷⁹ to include a wavy laminar and transition region. Wilke's data, obtained on the outside of a brass rod, were correlated with the following equations:

$$Nu = 1.88 = \frac{h_c \delta}{k}; \text{ Re} < 2460 \text{Pr}^{-0.646} \text{ (laminar flow)}, \quad (24)$$

$$Nu = 0.0641 \left(\frac{\text{Re}}{4} \right)^{8/15} \text{Pr}^{0.344}; \quad 2460 \text{Pr}^{-0.646} \leq \text{Re} < 1600 \text{ (wavy laminar)}, \quad (25)$$

$$Nu = 0.00112 \left(\frac{\text{Re}}{4} \right)^{6/5} \text{Pr}^{0.344}; \quad 1600 \leq \text{Re} < 3200 \text{ (transition region)}, \quad (26)$$

and

$$Nu = 0.0066 \left(\frac{\text{Re}}{4} \right)^{14/15} \text{Pr}^{0.344}; \quad \text{Re} \geq 3200 \text{ (turbulent)}. \quad (27)$$

Correlations by Chun and Seban¹² and by Bays et al.⁴ are shown in Figs. 15 and 16 to indicate the range of reported correlations. The Wilke correlations are used in Region 1, although there is no preference to specify that one. If an error band of 50% were used, all of the correlations appear equally good.

B. Incipient Boiling

The criterion used to define the beginning of Region 2 is the location of incipient boiling. It can be seen in Fig. 2 that incipient boiling is defined by the minimum surface temperature needed to produce nucleate boiling. For water at atmospheric pressure, this temperature is approximately 10°F greater than the saturation temperature. Most theories of nucleate boiling assume that nucleation starts at favored sites on the heater surface. These favored sites are microscopic pits, scratches, irregularities, and cavities which are not completely wetted.⁷⁴ If vapor is trapped inside these cavities, the vapor expands as the wall temperature increases.³⁴ The pressure inside the bubble is higher than the ambient pressure due to surface tension forces and, hence, for the bubble to expand, the wall and adjacent liquid must be superheated relative to ambient pressure. This is shown schematically in Fig. 17 where the depth of a superheated layer is related to the temperature gradient for a specific cavity size. This liquid temperature gradient in turn corresponds to the incipient heat flux ϕ_{incip} . This physical description of incipient heat flux has led to the following correlation, which will be used here:⁷

$$\phi_{\text{incip}} = 15.6 P^{1.156} \exp[2.3/P^{0.0234} \ln(\Delta T_x)]. \quad (28)$$

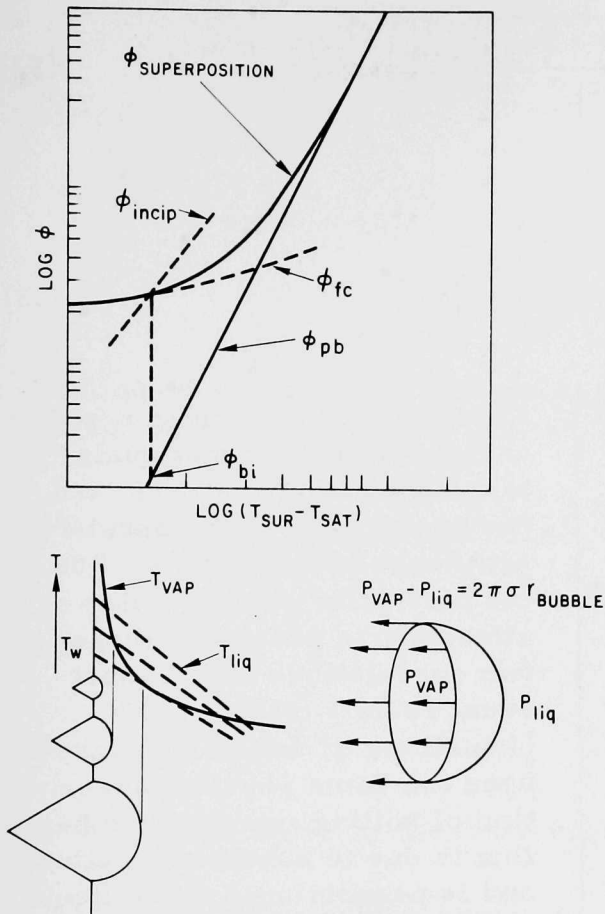


Fig. 17. Superposition and Bubble Nucleation.
ANL Neg. No. 900-75-872.

An example of the iterative method required for the solution of Eq. 28 is given at the end of this chapter.

C. Region 2--Nucleate Boiling

Region 2 is defined to exist from the location of incipient boiling to the location where the heat flux equals the local CHF. Generally for water at atmospheric pressure these surface temperatures range from 10 to 60-90°F above saturation.⁶⁰ Since the present situation is for flow boiling, the method of superposition will be used (see Fig. 17).

Forced-convection nucleate-boiling heat flux has been considered to be the sum of the pool-boiling heat flux and the forced-convection heat flux:⁵⁸

$$\varphi_{fc,b} = \varphi_{fc} + \varphi_{pb}. \quad (29)$$

This was later modified by Bergles⁷ to provide a curve for a smooth transition from forced-convection nonboiling to forced-convection boiling (see Fig. 17):

$$\varphi_{fc,b} = \varphi_{fc} \left\{ 1 + \left[\frac{\varphi_{pb}}{\varphi_{fc}} \left(1 - \frac{\varphi_{bi}}{\varphi_{pb}} \right) \right]^2 \right\}^{1/2}. \quad (30)$$

The superposition method of Eq. 30 is used in Region 2 where $\varphi_{fc} = h_c | \text{falling film} (T_{\text{wall}} - T_{\text{liq}})$, φ_{pb} is the pool boiling heat flux, and φ_{bi} is the boiling heat flux at $\Delta T_{x,ib}$.

Numerous correlations are available in the literature for estimating pool-boiling heat fluxes.^{3,13,23,24,25,33,37,46,48,58,66} The controlling parameter in nucleate-boiling heat transfer has generally been accepted as $\Delta T_x = (T_{\text{sur}} - T_{\text{sat}})$.³⁹ Typically, boiling-heat-transfer correlations are of the form

$$\varphi_{pb} = C \Delta T_x^n, \quad (31)$$

where the values of C vary from system to system and the exponent n is in the range from 2 to 8. The Roshenow⁵⁸ and Levy⁴⁶ correlations are of this type and are, respectively,

$$\varphi_{pb} = c_{liq}^3 Pr^{-5.1} \frac{\mu_{liq}}{C_{sf}^3 h_{fg}^2} \sqrt{\frac{g(\rho_{liq} - \rho_{vap})}{g_c \sigma}} \Delta T_x^3 \quad (32)$$

and

$$\varphi_{pb} = \frac{k_{liq} c_{liq} \rho_{liq}^2}{\sigma T_{sat} (\rho_{liq} - \rho_{vap}) \beta_L} \frac{1}{\left[1 + \frac{\Delta T_{sub} c_{liq}}{h_{fg}} \right]} \Delta T_x^3 \quad (33)$$

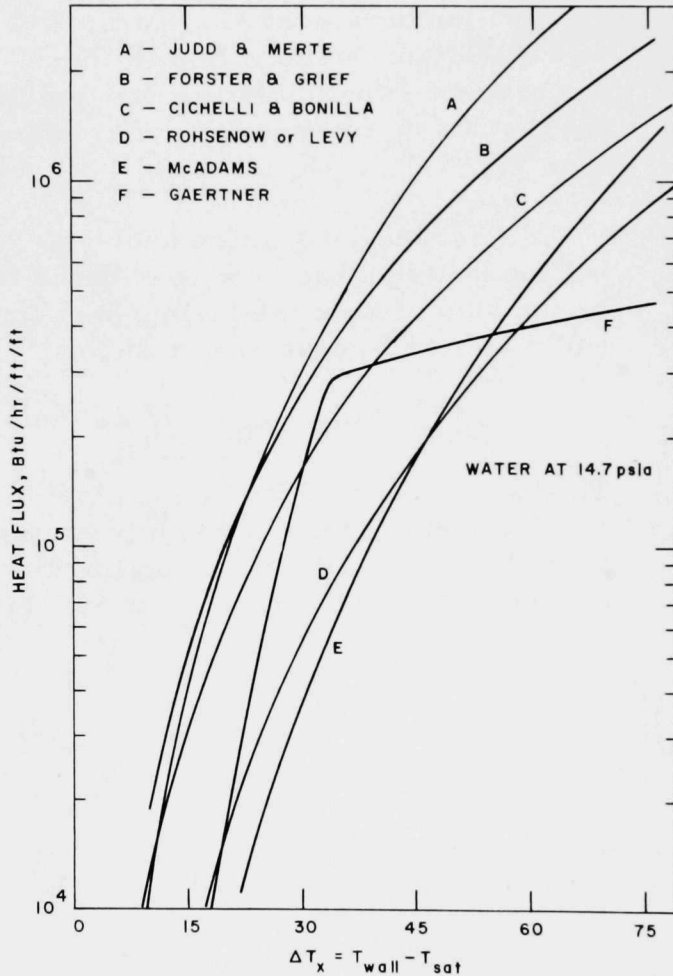


Fig. 18. Pool-boiling Correlations. ANL Neg. No. 900-75-873.

the experimental data differ by a factor of three. Thus, for the calculations shown in Fig. 18, the suggested value of β_L has been decreased by a factor of three.]

Two correlations in Fig. 18 which are for water at atmospheric pressure are

Experimental data from a wide variety of surface materials, test fluids, temperatures, and pressures have been correlated with these two relations. For the particular case of water at atmospheric pressure, these two correlations give almost equal results (see Fig. 18). [Equations 32 and 33 are based upon the same physical description of boiling, namely, the heat flux is due to bubble nucleation, and is proportional to the liquid agitation due to bubbles being formed at the surface and subsequently departing or collapsing. In Eq. 32, C_{sf} is an empirical coefficient for various fluids and surfaces. The term β_L of Eq. 33 corresponds to the term C_{sf} of Eq. 32; β_L is an empirical function of ρ_{liq} and h_{fg} ; the suggested functional relation of $\beta_L(\rho_{liq}, h_{fg})$ does reasonably well for much of the reported boiling data. Unfortunately, for water at atmospheric pressure the suggested value of β_L and the value of β_L needed to make Eq. 33 accurately predict

$$\varphi_{pb} = 0.16Pr^{1/3} \left(\frac{g\beta k_{liq}}{v_{liq}} \right)^{1/3} [\Delta T_x + (T_{sat} - T_{liq})]^{1/3} \left(\frac{a}{g} \right)^{1/3} \\ + 2.39 \cdot 10^6 Pr^{-4.1} \left[k_{liq} \frac{\Delta T_x + (T_{sat} - T_{liq}) \left(\frac{c_{liq} \Delta T_x}{h_{fg}} \right)^2}{\sqrt{\frac{g_c \sigma}{g \rho_{liq}}}} \right]. \quad (34)$$

Equation 34 successfully correlated pool-boiling data obtained with a centrifuge for accelerations from 1 to 100 g:³⁷

$$\varphi_{pb} = C_1 \frac{k_{liq}}{2\sigma} \Delta P \Delta T_x \left(\frac{\rho_{liq}}{\mu_{liq}} A^2 \right)^{1/5} \left(\frac{\mu c_{liq}}{k_{liq}} \right)^{1/3}, \quad (35)$$

where

$$\Delta P = \frac{dP}{dT} \Delta T_x$$

(dP/dT is estimated by the Clapeyron equation),

$$A = \frac{c_{liq} \rho_{liq} (\pi \alpha)^{1/2} T_{sat}}{(h_{fg} \rho_{vap})^2} \Delta P,$$

and for water $C_1 = 0.007$.²³

Two pool-boiling correlations specifically for water at atmospheric pressure which are shown in Fig. 18 are those of McAdams⁴⁸ and Cichelli,¹³ respectively,

$$\varphi_{pb} = 0.074 \Delta T_x^{3.86} \quad (36)$$

and

$$\varphi_{pb} = 42 \Delta T_x^{2.42}. \quad (37)$$

It has been postulated²³ that the high heat fluxes obtained with boiling are a result of the intense agitation of the liquid layer at the surface. This agitation is caused by the growth and collapse or departure of bubbles at the surface. The pumping action of the bubbles mechanically moves the superheated water adjacent to the surface away and replaces it with cooler water. It has been observed²⁴ that subcooling does affect this pumping action. Increased liquid subcooling increases the frequency at which bubbles nucleate

at the surface. This in itself would increase the heat transfer; however, the increased subcooling also affects the average bubble size at departure, which decreases with subcooling. The net result is only a small increase in heat flux with increased subcooling. The correlations of Levy⁴⁶ (Eq. 33) and of Judd and Merte³⁷ (Eq. 34) consider the subcooling effects, which are usually less than 15% of the pool-boiling heat flux.

Another curve of Fig. 18 shows a correlation for the data obtained by Gaertner.²⁴ These data were obtained for a temperature-controlled surface of water at atmospheric pressure up to and including the CHF point. The expression for pool-boiling heat flux recommended by Gaertner is

$$\varphi_{pb} = 0.0012\Delta T_x^{5.5} \text{ for } \Delta T_x \leq 35^\circ\text{F} \quad (38)$$

and

$$\varphi_{pb} = 35000\Delta T_x^{0.5} \text{ for } \Delta T_x > 35^\circ\text{F}. \quad (39)$$

As can be seen from Fig. 18, there is considerable scatter in the pool-boiling heat flux. (Gaertner²⁴ and Kurihara⁴⁰ used the same experimental apparatus, and their data differed by a factor of 2.5. Apparently even experimental techniques can affect the data. However, within a given set of data the trends are consistent, the data reproducible, and the correlations accurate.) Since a large variety of surface-liquid combinations have been correlated by the Rohsenow model, Eq. 32, this type of expression is more easily accepted. Vachon⁷² extended the original Rohsenow pool-boiling correlation to encompass a wider range of surface-liquid combinations and surface preparations. A least-squares fit was used to correlate the data, in which the exponent of the Prandtl number was related to surface cleanliness and the exponent of the excess temperature was related to the surface roughness. Vachon reported that, for a smooth copper-water combination, the excess temperature exponent ranged from 4 to 8:

$$\varphi_{pb} = 0.184\Delta T_x^{4.16} \text{ (4/0 emery surface polish);} \quad (40)$$

$$\varphi_{pb} = 4.022 \cdot 10^{-4}\Delta T_x^{6.66} \text{ (2/0 emery surface polish);} \quad (41)$$

$$\varphi_{pb} = 1.2586 \cdot 10^{-5}\Delta T_x^{7.69} \text{ (3/0 emery surface polish).} \quad (42)$$

Equation 41 will be used here because it is believed that the copper-rod surface is best described by those conditions. Calculations with Eqs. 40 and 42 are shown in Ch. VI for comparison.

The reason for using the Vachon exponents and constants is that these values are specifically for water boiling on copper at atmospheric pressure.

The original Rohsenow exponent, 3, is for a wide range of fluids and heater materials. Vachon has published recommended surface-liquid coefficients and exponents for many different combinations. If these calculations were to be done with a different combination of materials, other values could be used. In this manner, the general nature of Eq. 32 is maintained. Equation 30 can now be used to determine the boiling heat flux, where the forced-convection heat flux is $(h_c |_{\text{falling film}})(T_{\text{rod}} - T_{\text{liq}})$ and the pool-boiling heat flux is determined by Eq. 41. The effects of subcooling are smaller than the uncertainty in the nucleate-boiling heat flux and hence can be ignored.

D. Approach to CHF

Extrapolating the Rohsenow correlation, Eq. 32, to CHF would yield unreasonably high heat fluxes at measured CHF surface temperatures. The nucleate-boiling heat flux has been observed to be a smoothly continuous process at CHF because of competing physical processes at the heated surface.^{62,68} Increasing the nucleate-boiling surface temperature increases both the number of nucleation sites and bubble-departure frequency. Gaertner observed that, as the CHF was approached, continuous columns of vapor emanated from nucleation sites. The maximum upward flow of vapor without inhibiting the downward flow of liquid occurred at the CHF.

At higher surface temperatures, the larger volumes of departing vapor limited the downward flow of water. A means must be found to complete the boiling curve up to that point. It was shown that Gaertner correlated his data (see Fig. 18) as two straight lines on a log-log plot with a change in slope at approximately 0.5 CHF. This is a simple correlation and does not satisfy the criterion of the CHF being a relative maximum. A means of calculating the boiling heat flux as a function of surface temperature which satisfies the following constraints is desirable:

1. The calculated heat flux must equal the heat flux as calculated by Eq. 30 at some intermediate point. The location of this point is arbitrary. For the work done here, a value of 0.6 CHF is used. Calculations with a value of 0.4 CHF, 0.6 CHF, and 0.8 CHF are compared in Ch. VI.
2. The calculated heat flux must equal the CHF when the surface temperature equals the temperature needed to produce a CHF phenomena.
3. The slope of the calculated heat flux at CHF is zero, that is, the curve has a relative maximum at CHF.^{51,55}

These three constraints determine a parabola:

$$\phi_{\text{pb}} = A\Delta T_x^2 + B\Delta T_x + C. \quad (43)$$

This approximation is used from 0.6 CHF to CHF; the boundary conditions which determine the constants A, B, and C are evaluated at local conditions.

E. The Critical Heat Flux

The location of the CHF on the boiling map can be found by determining its coordinates, ΔT_x and ϕ_{CHF} . Unlike the case with pool boiling, the influence of velocity and subcooling are significant, and will be considered.^{14,42,43,65,67} Pressure is also a significant factor, but since all the data taken here are at 1 atm, it will not be discussed. (Increased pressure increases the CHF. For water, the CHF increases up to 1200 psia and then decreases with pressure. The FLECHT tests were conducted at various pressures up to 300 psia, where increased rewetting velocities were observed with increased pressures.) Generalized CHF correlations do exist,^{56,84} but, as with pool-boiling correlations, a wide range of values can be calculated. One such correlation is the superposition approach by Levy:⁴⁴

$$\phi_{CHF} = \phi_{CHF,pb} + \phi_{sub} + \phi_{fc}, \quad (44)$$

where

$$\phi_{CHF,pb} = 0.131 h_{fg} \rho_{vap} \left[\frac{\sigma g g_c (\rho_{liq} - \rho_{vap})}{\rho_{vap}^2} \right]^{1/4}, \quad (45)$$

$$\phi_{sub} = 0.696 (k_{liq} \rho_{liq} c_{liq})^{1/2} \left[\frac{g (\rho_{liq} - \rho_{vap})}{\sigma g_c} \right]^{1/4} \left[\frac{\sigma g g_c (\rho_{liq} - \rho_{vap})}{\rho_{vap}^2} \right]^{1/8} \Delta T_{sub}, \quad (46)$$

and

$$\phi_{fc} = 0.023 \frac{k_{liq}}{D} \left(\frac{GD}{\mu_{liq}} \right)^{0.8} \left(\frac{\mu_{liq}}{k} \right)^{0.33} (T_{sur} - T_{liq}). \quad (47)$$

Another superposition approach was suggested by Chang,¹¹ in which the CHF was the summation of the sensible heat transport by liquid convection and the latent heat transport by the bubbles. The superposition approach of Eq. 44 will be used here; however, other CHF correlations will be presented for the sake of comparison.

Gunther³⁰ conducted a photographic study of forced-convection boiling from 1 atm to 164 psia. The CHF data for water were correlated as

$$\phi_{CHF} = 7000 \bar{u}_{liq} \Delta T_{sub}. \quad (48)$$

This product-type correlation was limited to the range of $5 < \bar{u}_{liq} < 40$ fps and $22 < \Delta T_{sub} < 282^\circ\text{F}$. On the basis of his data, Gunther proposed the following rule of thumb for forced-convection water:

$$\frac{\varphi_{CHF}}{\varphi_{fc}} \approx \frac{\bar{u}_{liq}^{0.5}}{\bar{u}_{liq}^{0.8}} = \frac{10}{\bar{u}_{liq}^{0.3}}. \quad (49)$$

Kutateladze⁴¹ examined pool boiling of water at 1 atm and reported the effects of liquid subcooling on the CHF magnitude with the following relation:

$$\varphi_{CHF} = 504000 + 1400\Delta T_{sub}. \quad (50)$$

Vleit and Leppert⁷³ measured the CHF of forced convection water at 1 atm in 0.105-in. -ID tube. They recommended a superposition type of correlation:

$$\varphi_{CHF} = 504000 + 86400\bar{u}_{liq} + 1400\Delta T_{sub}. \quad (51)$$

A general CHF relation based upon the physical properties of the fluid where the subcooling effect is included by a superposition method is³⁵

$$\varphi_{CHF} = 0.16h_{fg}\rho^{1/2}[g\sigma(\rho_{liq} - \rho_{vap})]^{1/4}(1 + \beta\Delta T_{sub}), \quad (52)$$

where

$$\beta = 0.1 \left(\frac{\rho_{liq}}{\rho_{vap}} \right)^{0.75} \frac{c_{liq}}{h_{fg}}.$$

However, to use the superposition method of Levy, a forced-convection term must be added to Eq. 52. Thus a complete expression for CHF is

$$\varphi_{CHF} = [\varphi_{CHF} \text{ (Eq. 52)}] + [h_c | \text{Eqs. 24-27} (T_{sur} - T_{liq})]. \quad (53)$$

The CHF data of Vliet and Leppert can be successfully correlated with Eq. 53. Hence, Eq. 53 is a general correlation based upon physical properties, yet it is accurate for water at atmospheric pressure. Equation 53 will be used here for this reason.

Correlations such as Eqs. 44-53, which relate CHF to flow conditions, are independent of ΔT_x because the CHF is a hydraulic limitation. Berenson reported that surface conditions affected the surface temperature but not the heat flux at burnout.⁶ Corrosion increases the surface temperature for a given heat flux during nucleate boiling and at the CHF.⁷⁷ Gaertner²⁴ and Stock⁶² reported ΔT_x at the CHF for atmospheric water to be 79 and 43°F, respectively. Both sets of data were taken from freshly polished surfaces. Jens and Lottes³⁶ correlated the surface temperature at CHF for water from 100 to 2500 psia as

$$\Delta T_x|_{CHF} = 60 \left[\frac{\varphi_{CHF}}{10^6} \right]^{1/4} \exp \left(\frac{P}{900} \right). \quad (54)$$

This expression was modified by Weatherhead^{76,77} to include data to 60 psia as

$$\Delta T_x|_{CHF} = (0.18 \cdot 10^6)(500 - 0.707T_{sat})10^{-6} \left(\frac{q_{CHF}}{10^6} \right)^{1/4}. \quad (55)$$

For the calculation done here, Eqs. 53 and 55 will be used to determine the location of the CHF point.

F. Sample Calculation

The purpose of this chapter has been to propose a method for obtaining the heat-transfer coefficient in a sputtering front. Numerous correlations

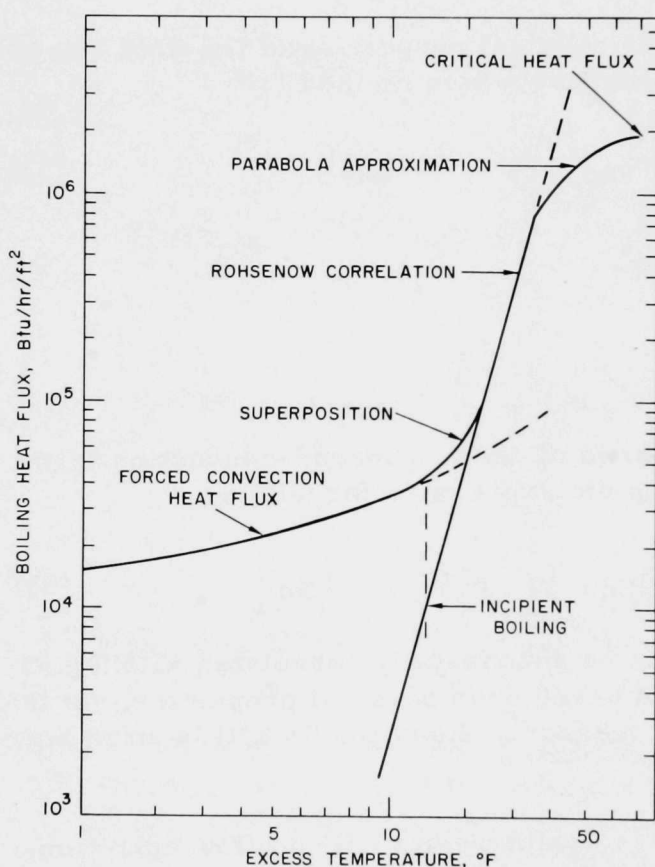


Fig. 19. Subcooled Forced-convection Boiling Heat Flux up to CHF. ANL Neg. No. 900-75-874.

have been discussed where the heat-transfer coefficient or the heat flux is a function of flow conditions. Figure 19 shows the results of linking these correlations together according to the procedure already described. This procedure is a logical method for joining Regions 1, 2, and 3 to form this curve, which is the same as the curve in Fig. 2 up to the CHF point. Probably the best way to summarize this chapter is to illustrate this procedure with an example.

Example

Consider sputtering under the following flow conditions:

$$\Gamma = 968 \text{ lb}_m/\text{hr-ft};$$

$$T_{liq} = 173^\circ\text{F};$$

$$T_{sat} = 211^\circ\text{F}.$$

For this example, the water temperature will be assumed to be constant. Actually, the water tem-

$$h_c = \frac{\text{total heat flux}}{\text{total temperature difference}}. \quad (56)$$

Step 1

In Region 1, the heat-transfer coefficient can be determined from Eqs. 24-27. Figure 18 shows calculations for 150°F water, which is lower than in the present case. The value at 173°F is about 2000 Btu/hr-ft²-°F.

Step 2

Region 1 ends when the surface temperature reaches the incipient-boiling temperature. The incipient heat flux can be estimated from Eq. 28, which reduces to

$$\varphi_{\text{incip}} = 337\Delta T_x^{2.16}. \quad (57)$$

To find the incipient-boiling temperature, an iterative solution is required. If we guess that $\Delta T_{x,bi} = 15^\circ\text{F}$, then $\varphi_{\text{incip}} = 118,000$ Btu/hr-ft². Since the actual heat flux at this temperature is less than the incipient-boiling heat flux $\{\varphi_{fc} = h_c\Delta T = (2000 \text{ Btu/hr-ft}^2\text{-}^\circ\text{F})[(211 + 15 - 173)^\circ\text{F}] = 106,000 \text{ Btu/hr-ft}^2\}$, 15°F is too high. A guess that $\Delta T_{x,bi} = 14^\circ\text{F}$ reduces φ_{incip} to 104,000 Btu/hr-ft² and $\varphi_{\text{incip}} = \varphi_{fc}$, so that $\Delta T_{x,bi}$ has been found. Therefore, Region 2 starts when the surface temperature is 225°F (211 + 14°F).

Step 3

The third step is to find the CHF, which is done by using the principle of superposition and the general pool-boiling CHF of Collier. For water at atmospheric pressure, Eq. 52 reduces to

$$\varphi_{\text{CHF,pb}} = (113.25 + 3.85\Delta T_{\text{sub}}), \quad (58)$$

and the total CHF is, by superposition,

$$\varphi_{\text{CHF}} = \varphi_{\text{CHF,pb}} + h_{c|\text{falling film}}(T_{\text{sur}} - T_{\text{liq}}). \quad (59)$$

To solve this, T_{sur} must be known, which is obtained from Eq. 55, which at 14.3 psia reduces to

$$\Delta T_x = 63 \left(\frac{\varphi_{\text{CHF}}}{10^6} \right)^{1/4}. \quad (60)$$

Again an iterative process is required, and the results are $\Delta T_x = 62.6^\circ\text{F}$ and $\varphi_{\text{CHF}} = 973,000$ Btu/hr-ft².

Step 4

The superposition method, Eq. 30, is used to determine the heat flux in Region 2 up to the point where $\varphi = 0.6 \varphi_{\text{CHF}}$. In using the superposition method, the heat flux due to forced convection is determined as

$$\varphi_{fc} = (h_c|_{\text{falling film}})(\Delta T_{\text{total}}),$$

and the pool-boiling component is determined as from Eq. 41.

Step 5

When the heat flux is 0.6 CHF, the parabola approximation is begun. In this example, this occurs when $T_{\text{sur}} = 245.1^\circ\text{F}$. If the parabola is of the form of Eq. 43, the following equations must be satisfied:

$$0.6 \varphi_{\text{CHF}} = A\Delta T_{x_1}^2 + B\Delta T_{x_1} + C; \quad (61a)$$

$$\varphi_{\text{CHF}} = A\Delta T_{x_2}^2 + B\Delta T_{x_2} + C; \quad (61b)$$

$$0 = 2A\Delta T_{x_2} + B, \quad (61c)$$

where

$$\Delta T_{x_1} = (T_{\text{sur}} - T_{\text{sat}})|_{0.6\text{CHF}}$$

and

$$\Delta T_{x_2} = (T_{\text{sur}} - T_{\text{sat}})|_{\text{CHF}}.$$

Upon solving for A, B, and C, Eq. 42 is used up to CHF. At this point, the heat-transfer coefficient is assumed zero and the curve is completed.

The present chapter has dealt with the details of calculating the heat-transfer coefficient through a sputtering front. When the sputtering is considered as being composed of three regions, heat-transfer correlations based upon local conditions could be linked together to form a continuous heat-transfer-coefficient curve. These three regions are:

Region 1: a quiescent falling film, Eqs. 24-27;

Region 1-2 interface: incipient boiling, Eq. 28;

Region 2A: forced-convection boiling by superposition, Eq. 30;

Region 2B: approach to CHF by parabola approximation, Eq. 43;

Region 2-3 interface: CHF, Eq. 44;

Region 3: adiabatic, $h_c = 0$.

Such a method is necessary since no single heat-transfer-coefficient correlation covers the entire boiling map. Several heat-transfer coefficients for each region were presented, and a recommended one for each region was chosen.

VI. EXPERIMENTAL DATA AND COMPARISON WITH ANALYSIS

The last chapter addressed the problem of calculating the heat-transfer coefficient through a sputtering front and a method was proposed for doing this based upon local conditions along the solid surface. The only assumptions in the development of this method were: (1) the sputtering front corresponds to a CHF phenomena, and (2) the surface below the sputtering front is adiabatic. This chapter will present experimental evidence proving the validity of these two assumptions. In the development of this method, an arbitrary constant existed that corresponds to the point on the boiling map where the Rohsenow correlation terminated and the parabola approximation began. Sensitivity studies showing the effect of various values for this constant as well as three different pool-boiling correlations will be presented. Experimental and calculated temperature profiles for five test cases showing the extremes of the data will be shown in detail. Finally, by means of a coordinate transformation, reported sputtering data for a moving front will be predicted by using a simplified version of the heat-transfer-coefficient curve.

A. Sputtering-front Temperature

One of the major objectives of this study was to estimate the sputtering-front temperature. In either a stationary or moving sputtering front, this is the surface temperature at the lowest wetted position. In other words, it is the highest surface temperature at which the rod is still wet. It was shown in Ch. II that this temperature has been measured or estimated from as low as 280°F (138°C) to as high as 500°F (260°C) for water at atmospheric pressure. Surface temperatures of 280°F generally correspond to CHF, whereas 500°F is more characteristic of film boiling. As shown in Ch. V, a knowledge of the sputtering temperature is necessary for predicting the heat-transfer coefficient. At surface temperatures less than the sputtering temperature, the surface is wet and the surface heat flux can be large. From an examination of the one-dimensional energy equation, Eq. 13, a significant surface heat flux will cause a change in the axial temperature gradient. Therefore, the sputtering temperature can be estimated by examining the temperature profiles and determining the lowest temperature at which the gradient begins to change (see Fig. 20).

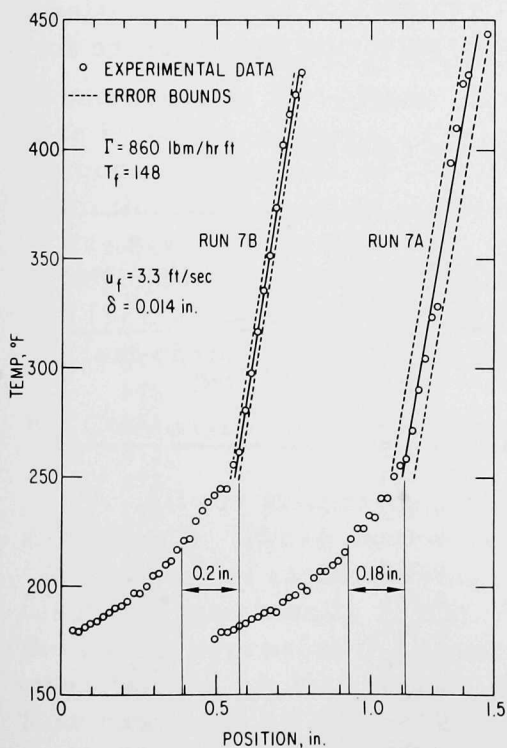


Fig. 20. Least-squares Correlation for Runs 7A and 7B. ANL Neg. No. 900-75-875.

A problem in using this method is the possible existence of a significant surface heat flux in the dry zone. There are two possible heat-transfer mechanisms here: radiation and convection. For the data obtained here, the dry zone was short, usually about 1/4 in. (0.64 cm), and the measured peak temperature was less than 600°F (315°C). In this temperature range, radiation can be neglected. The convection heat flux would be at most of the order of 6000 Btu/hr-ft² (1.89 W/cm²). Again, by use of the one-dimensional energy equation this heat flux can be seen to have only an insignificant effect (<1%) on the temperature gradient. Such an analysis shows a constant temperature gradient can be physically justified only in the dry zone.

The temperature gradient in the dry zone was obtained by fitting a straight line through the data in a least-squares sense; the solid lines of Fig. 20 are the fitted lines. Inspection of all of the temperature profiles showed that at temperatures greater than 300°F (149°C) all the data appeared as straight lines. Therefore, a 300°F cutoff point was selected when correlating the data to avoid attempting to correlate a straight line through a curve. The standard error and 95% confidence bounds (dashed lines of Fig. 20) were also calculated. For the data obtained here, the experimental sputtering-front temperature is defined as that temperature at which the data begin to deviate from the fitted straight line. This corresponds to the highest temperature at which a significant heat flux is observed and the lowest wetted position of the rod. Table I lists the experimental sputtering temperature, 95% confidence band, correlation coefficient (an explanation of these statistical terms is given in Appendix F), and calculated sputtering temperature for all the data obtained here.

TABLE I. Comparison of Experimental and Calculated Sputtering Temperatures

Run No.	T _{sput} Experimental, °F	95% Confidence Band, °F	Correlation Coefficient	T _{sput} Calculated, °F
1	267	±6	0.999	272
2	265	±6	0.997	274
3	274	±39	0.982	272
4	267	±26	0.975	278
5	250	±11	0.993	278
6	259	±12	0.999	277
7A	260	±33	0.970	277
7B	258	±14	0.992	277
8A	215	±32	0.986	280
8B	245	±18	0.984	280
9	260	±14	0.986	278
10	295	±38	0.970	277
11	240	±14	0.988	287
12	285	±25	0.988	284
13	250	±20	0.967	282
14	280	±25	0.984	281
15	305	±42	0.957	285
16	290	±18	0.972	283

These results are shown graphically in Fig. 21, where the vertical bars represent the 95% confidence bounds of the sputtering temperature and the horizontal bars represent the experimental uncertainty.

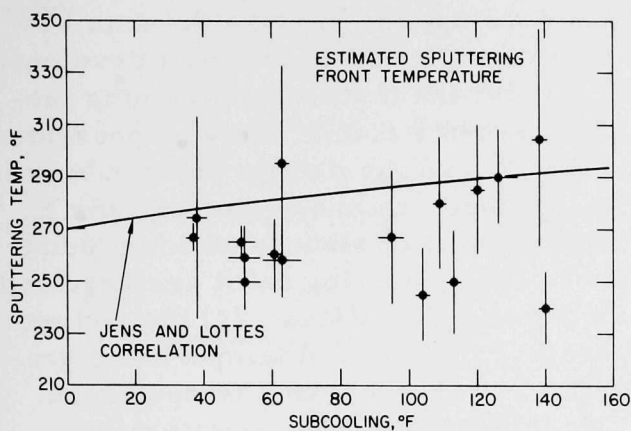


Fig. 21. Comparison of Measured Sputtering-front Temperatures and Jens-Lottes Correlation. ANL Neg. No. 900-75-876.

It can be seen in Fig. 21 that the measured sputtering temperature is in good agreement with the Jens-Lottes correlation. The correlation shown in Fig. 21 is approximate because ΔT_x is a function of CHF which is, in turn, a function of subcooling and flow rate. However, ΔT_x is a weak function ($1/4$ power) of CHF, and the estimate in this figure is within 20°F (11°C). If the sputtering front coincided with film boiling, the temperature would be the minimum temperature for stable film boiling. These temperatures have been estimated at 380°F

(190°C) and 450°F (232°C) for water at atmospheric pressure.^{6,32} Even if one considers the uncertainty in the CHF correlation and the experimental uncertainty, temperatures corresponding to stable film boiling cannot be justified. Further experimental evidence that the sputtering front corresponds to a CHF phenomenon is that these data are reproducible, as shown in Figs. 20 and F.1.

A physical argument that the sputtering front corresponds to a CHF phenomenon is as follows: The falling liquid film is displaced from the surface by a lateral force. The only source of such a force is nucleation, which reaches a maximum at CHF. Once the falling liquid film has been displaced from the surface, it does not return since the only force acting on the liquid is gravity. These facts--(1) the minimum temperature for stable film boiling is beyond the range of experimental uncertainty, (2) the data are reproducible, and (3) the maximum lateral force exists at CHF--justify the assumption in the last chapter that the sputtering front corresponds to a CHF phenomenon.

B. Comparison of Experimental Data and Calculations

All the stationary-sputtering-front data obtained here is listed in Appendix B. These data were taken for water subcoolings varying from 40 to 140°F and flow rates varying from 350 to $1600 \text{ lb}_m/\text{hr-ft}$. These ranges are displayed graphically in Fig. 22, where the vertical and horizontal lines through the points represent the experimental uncertainty in flow rate and subcooling, respectively. A lack of data for the combination of high subcooling and high flow rates can be seen in the figure. The reason for this is that a stationary sputtering could not be maintained during these flow conditions. The heat-removal rate of such a sputtering front was greater than the maximum electrical power that could be supplied to the test section.

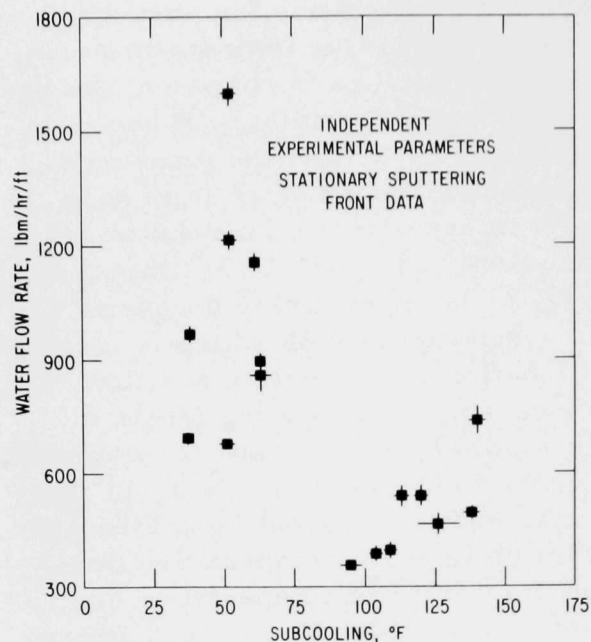


Fig. 22. Range of Experimental Data.
ANL Neg. No. 900-5484.

A two-dimensional nonlinear model of a stationary sputtering front was developed to analyze the data obtained here. This model was developed in Ch. IV, the method of obtaining the heat-transfer coefficient was presented in Ch. V, and the details of the numerical method are shown in Appendix E. Three initial conditions at some point above the sputtering front are required for these calculations: (1) the rod temperature, (2) the rod temperature gradient, and (3) the water temperature. Two other parameters--water flow rate and condensation heat flux--are also required and were assumed to be constant along the length of the rod. All of these values were obtained from the data and used in the calculations. The experimental temperature profiles are compared to the calculated tem-

perature profiles for both surface and centerline in Figs. 23-27 for five test cases. In these figures, data were taken for three different stepping intervals: 0.020, 0.050, and 0.100 in. (0.05, 0.127, and 0.254 cm), and the calculated sputtering front (location of CHF) is indicated by a double-ended arrow. The reason that data in Figs. 24 and 25 appear to be truncated is that most of the

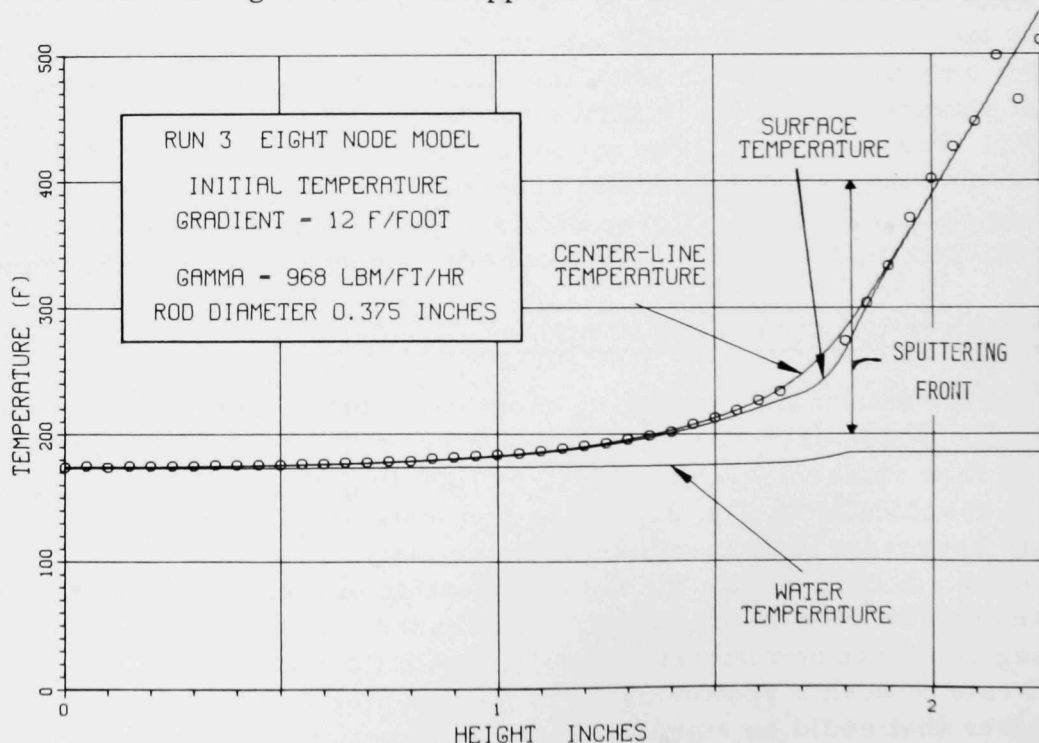


Fig. 23. Calculated and Measured Temperature Profiles for Run 3. ANL Neg. No. 900-75-878.

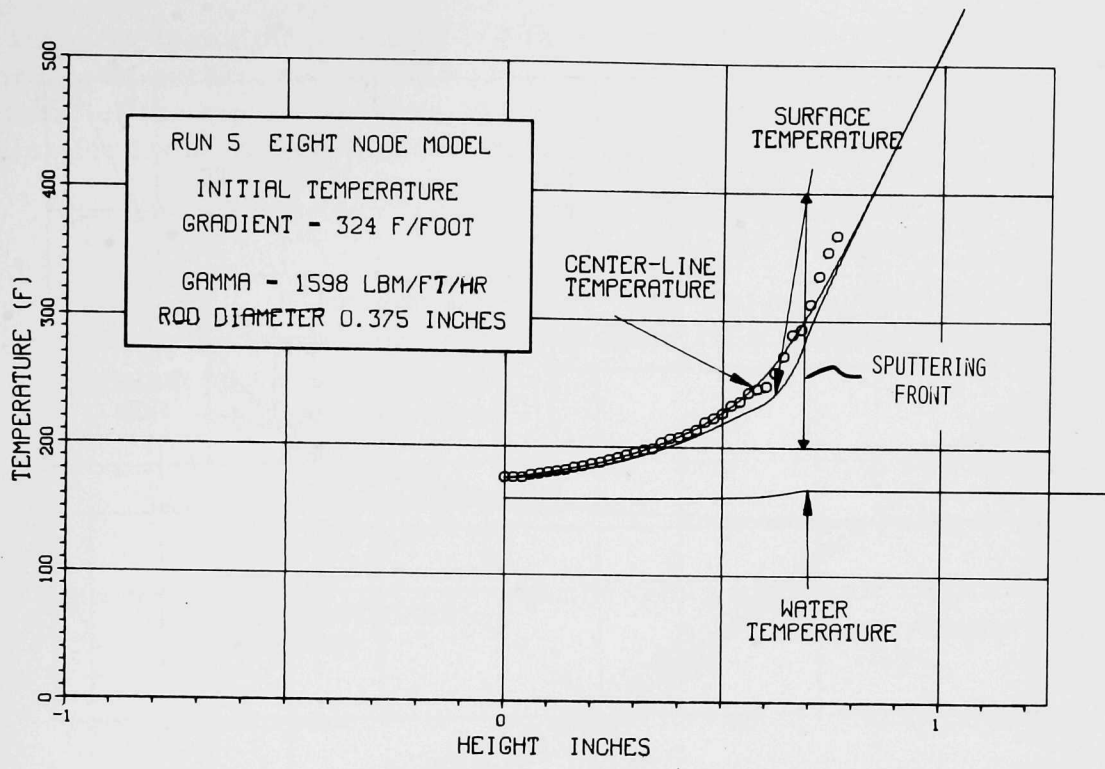


Fig. 24. Calculated and Measured Temperature Profiles for Run 5. ANL Neg. No. 900-75-879.

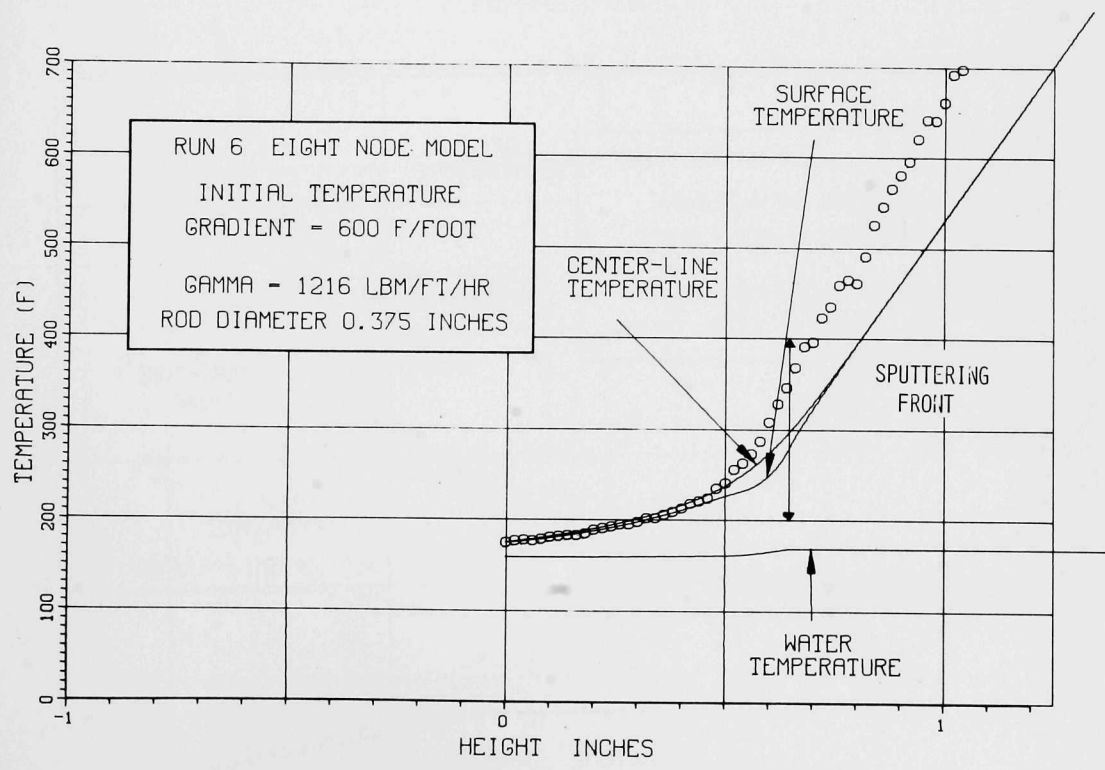


Fig. 25. Calculated and Measured Temperature Profiles for Run 6. ANL Neg. No. 900-75-880.

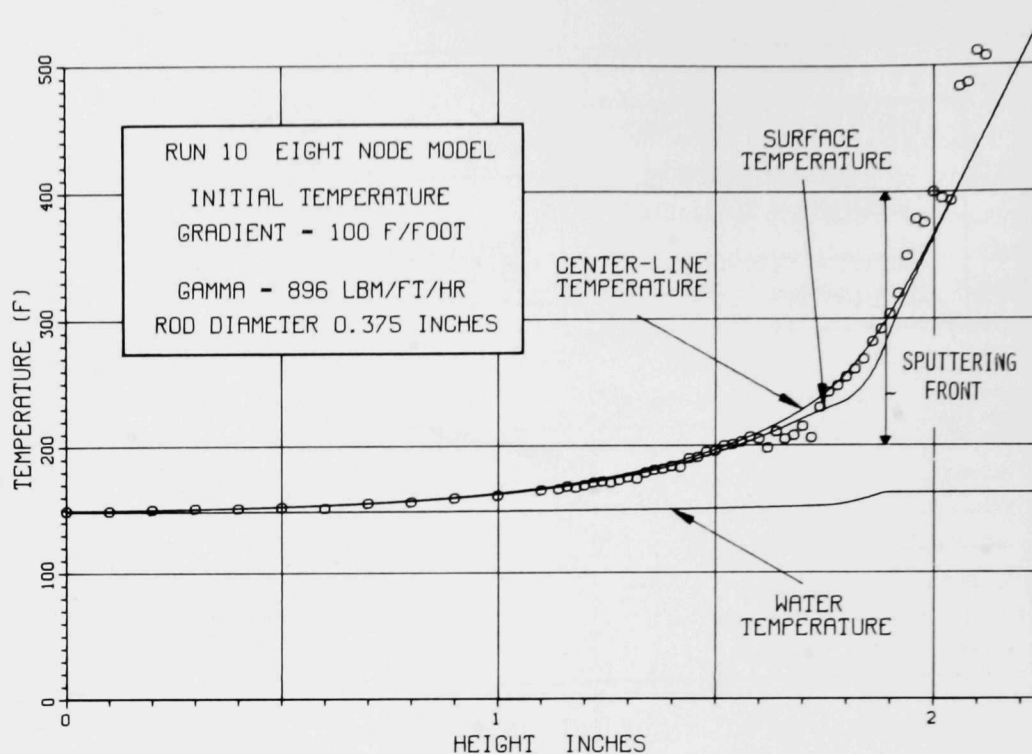


Fig. 26. Calculated and Measured Temperature Profiles for Run 10. ANL Neg. No. 900-75-881.

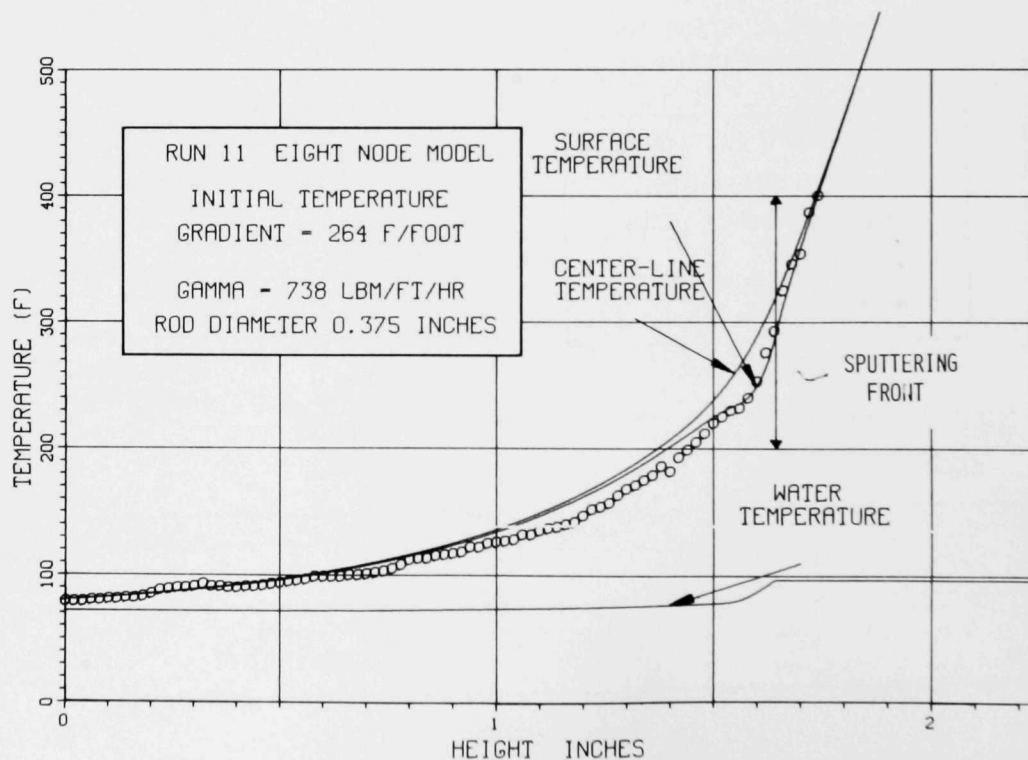


Fig. 27. Calculated and Measured Temperature Profiles for Run 11. ANL Neg. No. 900-75-882.

heat transfer takes place within 1/2 in. (1.27 cm) of the sputtering front. Recording of surface temperatures were terminated when it was believed that most of the significant data had already been recorded. Temperature profiles for these five test cases can be seen in greater detail in Figs. 28-32.

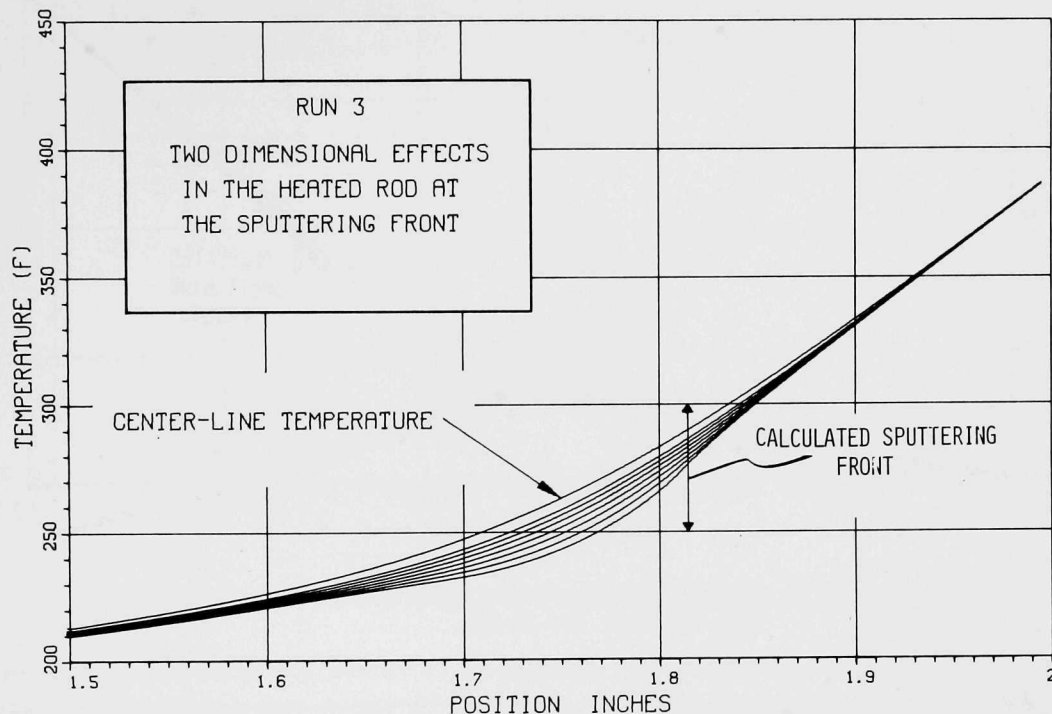


Fig. 28. Two-dimensional Temperature Profiles for Run 3. ANL Neg. No. 900-75-883.

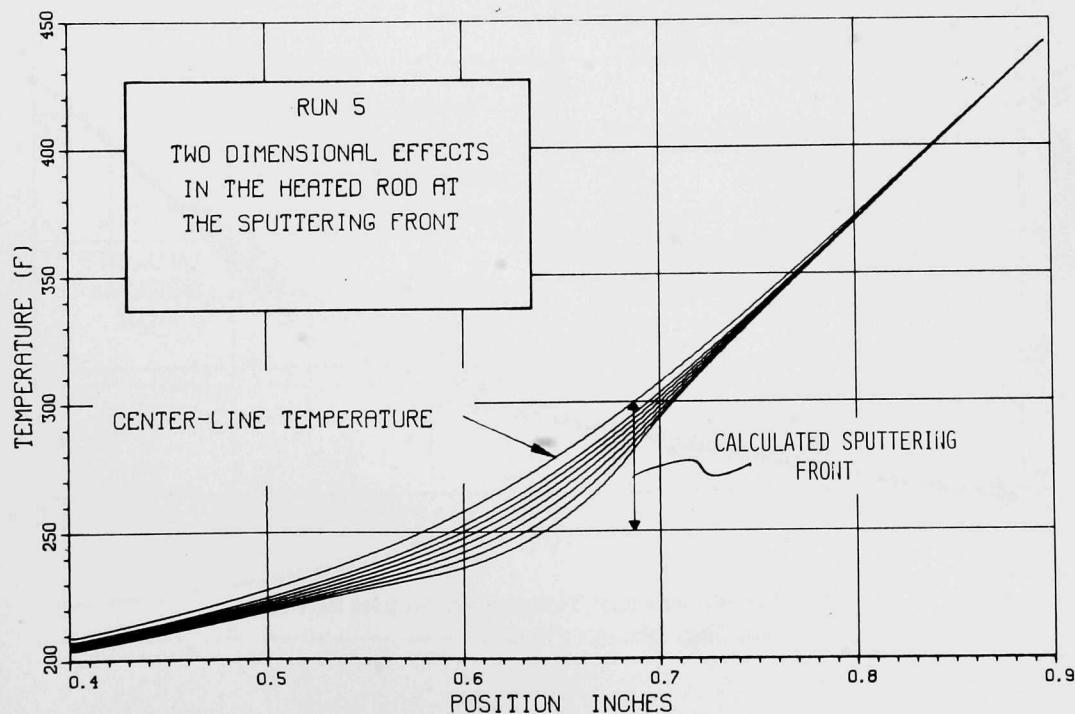


Fig. 29. Two-dimensional Temperature Profiles for Run 5. ANL Neg. No. 900-75-884.

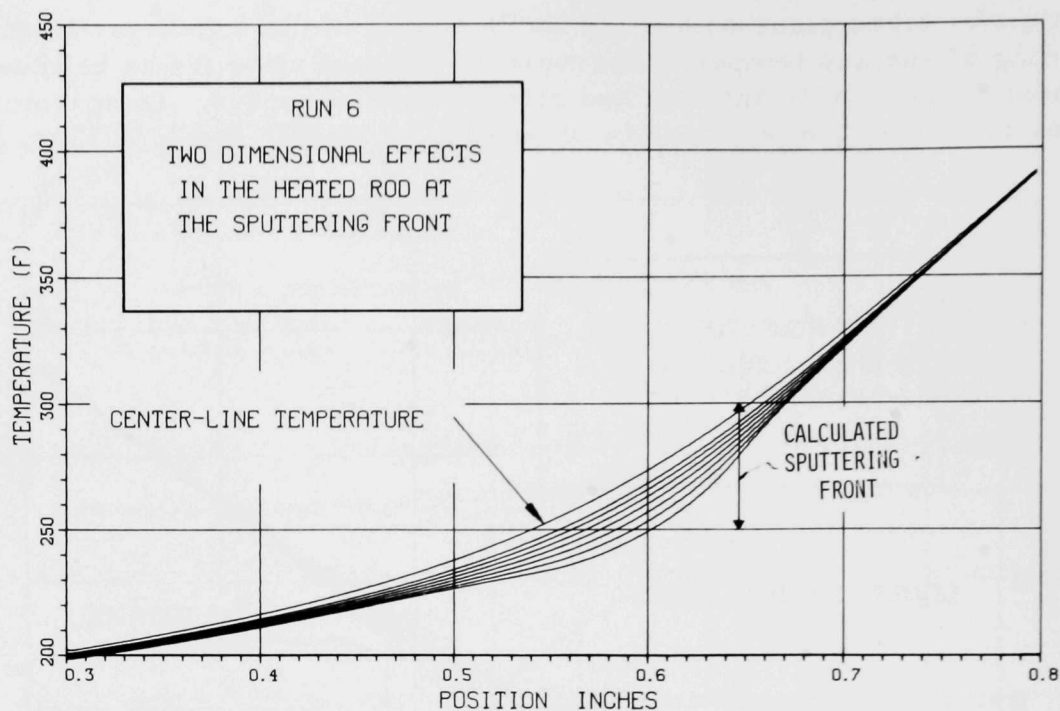


Fig. 30. Two-dimensional Temperature Profiles for Run 6.
ANL Neg. No. 900-75-885.

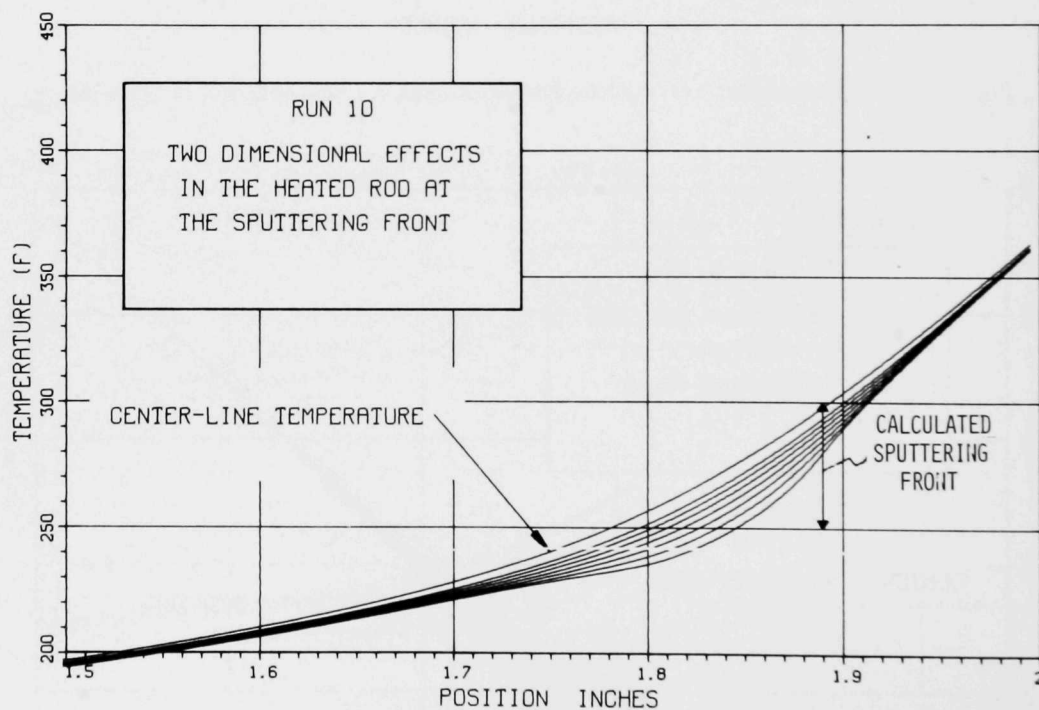


Fig. 31. Two-dimensional Temperature Profiles for Run 10.
ANL Neg. No. 900-75-886.

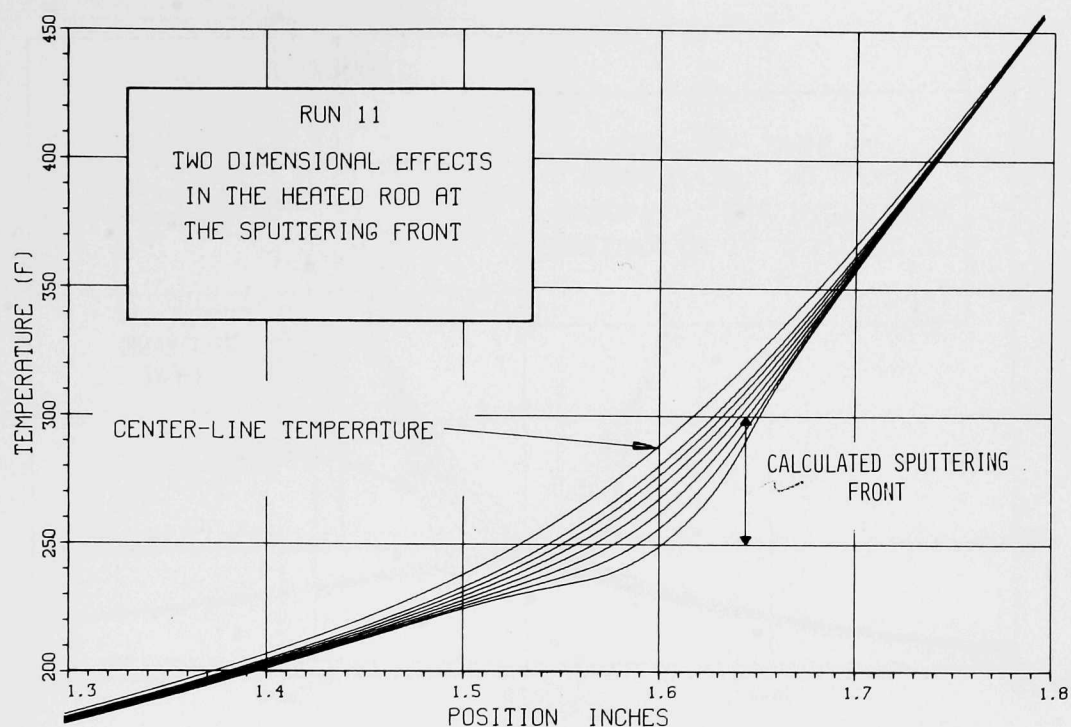


Fig. 32. Two-dimensional Temperature Profiles for Run 11. ANL Neg. No. 900-75-887.

The calculated sputtering front is indicated by a vertical arrow; the calculated temperature profiles for eight different radial locations are shown for the rod near the sputtering front. Two-dimensional effects are even more evident from Figs. 33-37, which detail the axial temperature gradient for the eight

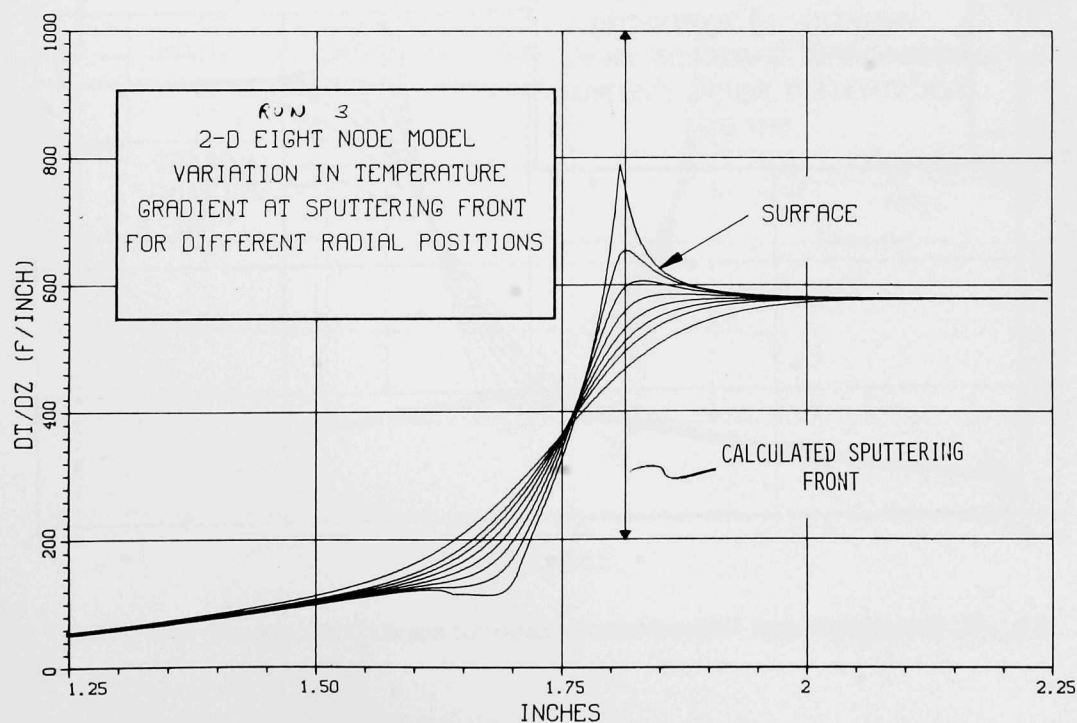


Fig. 33. Two-dimensional Temperature Gradients for Run 3. ANL Neg. No. 900-75-888.

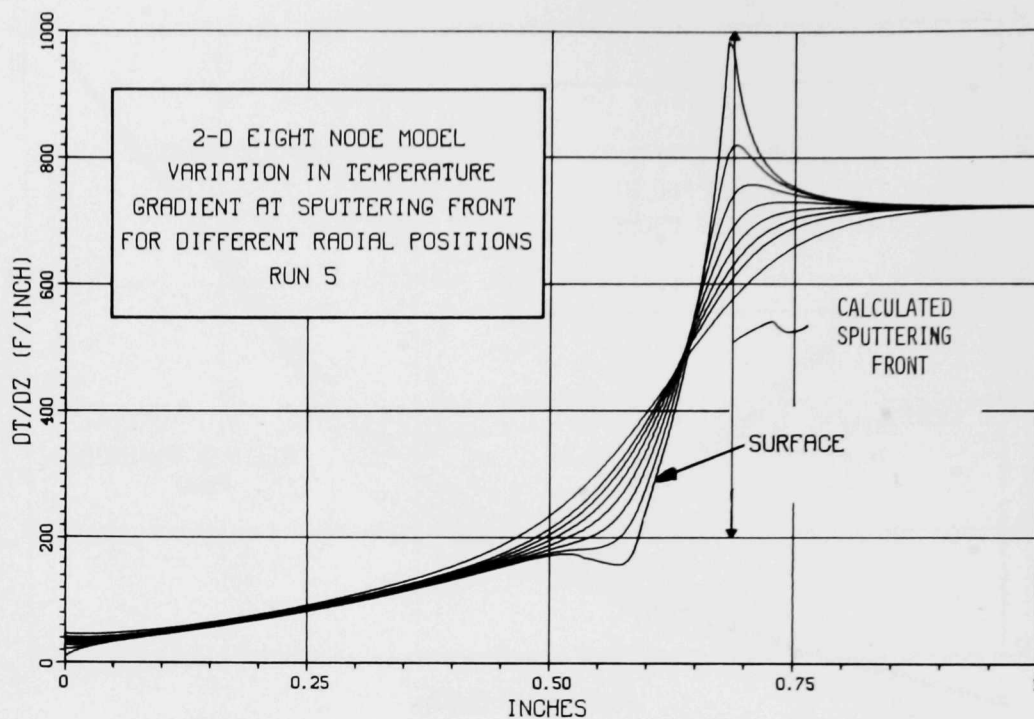


Fig. 34. Two-dimensional Temperature Gradients for Run 5. ANL Neg. No. 900-75-889.

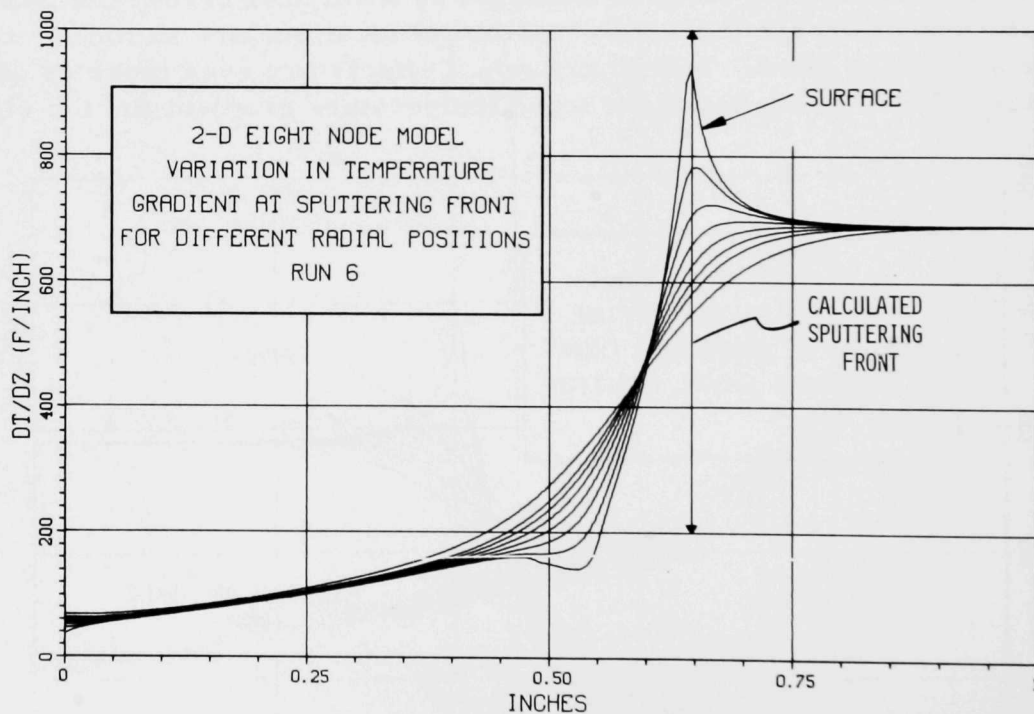


Fig. 35. Two-dimensional Temperature Gradients for Run 6. ANL Neg. No. 900-75-890.

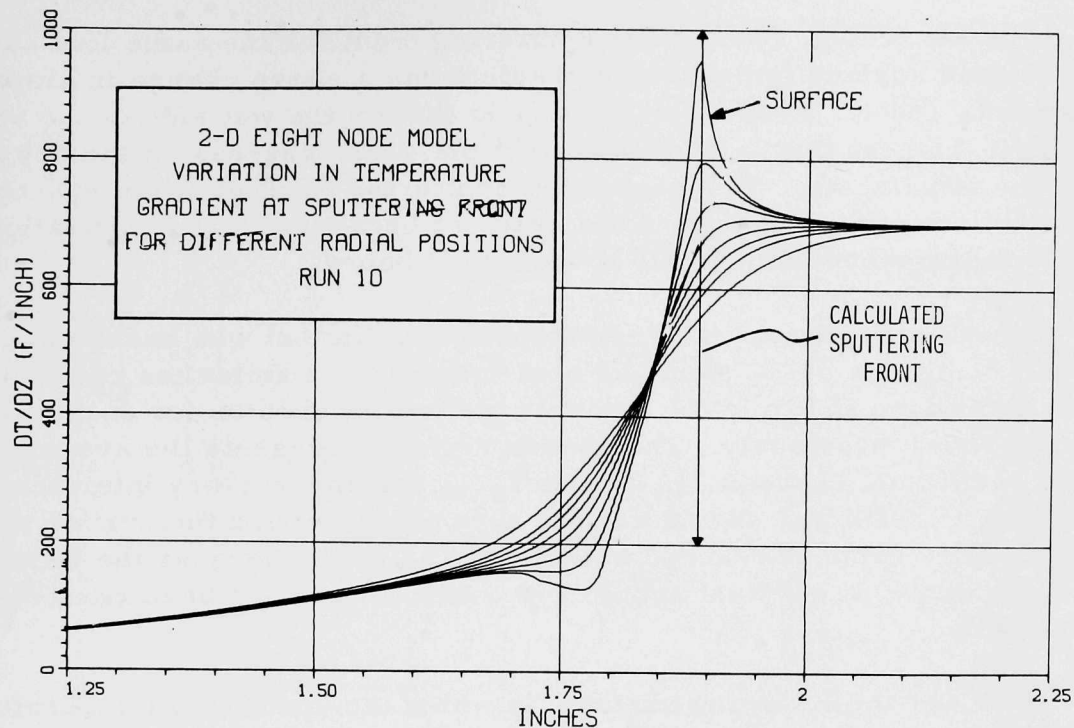


Fig. 36. Two-dimensional Temperature Gradients for Run 10. ANL Neg. No. 900-75-891.

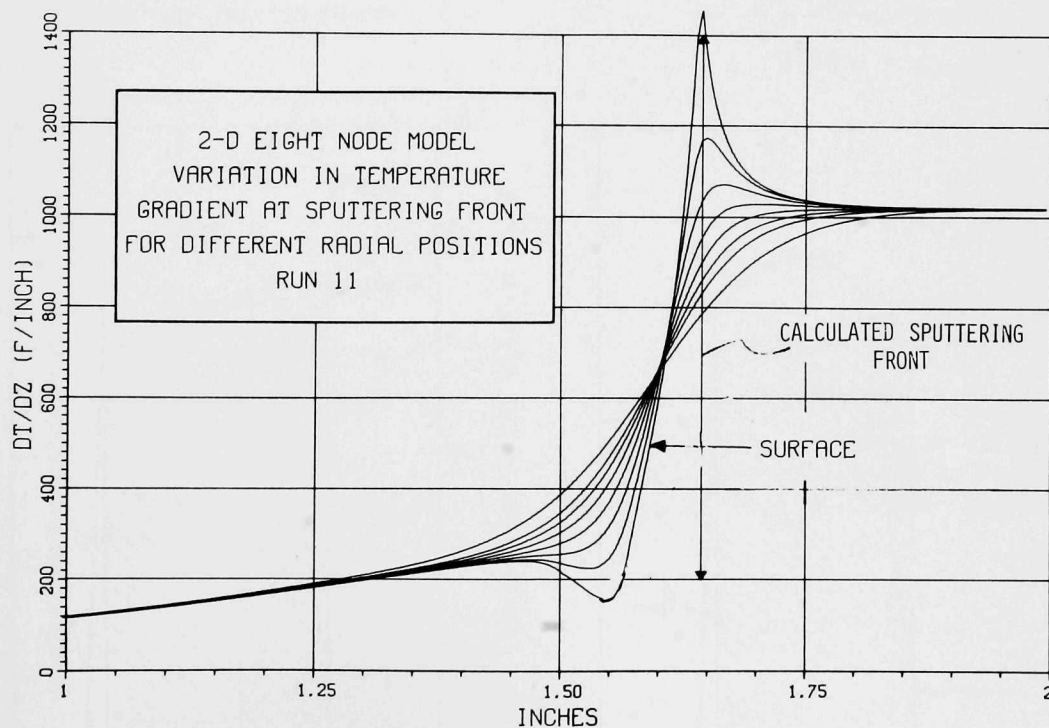


Fig. 37. Two-dimensional Temperature Gradients for Run 11. ANL Neg. No. 900-75-892.

radial locations of Fig. 13 near the sputtering front for the same five cases. The calculated surface temperature gradient has a sharp change in slope at the sputtering front. The reason for this is that on the wet side of the sputtering front the heat flux is approximately the CHF, whereas on the dry side the surface is adiabatic. The calculated sputtering front does not exactly coincide with the sharp change in the gradient because of a simplification in the numerical method, which will be explained below.

For all calculations the heat-transfer coefficient was based upon local conditions. Figures 38-42 show the heat-transfer coefficient as calculated with the procedure shown in the example of the last chapter for each of five test cases shown previously. The shaded region represents the average heat-transfer coefficient between T_{incip} and T_{sput} . At the wet-dry interface the heat-transfer coefficient should drop to zero abruptly, and the curves show an intermediate value is reached before zero. This is because the finite-element technique of constant properties within a node has been relaxed at this boundary.

Consider the following example in which the sputtering temperature is 280°F and the temperature of the surface nodes are:

$$T_{\text{node } 1} = 278^{\circ}\text{F};$$

$$T_{\text{node } 2} = 282^{\circ}\text{F};$$

$$T_{\text{node } 3} = 287^{\circ}\text{F}.$$

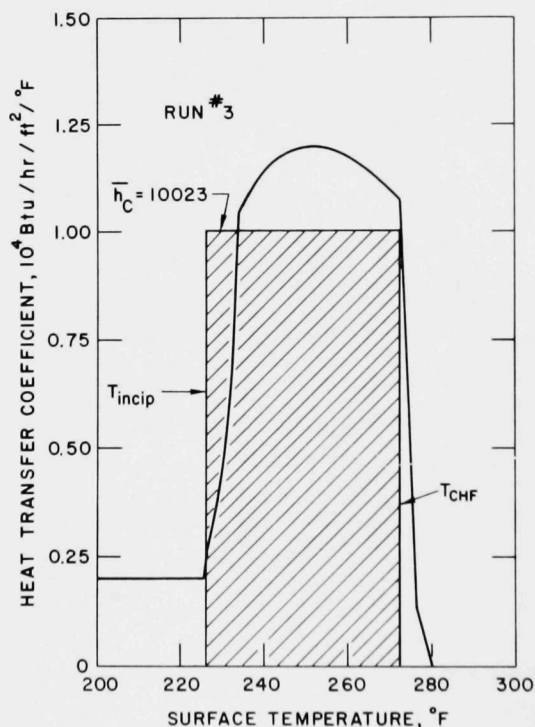


Fig. 38. Heat-transfer Coefficient as a Function of Surface Temperature for Run 3.
ANL Neg. No. 900-75-893.

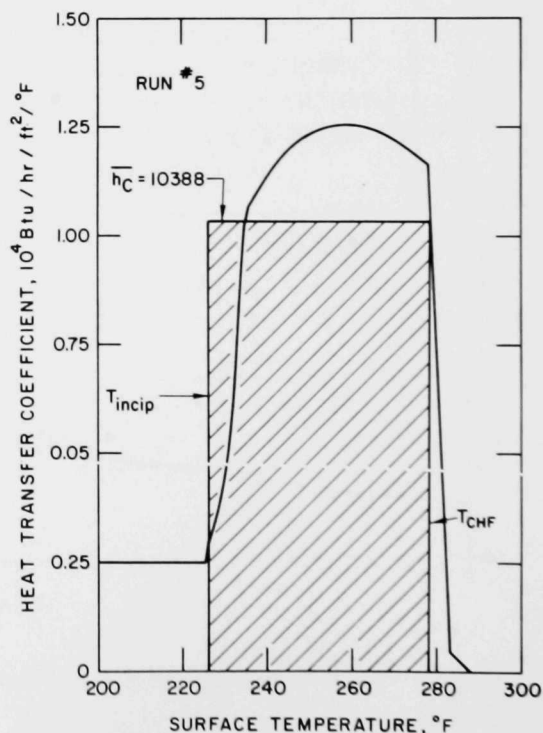


Fig. 39. Heat-transfer Coefficient as a Function of Surface Temperature for Run 5

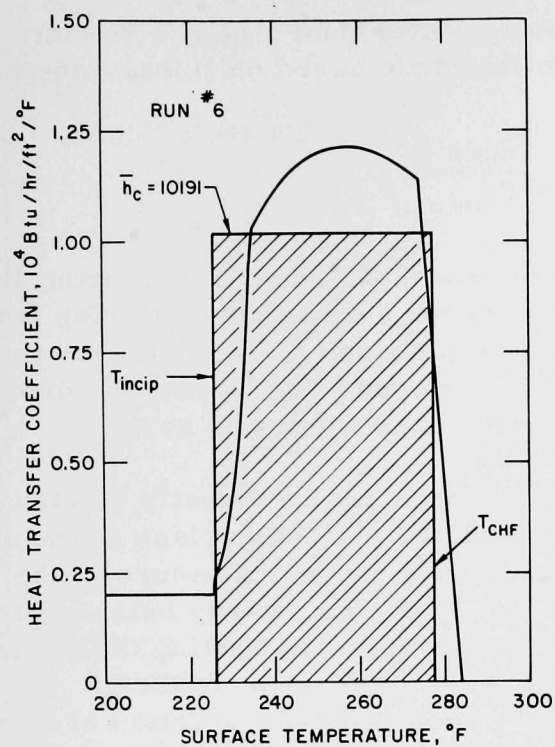


Fig. 40. Heat-transfer Coefficient as a Function of Surface Temperature for Run 6. ANL Neg. No. 900-75-895.

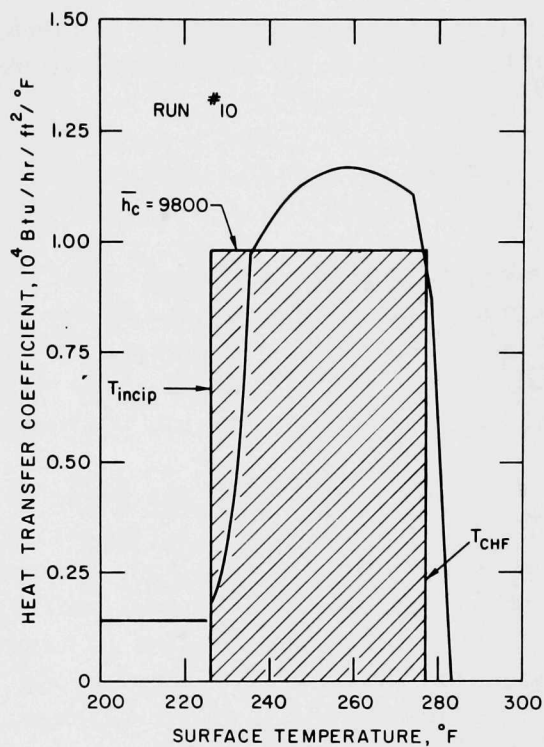


Fig. 41. Heat-transfer Coefficient as a Function of Surface Temperature for Run 10. ANL Neg. No. 900-75-896.

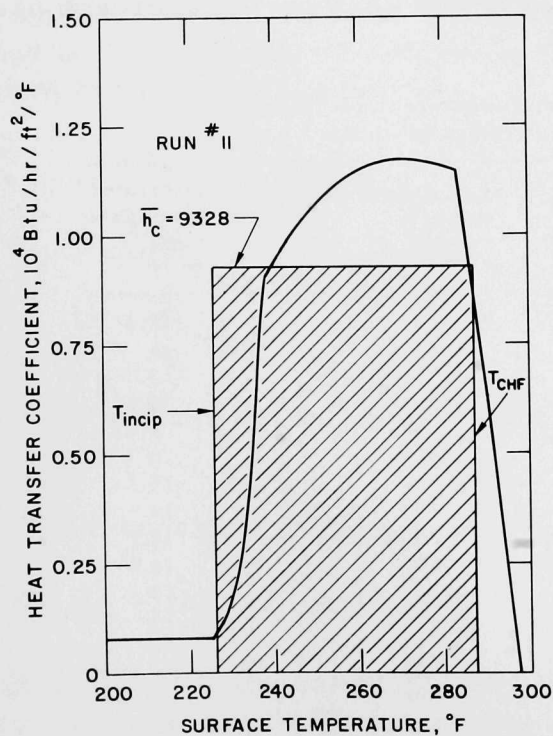


Fig. 42
Heat-transfer Coefficient as a Function of Surface Temperature for Run 11. ANL Neg. No. 900-75-897.

Even though the temperature of node 2 was greater than T_{sput} , a nonzero heat-transfer coefficient was assigned to this node based on linear interpolation:

$$h_c|_{\text{node 2}} = h_c|_{\text{node 1}} \left(\frac{T_{\text{sput}} - T_{\text{node 1}}}{T_{\text{node 2}} - T_{\text{node 1}}} \right). \quad (62)$$

This approximation eliminates the requirement that the sputtering front lies on a node boundary and caused the location of the calculated sputtering front in Figs. 33-37 to not lie precisely on the sharp change in axial surface temperature gradient. For all of these figures the sputtering front was considered to be the first node at which the heat-transfer coefficient was zero.

The temperature gradients in the dry zone can be directly related to the heat-removal rate of a sputtering front. Hence, a comparison of the measured and calculated dry-zone temperature gradients is a measure of the overall goodness of the model (see Table II). A simple energy balance in which zero net vapor release is assumed was used in calculating the water temperature rise in passing through a sputtering front (see Table II). Calculated estimates of net vapor released⁴⁵ have shown that the fraction of thermal energy that can be associated with vapor released is negligible. Although nucleate boiling, and hence vapor production, are evident near the sputtering front, most of the bubbles condense in the falling liquid film. Figure 43 graphically summarizes the comparison of data and calculations; most of the data lie within $\pm 20\%$ of the calculated values. When one considers the accuracy of most heat-transfer correlations ($\sim \pm 25\%$) this engineering approach has resulted in very good agreement with the data.

TABLE II. Comparison of Measured and Calculated Dry-zone Temperature Gradients

Run No.	Measured ^a $\frac{dT_{\text{rod}}}{dz} \Big _{\text{dry}}$	Calculated ^a $\frac{dT_{\text{rod}}}{dz} \Big _{\text{dry}}$	Calculated Temp Rise $\Delta T_{\text{liq}},$ °F
1	764	681	12.4
2	530	612	18
3	612	578	13
4	833	732	39.5
5	760	722	8.4
6	894	689	10
7A	843	704	14.5
7B	910	704	14.5
8A	931	800	34.7
8B	927	800	34.7
9	872	731	12
10	943	702	14
11	1045	1018	16
12	1089	900	31.0
13	910	898	30.2
14	1169	840	38.5
15	1023	960	37
16	692	890	37

^a°F/in.

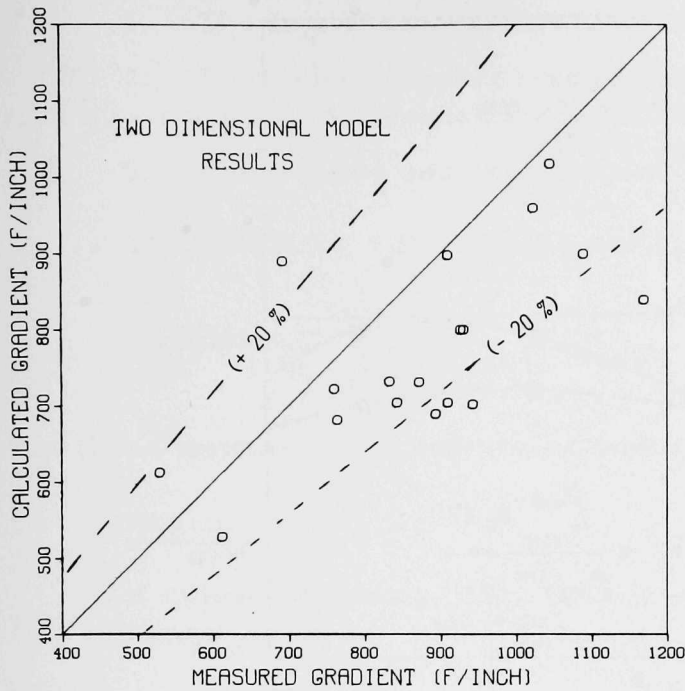


Fig. 43. Calculated and Measured Temperature Gradients. ANL Neg. No. 900-75-898.

C. Sensitivity Studies

In the synthesis of a heat-transfer coefficient throughout a sputtering front, various heat-transfer correlations for different local conditions were concatenated together to form a continuous heat-transfer-coefficient curve from nonboiling to the sputtering front. In the development of this curve, numerous correlations were presented with a considerable range in reported values. The range in pool-boiling heat-flux correlations is important because nucleate boiling accounts for the major fraction of the total heat removed by a sputtering front. A choice was made to adopt the Rohsenow correlation because it is the most widely used. The coefficients for

the correlation as recommended by Vachon were used because they were obtained in an unbiased least-squares sense for conditions closely approximated here. Three different pool boiling heat-flux correlations are shown in Eqs. 40-42. From Ch. V, it can be seen that these three correlations include most of the range of other boiling correlations. By defining the average heat-transfer coefficient for a sputtering front as

$$\bar{h}_c = \frac{\int_{T_{incip}}^{T_{CHF}} h_c(T) dT_{rod}}{\int_{T_{incip}}^{T_{CHF}} dT_{rod}}, \quad (63)$$

the effect of various boiling correlations on \dot{Q}_{total} and \bar{h}_c can be seen in Fig. 44.

The insensitivity of \dot{Q}_{total} can be explained as follows: Consider

$$\dot{Q}_{total} = (\bar{h}_c)(\Delta T_{total})(area). \quad (64)$$

It was observed that the calculated length, and hence the area of the nucleate-boiling zone, decreased with increasing boiling exponent. Since the average heat-transfer coefficient increased, the net effect was fairly small. When one considers the uncertainty in pool-boiling correlations, this insensitivity is encouraging.

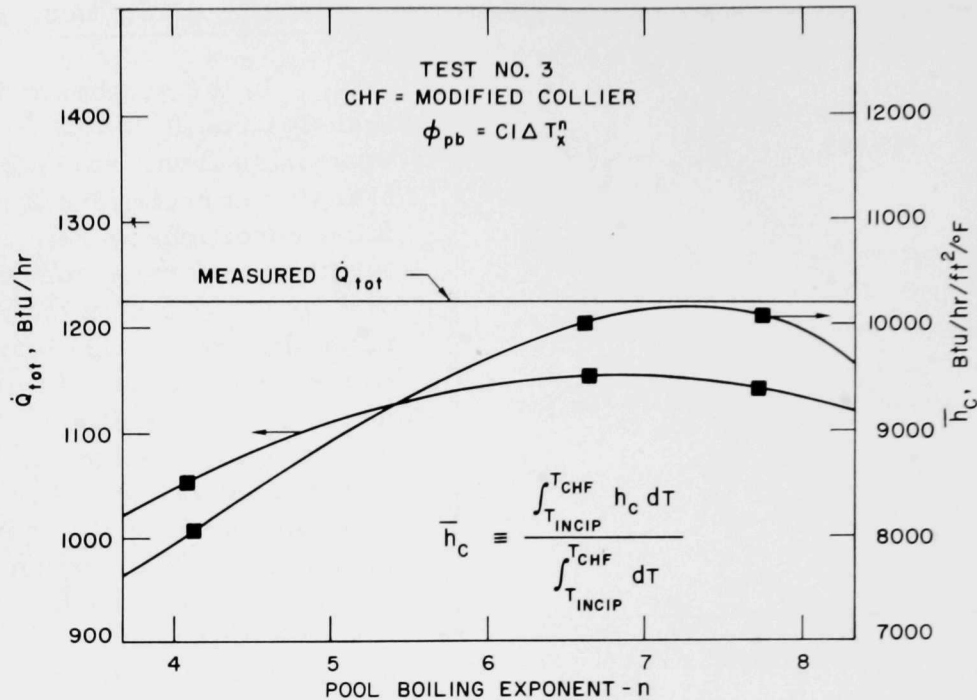


Fig. 44. Model Sensitivity to Pool-boiling Correlation. ANL Neg. No. 900-75-899.

The termination of the Rohsenow correlation and the beginning of the parabola approximation were shown in the last chapter to be arbitrary. Figure 45 shows the effect of various locations of this junction on \dot{Q}_{total} and \bar{h}_c , where the junction is referred to as breakpoint. This sputtering model has been based upon an engineering approach, and if it were a strong function of a particular pool-boiling correlation or arbitrary constant, its usefulness would be questionable.

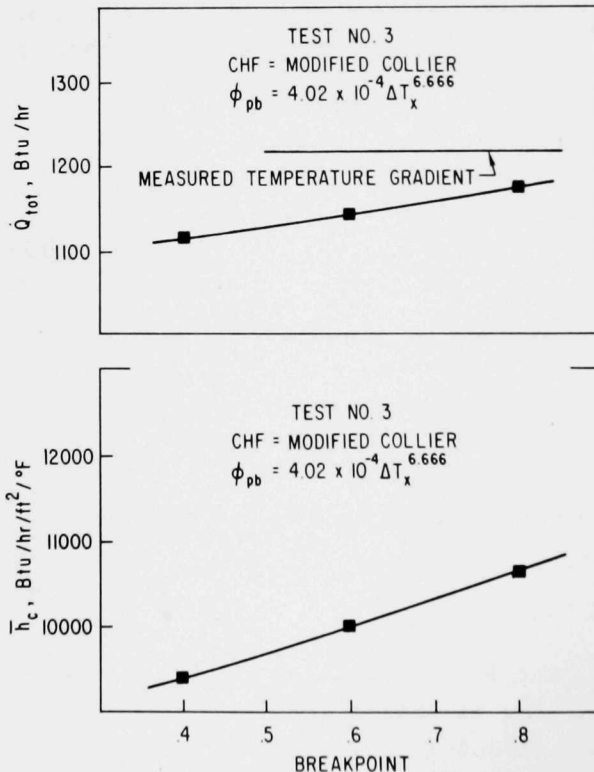


Fig. 45. Model Sensitivity to Breakpoint. ANL Neg. No. 900-75-900.

D. Simplified Analysis

The two-dimensional nonlinear model has shown good agreement with the data obtained here. The drawback of this model is that numerical methods are required, and computational facilities are expensive and not necessarily available. The analysis to be presented here is based on the physics of the process but with some simplifying assumptions. This analysis reduces to three second-order linear differential equations

1. The liquid temperature is constant.
2. Sputtering is a three-region process with each region characterized by a constant heat-transfer coefficient.
3. The rod has constant properties.

The governing differential equation, where positive z is downward, is

$$\frac{d^2 T_{\text{rod}}}{dz^2} = \frac{4h_c}{k_{\text{rod}} D_{\text{rod}}} (T_{\text{rod}} - T_{\text{liq}}). \quad (65)$$

The three regions of the rod are defined as:

Region 1

A quiescent falling liquid film extending from $-\infty < z < 0$. The surface temperature at $z = 0$ is T_{incip} .

Region 2

The nucleate-boiling zone extends from $z = 0$ to $z = \ell$, where ℓ is the unknown length of the nucleate-boiling zone. The temperature at $z = \ell$ is the CHF temperature.

Region 3

This region is adiabatic and extends from ℓ to ∞ . There are two boundary conditions for each region:

Region 1

$$\text{B.C. 1 at } z = -\infty: T_{\text{rod}} = T_{\text{liq}}; \quad (66a)$$

$$\text{B.C. 2 at } z = 0: T_{\text{rod}} = T_{\text{incip}}. \quad (66b)$$

Region 2

$$\text{B.C. 3 at } z = 0: T_{\text{rod}} = T_{\text{incip}}; \quad (66c)$$

$$\text{B.C. 4 at } z = 0: \frac{d}{dz} T_{\text{Region 1}} = \frac{d}{dz} T_{\text{Region 2}}. \quad (66d)$$

Region 3

$$\text{B.C. 5 at } z = \ell: T_{\text{rod}} = T_{\text{sput}}; \quad (66e)$$

$$\text{B.C. 6 at } z = \ell: \frac{d}{dz} T_{\text{Region 2}} = \frac{d}{dz} T_{\text{Region 3}}. \quad (66f)$$

The solution for Region 1 is

$$T_{\text{rod}} = (T_{\text{incip}} - T_{\text{liq}})e^{(\text{root}_1 z)} + T_{\text{liq}}, \quad (67)$$

where

$$\text{root}_1 = \sqrt{\frac{4h_c|_{fc}}{k_{\text{rod}}D_{\text{rod}}}}$$

and $h_c|_{fc}$ is determined from Eqs. 24-27, and T_{incip} is determined from Eq. 28.

The solution for Region 2 is

$$\begin{aligned} T_{\text{rod}} = & \frac{(T_{\text{incip}} - T_{\text{liq}})}{2 \text{root}_2} (\text{root}_1 + \text{root}_2) e^{(\text{root}_2 z)} \\ & + (\text{root}_2 - \text{root}_1) e^{(-\text{root}_2 z)}, \end{aligned} \quad (68)$$

where

$$\text{root}_2 = \sqrt{\frac{4\bar{h}_c}{k_{\text{rod}}D_{\text{rod}}}}$$

and \bar{h}_c is an average heat-transfer coefficient that can be associated with a sputtering front as defined in Eq. 63. The previous chapter detailed a method of calculating h_c through a sputtering front; in general, h_c is a complicated function of the surface temperature, the liquid temperature, and the liquid flow rate. These calculations would be difficult without a computer,* and have been done numerically for all flow rates and subcoolings of interest. The results are given in Fig. 46. The heat-transfer coefficients were also calculated for Region 1, and the results are shown in the same figure. The maximum surface temperature for Region 2 is $T_{\text{sur,CHF}}$ and is found iteratively with Eqs. 53 and 55. These calculations are tedious without a computer, so they have been carried out for a wide range of subcoolings and flow rates; the results are shown in Fig. 47. After $T_{\text{sur,CHF}}$ has been determined, the length ℓ of Region 2 can be found iteratively with Eq. 68. The temperature gradient in the dry zone, Region 3, is constant because this region is adiabatic and equal to the gradient at ℓ . The solution of Eq. 68 for the gradient is²²

*A useful rule of thumb was discovered in carrying out these calculations: a good guess for the average heat-transfer coefficient is

$$\bar{h}_c = \frac{0.6\phi_{\text{CHF}}}{T_{\text{sur,CHF}} - T_{\text{liq}}}.$$

$$\frac{d}{dz}T_{rod}|_l = (T_{incip} - T_{liq})[\text{root}_2 \sinh(\text{root}_2 l) + \text{root}_1 \cosh(\text{root}_2 l)]. \quad (69)$$

The results of this simplified analysis for all the data obtained here are shown in Fig. 48. Triangles, denoting one-dimensional results, are connected to the corresponding two-dimensional results, denoted as circles, for each data point. It can be seen that the one-dimensional simplified model is in good agreement with these data. The one-dimensional model is adequate for these data because two-dimensional effects do not dominate; the Biot number is approximately 0.6 for these data.

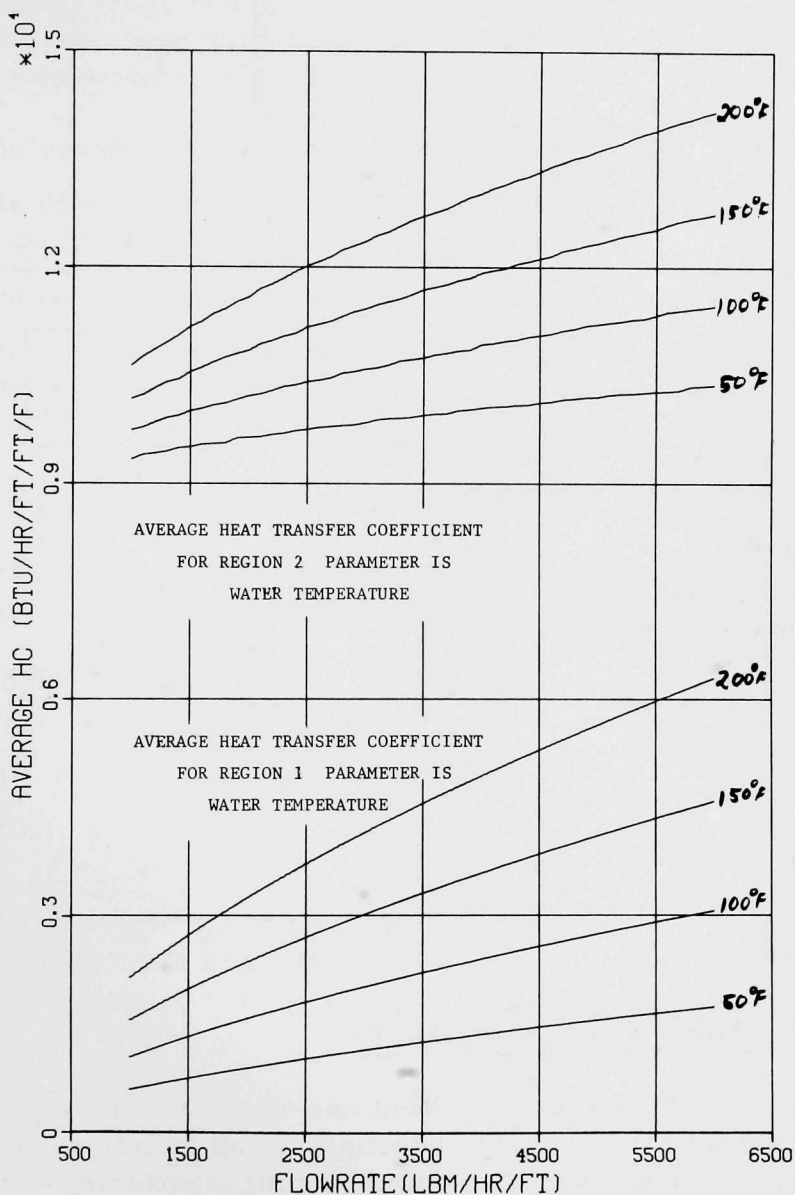


Fig. 46. Average Heat-transfer Coefficient as a Function of Flow Rate and Subcooling. ANL Neg. No. 900-75-901.

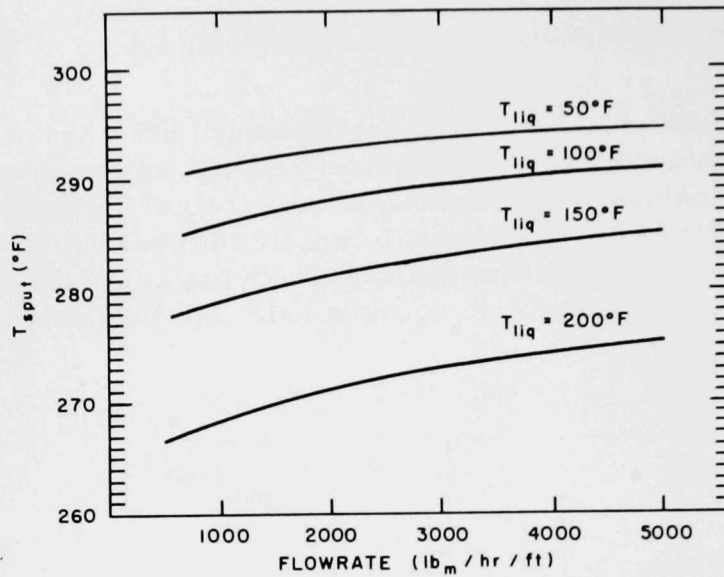


Fig. 47

Variation of Sputtering Temperature with Flow Rate and Subcooling. ANL Neg. No. 900-75-902.

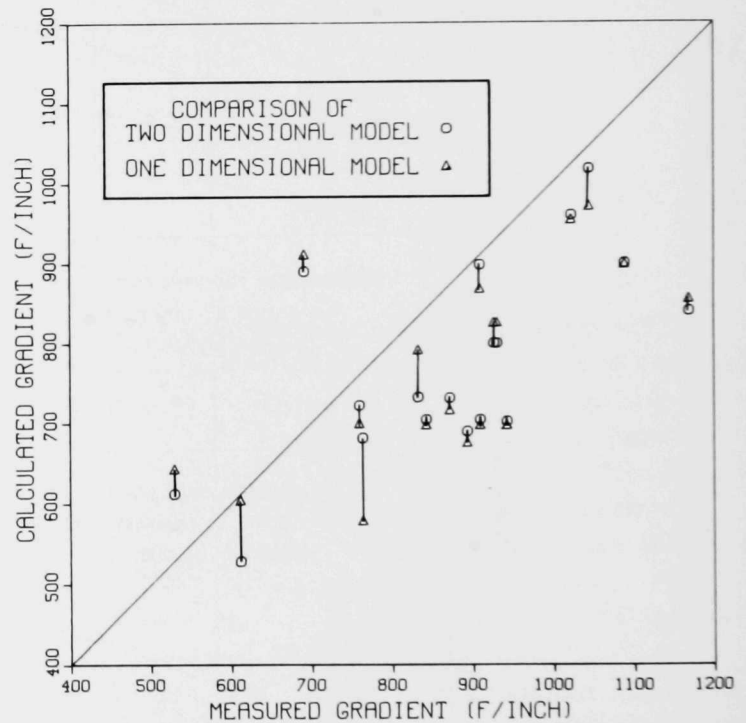


Fig. 48

Comparison of One-dimensional Analysis, Two-dimensional Analysis, and Data. ANL Neg. No. 900-75-903.

E. Analysis of a Moving Sputtering Front

Good agreement of the simplified one-dimensional model and data has shown that a constant heat-transfer coefficient and an adiabatic dry zone are good simplifying assumptions. To model moving-sputtering-front data, a coordinate transformation is necessary which will reduce the transient analysis to a steady-state analysis. Consider the origin to move with the sputtering front and the dry zone as in the positive z direction. Since most rewetting data^{19,61,81,82} have been obtained on surfaces for which thermal conductivity is

fairly low (typically Biot numbers range from 2 to 5[†]), two-dimensional effects must be considered. The governing two-dimensional equation for such a system is

$$\frac{\partial^2}{\partial z^2} T_t + \frac{\partial^2}{\partial y^2} T_t + \frac{u_{\text{sput}} \rho_t c_t}{k_t \epsilon_t} \frac{\partial}{\partial z} T_t = 0. \quad (70)$$

The governing differential equation is solved for two regions, a wetted region and a dry region, and the solutions are joined together under the constraints that (1) the average temperature at the junction of both regions are equal and (2) the average temperature gradient of both regions are equal at the junction. (A complete development of this model is shown in Appendix G.) Simplifying assumptions used in this model are:

1. The rewetting velocity is constant.
2. The effective water temperature is constant and estimated by simple energy balance.
3. The tube is adiabatic below the front.
4. The heat transfer above the front can be characterized with a constant heat-transfer coefficient.
5. The inside surface of the tube is adiabatic.
6. Since $\epsilon \ll D_t$, a rectangular coordinate system is adequate.

By introducing the dimensionless temperature and dimensionless sputtering velocity, the governing differential equation becomes

$$\frac{\partial^2}{\partial \zeta^2} \tau + \frac{\partial^2}{\partial \eta^2} \tau + u^* \frac{\partial}{\partial \zeta} \tau = 0, \quad (71)$$

where

$$\tau = \frac{T - T_{\text{liq,eff}}}{T_{\infty} - T_{\text{liq,eff}}}; \quad (72)$$

$$u^* = \frac{\rho_t c_t \epsilon u_{\text{sput}}}{k_t}; \quad (73)$$

$$\zeta = \frac{z}{\epsilon}; \quad (74)$$

$$\eta = \frac{y}{\epsilon}; \quad (75)$$

[†]The Biot number ($\bar{h}_c \epsilon / k_t$) is estimated with $9000 < \bar{h}_c < 14,000$ Btu/hr-ft²-°F, $\epsilon \approx 0.035$ in., and $8 < k_t < 14$ Btu/hr-ft-°F.

$$T_{\text{liq,eff}} = T_{\text{liq,initial}} + \frac{u^* k_t (T_{\text{sput}} - T_{\text{liq}})}{\Gamma c_{\text{liq}}}. \quad (76)$$

For a given value of u^* , Eq. 71 can be solved for a dimensionless sputtering temperature, τ_0^* :

$$\tau_0^* = \frac{T_{\text{sput}} - T_{\text{liq,eff}}}{T_{\infty} - T_{\text{liq,eff}}}. \quad (77)$$

The dimensionless sputtering temperature is

$$\tau_0^* = \frac{(24 + 12\text{Bi})u^*}{(24 + 20\text{Bi} + 5\text{Bi}^2)(u^* + m_1)}, \quad (78)$$

where

$$m_1 = \frac{-u^*}{2} + \sqrt{\left(\frac{u^*}{2}\right)^2 + \frac{24\text{Bi} + 12\text{Bi}^2}{24 + 20\text{Bi} + 5\text{Bi}^2}}. \quad (79)$$

In general, the rewetting velocity is desired and initial temperatures are known; however, this analysis requires u^* and yields τ_0^* . This problem has been solved by plotting the calculated τ_0^* as a function of u^* for various Biot numbers, as shown in Fig. 49. Since the effective liquid temperature is a function of the rewetting velocity, an iterative solution is required. The following procedure can be used with this analysis:

1. Calculate the Biot number $\bar{h}_c \epsilon / k_t$ by estimating \bar{h}_c from Fig. 46 for $T_{\text{liq,initial}}$ and Γ .
2. Calculate τ_0^* , where T_{sput} is estimated from Fig. 47; for a first approximation $T_{\text{liq,eff}} = T_{\text{liq,initial}}$.
3. Determine u^* from Fig. 49.
4. Calculate $T_{\text{liq,eff}}$ from Eq. 76.
5. Recalculate the Biot number.
6. Recalculate τ_0^* .
7. Find u^* from Fig. 49.
8. If the new u^* is significantly different, repeat steps 4-7 with $u^* = (u_{\text{step } 3}^* + u_{\text{step } 7}^*)/2$; otherwise stop.

This procedure has been used to predict the rewetting velocity as measured by four investigators^{19,61,81,82} for a wide range of test conditions. Only data for unconfined geometries were compared because in a confined geometry the falling-liquid-film temperature could increase due to condensation. By restricting the data in this manner, the water temperature can be

estimated with reasonable accuracy. For a confining geometry, steam would be produced below the front as the water droplets fall down the channel, and this would then condense on the liquid film. This comparison has been tabulated in Table III and displayed in Fig. 50, where reasonably good agreement occurs over two orders of magnitude.

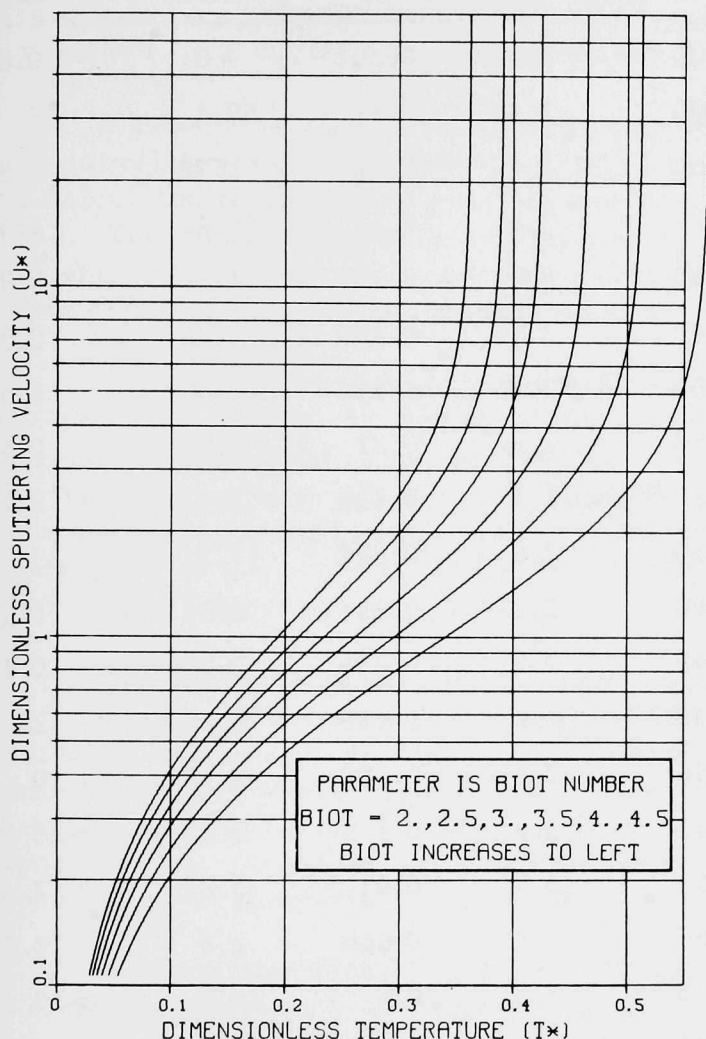


Fig. 49
Calculated Results of Two-dimensional
Moving-sputtering-front Analysis. ANL
Neg. No. 900-75-904.

Fig. 50
Measured and Calculated Rewetting
Velocity. ANL Neg. No. 900-75-905.

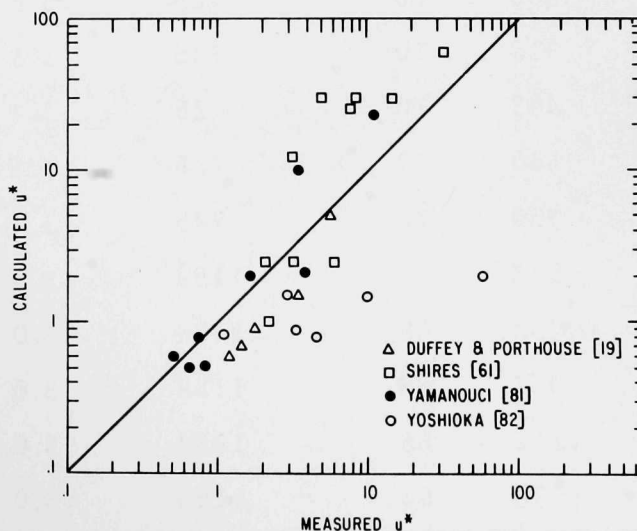


TABLE III. Calculated and Experimentally Measured
Dimensionless Rewetting Velocities

Ref.	T_{∞} , °F	T_{liq} , °F	Γ , lb _m /hr-ft	Biot No.	T_0^*	u_{meas}^*	u_{cal}^*
82	932	122	2500	3.47	0.201	4.6	0.8
82	752	70	5000	3.44	0.32	59.4	2
82	752	70	362	3.18	0.32	2.92	1.5
82	752	70	1327	3.21	0.32	10.4	1.5
82	752	158	1200	3.62	0.202	1.1	0.85
82	752	158	2600	3.67	0.208	3.46	0.9
81	1202	70	850	2.2	0.194	0.66	0.5
81	1112	70	850	2.2	0.21	0.835	0.52
81	572	70	850	2.2	0.438	3.91	2.1
81	392	70	850	2.6	0.528	11.7	23
81	1022	70	340	2.2	0.23	0.51	0.6
81	932	70	340	2.2	0.255	0.78	0.75
81	572	70	340	2.2	0.438	1.68	2
81	392	70	340	2.4	0.502	3.52	10
61	360	70	363	3.5	0.5	7.76	>25
61	490	70	363	3.5	0.41	3.25	12
61	660	70	363	3.4	0.366	2.2	2.5
61	350	70	725	3.5	0.6	14.9	>30
61	410	70	725	3.5	0.55	5.0	>30
61	650	70	725	3.5	0.37	3.2	2.5
61	330	70	725	3.3	0.75	33.5	>60
61	495	70	725	3.4	0.5	8.4	>30
61	660	70	725	3.4	0.87	6.0	2.5
61	950	70	725	3.4	0.246	2.2	1
19	572	68	1154	3.0	0.436	5.7	5
19	752	68	1154	3.0	0.32	3.5	1.5
19	932	68	1154	3.0	0.25	1.76	0.9
19	1112	68	1154	3.0	0.21	1.45	0.7
19	1292	68	1154	3.0			

VII. CONCLUSIONS

Experimental evidence that the sputtering-front temperature corresponds to a CHF phenomena has been obtained. The data were analyzed in an unbiased least-squares sense and showed the lowest wetted surface temperature to be approximately 270°F. This temperature closely corresponds to reported CHF surface temperatures for water.

A two-dimensional model was proposed to describe the data, and a good correlation between model and data has been obtained. Experimental and calculated temperature profiles were compared in detail for five test cases. The measured total heat-removal capacity of all the data obtained here show reasonably good agreement with this analysis. The analysis has shown evidence of two-dimensional effects near the sputtering front.

The two-dimensional model is based on a continuous curve for the heat-transfer coefficient, which is formulated from various heat-transfer correlations available in the literature. A method has been proposed and illustrated by an example for calculating the heat-transfer coefficient throughout a sputtering front based upon local conditions. The heat-transfer coefficients were of the order of 10,000 Btu/hr-ft²-°F, which is in variance with other values reported heretofore.

The increase in the water temperature as it passes through a sputtering front was measured, and it was found that the temperature rise can be estimated by a simple energy balance. Most of the thermal energy transferred from the rod in the cooling process can be accounted for in the gain of sensible heat by the water. Only a negligible fraction of this energy contributes to net vapor release. In general, the temperature rise was approximately 10-30°F depending upon flow rate for these data.

A simplified three-region model, in which each region is characterized by a constant heat-transfer coefficient, was proposed. A simplified one-dimensional model showed good agreement with the data because two-dimensional effects did not dominate. Typical Biot numbers near the sputtering front were of the order of 0.6.

A two-dimensional, two-region linear model for moving sputtering fronts has been proposed and compared to reported rewetted data. This model is based upon the propositions that the sputtering front is a CHF phenomenon and the dry zone is adiabatic. Reasonably good agreement was obtained.

APPENDIX A

Relation between a Stationary Sputtering Front and a Moving Sputtering Front

Up to the present, sputtering has been examined as it progresses down a vertical tube. The data have been presented with accompanying analyses which predict the rewetting velocity. The literature contains sputtering data for water at various pressures, temperatures, and flow rates. However, all the data obtained here and the model to describe these data are for a stationary sputtering front. In this appendix, a means of relating a moving sputtering front to a stationary sputtering front will be developed. The following analysis is similar to the one used by Yamanouchi with the exception that this is for a solid rod, whereas Yamanouchi modeled a tube.

Consider an initially isothermal vertical solid rod. Let the rod be cooled by a falling liquid film which advances downward at a constant rate, u_{sput} ; assume that at time = 0, the film has advanced to some point z . Assume that the film temperature remains constant, the rod has constant properties, and that the heat-transfer process in the wetted zone can be characterized by a constant heat-transfer coefficient \bar{h}_c . The region below the liquid film front is adiabatic. This nonsteady analysis can be simplified by a moving coordinate system with its origin at the liquid front. If the positive z direction is downward, the one-dimensional equation of this process is

$$\frac{d^2 T_{\text{rod}}}{dz^2} + \frac{u_{\text{sput}} \rho_{\text{rod}} c_{\text{rod}}}{k_{\text{rod}}} \frac{dT_{\text{rod}}}{dz} - \frac{4\bar{h}_c(T_{\text{rod}} - T_{\text{liq}})}{k_{\text{rod}} D_{\text{rod}}} = 0. \quad (\text{A.1})$$

The following boundary conditions are applicable:

$$\text{B.C. 1 at } z = -\infty: T_{\text{rod}} = T_{\text{liq}};$$

$$\text{B.C. 2 at } z = 0: T_{\text{rod}} = T_{\text{sput}};$$

$$\text{B.C. 3 at } z = 0: \frac{d}{dz} T_{\text{rod}} \text{ is smoothly continuous};$$

$$\text{B.C. 4 at } z = \infty: T_{\text{rod}} = T_{\infty}.$$

The complementary solution of Eq. A.1 is

$$T_{\text{rod}} = (T_{\text{sput}} - T_{\text{liq}})e^{(\text{root}_1 z)},$$

where

$$\text{root}_1 = \frac{-\frac{u_{\text{sput}} \rho_{\text{rod}} c_{\text{rod}}}{k_{\text{rod}}} + \sqrt{\frac{u_{\text{sput}}^2 \rho_{\text{rod}}^2 c_{\text{rod}}^2}{k_{\text{rod}}^2} + \frac{16 h_c}{k_{\text{rod}} D_{\text{rod}}}}}{2}$$

A particular solution is $T_{\text{rod}} = T_{\text{liq}}$, and the complete solution for $z \leq 0$ is

$$T_{\text{rod}} = T_{\text{liq}} + (T_{\text{sput}} - T_{\text{liq}})e^{(\text{root}_1 z)}. \quad (\text{A.2})$$

Below the front, $z > 0$, the heat-transfer coefficient is zero, and Eq. A.1 becomes

$$\frac{d^2 T_{\text{rod}}}{dz^2} + \frac{u_{\text{sput}} \rho_{\text{rod}} c_{\text{rod}}}{k_{\text{rod}}} \frac{dT_{\text{rod}}}{dz} = 0.$$

With boundary conditions 2 and 4, this has a solution

$$T = T_{\infty} - (T_{\infty} - T_{\text{sput}}) \exp\left(-\frac{u_{\text{sput}} \rho_{\text{rod}} c_{\text{rod}}}{k_{\text{rod}}} z\right). \quad (\text{A.3})$$

Equations A.2 and A.3 are joined at $z = 0$ to form a smoothly continuous temperature profile. Therefore the derivatives at this point must be equal:

$$(\text{root } 1)(T_{\text{sput}} - T_{\text{liq}}) = (T_{\infty} - T_{\text{sput}}) \frac{u_{\text{sput}} \rho_{\text{rod}} c_{\text{rod}}}{k_{\text{rod}}}. \quad (\text{A.4})$$

By solving Eq. A.4 for the rewetting velocity, we obtain

$$u_{\text{sput}} = \frac{(T_{\text{sput}} - T_{\text{liq}})}{(T_{\infty} - T_{\text{sput}})} \frac{\text{root}_1 k_{\text{rod}}}{\rho_{\text{rod}} c_{\text{rod}}}. \quad (\text{A.5})$$

Since the sputtering front is assumed to move at a constant velocity, the heat-removal capacity can be considered to be the sum of two components: (1) the energy conducted to the front by the temperature gradient immediately below the front, and (2) the energy removed by the cooling of the rod from T_{sput} to T_{liq} :

$$\begin{aligned} \dot{Q}_{\text{moving}} &= \dot{Q}_{\text{conducted to front}} + \dot{Q}_{\text{cooling of rod}} \\ &= k_{\text{rod}} \frac{\pi}{4} D_{\text{rod}}^2 \left. \frac{dT_{\text{rod}}}{dz} \right|_0 + \frac{\pi}{4} D_{\text{rod}}^2 \rho_{\text{rod}} c_{\text{rod}} (T_{\text{sput}} - T_{\text{liq}}) u_{\text{sput}} \\ &= k_{\text{rod}} \frac{\pi}{4} D_{\text{rod}}^2 (T_{\infty} - T_{\text{sput}}) \frac{u_{\text{sput}} \rho_{\text{rod}} c_{\text{rod}}}{k_{\text{rod}}} \\ &\quad + \frac{\pi}{4} D_{\text{rod}}^2 \rho_{\text{rod}} c_{\text{rod}} (T_{\text{sput}} - T_{\text{liq}}) u_{\text{sput}}. \end{aligned} \quad (\text{A.6})$$

The rate of energy removal determines how fast the sputtering front moves downward. Since the rewetting velocity is one to two orders of magnitude less than the average liquid velocity, the movement of a sputtering front should not affect the heat-transfer process.

If a stationary sputtering front were maintained on a solid rod, all the thermal energy would be conducted to it by a temperature gradient immediately below the front:

$$\dot{Q}_{\text{stationary}} = k_{\text{rod}} \frac{\pi}{4} D_{\text{rod}}^2 \left. \frac{dT_{\text{rod}}}{dz} \right|_0. \quad (\text{A.7})$$

Equating $\dot{Q}_{\text{stationary}}$ and \dot{Q}_{moving} as a given set of conditions (rod and fluid properties, flow rate, and temperatures), an equivalent rewetting velocity can be found from the temperature gradient in a stationary front:

$$u_{\text{sput}} = \frac{k_{\text{rod}}}{(T_{\infty} - T_{\text{liq}}) \rho_{\text{rod}} c_{\text{rod}}} \left. \frac{dT}{dz} \right|_0.$$

APPENDIX B

Stationary-sputtering-front Data

Run No.	1	2	3	4	5	6	7A	7B	8A	8B	9	10	11	12	13	14	15	16
Date	1/30/74	4/5/74	4/6/74	4/18/74	4/27/74	4/27/74	4/27/74	4/27/74	4/27/74	4/27/74	5/1/74	5/1/74	5/5/74	5/11/74	5/14/74	5/14/74	5/3/74	5/7/74
Γ , lbm/hr-ft Error, %	694 ± 2	678 ± 2	968 ± 2	357 ± 2	1,598 ± 2	1,216 ± 2	859 ± 2	859 ± 2	387 ± 5	387 ± 5	1,157 ± 2	896 ± 2	738 ± 5	539 ± 5	539 ± 5	397 ± 5	494 ± 3	465 ± 6
T_{liq} , °F Error, %	173 ± 2	160 ± 4	173 +0, -3	115 ± 4	159 ± 5	159 ± 5	148 ± 6	148 ± 6	107 ± 2	107 ± 2	150 ± 2	148 ± 2	71 ± 2	91 ± 5	98 ± 2	102 ± 2	73 ± 2	85 ± 6
ϕ_{cond} , Btu/hr-ft ² Error, %	Not measured	8,135 ± 20	8,883 +0, -10	4,032 ± 20	~0	~0	~0	~0	~0	~0	~0	1,100 ± 10	~0	~0	4,446 ± 10	4,374 ± 10	1,580 ± 20	1,500 ± 50
$\delta _{T_0}$, mills	12.7	12.8	14.3	12	16.8	15.5	14.2	14.2	11.6	11.6	15.4	14.4	15.8	13.8	12.9	11.9	12.7	12.5
T_{spray} , °F	192-203	-	191	187	172	175	168	-	-	-	-	-	-	-	-	-	-	-
$\Delta\sigma$, dynes/cm	0	40	0	0	40	40	40	40	40	40	35	35	35	44	42	42	35	0
\bar{u}_{liq} , ft/hr	10,800	10,400	13,300	6,120	18,700	15,500	11,900	11,900	6,480	6,480	14,800	12,240	9,000	7,560	8,100	6,480	7,560	7,200

Note: $\Delta\sigma$ is the decrease in surface tension of the water due to the addition of surfactant.
 $\delta|_{T_0}$ is the liquid film thickness as evaluated by Eq. 23 at the initial liquid temperature.

APPENDIX C

Estimate of Contact Temperature Error

A momentary depression of the rod surface temperature was caused by the thermocouple probe contacting the surface. The thermal response of the junction was analyzed as a two-dimensional finite-difference model. This transient analysis showed the junction temperature to recover to within 1°F in 100 ms (see Fig. C.1).

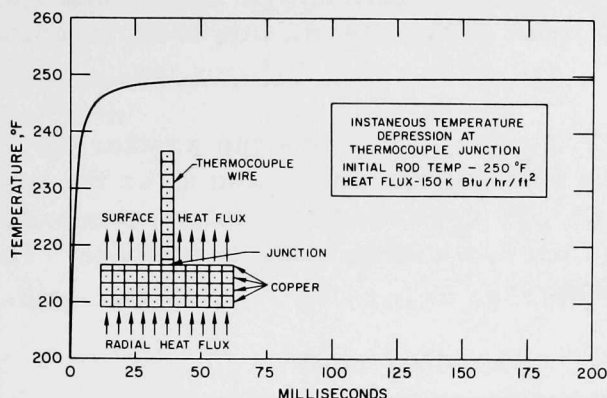


Fig. C.1

Thermocouple Response. ANL
Neg. No. 900-75-906.

An initial estimate of this error can be obtained by considering two semi-infinite isothermal bodies of different temperatures.³² If these two bodies are brought together, the interface temperature is invariant in time, and is determined by the thermal properties and initial temperatures:

$$\frac{T_2 - T_i}{T_i - T_1} = \sqrt{\frac{\rho_1 c_1 k_1}{\rho_2 c_2 k_2}} \quad (C.1)$$

For example, with the present materials and initial temperatures of

Thermocouple: $k = 34 \text{ Btu/hr-ft}^2\text{-}^\circ\text{F}$, $\rho = 555 \text{ lb}_m/\text{ft}^3$,

$c = 0.103 \text{ Btu/lb}_m\text{-}^\circ\text{F}$, $T_0 = 100^\circ\text{F}$,

Copper rod: $k = 218 \text{ Btu/hr-ft}^2\text{-}^\circ\text{F}$, $\rho = 558 \text{ lb}_m/\text{ft}^3$,

$c = 0.091 \text{ Btu/lb}_m\text{-}^\circ\text{F}$, $T_0 = 250^\circ\text{F}$.

The interface temperature is 207°F or an error of 43°F. An error of this magnitude justifies a more accurate model.

The analysis used here considers a cross section of the rod at a given axial location. Only the rod material near the surface is involved, so the problem is simplified by assuming a rectangular grid (see Fig. C.1). The analysis was conducted for conditions in the boiling zone, where a radial temperature gradient and surface heat flux existed. The transient analysis showed the interface temperature to increase rapidly because of the relative masses of the material and junction geometry. Since Eq. C.1 does not take this into consideration as an initial guess.

APPENDIX D

Estimate of the Condensation Heat Flux

The temperature of the falling liquid film sometimes increases as much as 20°F before it reaches the vicinity of the sputtering front. It was determined that condensation from steam inside the hood was the cause of this temperature rise. Neither the ambient temperature nor the lighting intensity was sufficient to cause an increase of this magnitude. The condensation heat flux varied from run to run because of different operating conditions. A heat exchanger (see Fig. 10) was capable of removing most of the steam; however, in some tests its capacity was insufficient.

Four thermocouples, 17, 7, 4, and 2 in. above the sputtering front, showed the temperature rise to be linear both before and after the sputtering temperature profile was measured. By assuming a constant condensation heat flux, a simple energy balance was used to estimate its magnitude. The following example illustrates this method.

Run 14, $\Gamma = 397 \text{ lb}_m/\text{hr-ft}$

T _{film} , (°F)		Position (in. above sputtering front)
Before Test	After Test	
89	88	17 (inlet)
96	94	7
98	99	4
103	102	1.75

In steady state, the sum of energy entering and leaving is

$$\sum \dot{E}_{\text{in}} - \sum \dot{E}_{\text{out}} = 0,$$

that is,

$$\Gamma c_{\text{liq}} T_{\text{in}} + \varphi_{\text{con}} \Delta z - \Gamma c_{\text{liq}} T_{\text{out}} = 0.$$

Accordingly,

$$\varphi_{\text{con}} = \frac{\Gamma c_{\text{liq}} (T|_{\text{out}} - T|_{\text{in}})}{\Delta z} = 4374 \text{ Btu/hr-ft}^2.$$

APPENDIX E

Numerical Methods

The one-dimensional energy equation of the rod and liquid are nonlinear because of the temperature dependence of the heat-transfer coefficient. These two equations are solved simultaneously by the modified Euler method,²⁸ and the solutions of these equations, the temperature profiles through a sputtering front, are used in a two-dimensional model which employs the relaxation technique.³⁹ Both of these numerical methods are described here.

The modified Euler method truncates the Taylor series after the second-derivative term:

$$T|_{z+\Delta z} = T|_z + \frac{d}{dz} T|_z \Delta z + \frac{d^2}{dz^2} T|_z \frac{\Delta z^2}{2}. \quad (\text{E.1})$$

The one-dimensional energy equation of the rod for a stationary sputtering front is

$$\frac{d^2}{dz^2} T_{\text{rod}} = \frac{4h_c}{k_{\text{rod}} D_{\text{rod}}} (T_{\text{rod}} - T_{\text{liq}}), \quad (\text{E.2})$$

where $h_c = F(T_{\text{rod}}, T_{\text{liq}}, \Gamma)$, as discussed in Ch. V.

Let the step size be Δz (0.0005 in. was used for the one-dimensional model). By inserting Eq. E.2 into Eq. E.1, one obtains

$$\begin{aligned} T_{\text{rod}}|_{z+\Delta z} = T_{\text{rod}}|_z + \frac{d}{dz} T_{\text{rod}}|_z \Delta z \\ + \frac{4h_c(T_{\text{rod}}|_z, T_{\text{liq}}|_z, \Gamma)}{k_{\text{rod}} D_{\text{rod}}} \frac{\Delta z^2}{2} (T_{\text{rod}}|_z - T_{\text{liq}}|_z). \end{aligned} \quad (\text{E.3})$$

Starting at some location above the sputtering front, where the initial conditions are known, Eq. E.3 is used to progressively calculate the rod temperature in the downward direction. Since T_{liq} is required at each step, the liquid-energy equation, Eq. 16, is solved simultaneously and is approximated as

$$T_{\text{liq}}|_{z+\Delta z} = T_{\text{liq}}|_z + \frac{d}{dz} T_{\text{liq}}|_z \Delta z + \frac{d^2}{dz^2} T_{\text{liq}}|_z \frac{\Delta z^2}{2}. \quad (\text{E.4})$$

To solve Eq. E.4, the first derivative is calculated as

$$\frac{d}{dz} T_{\text{liq}}|_z = \frac{h_c|_z (T_{\text{rod}}|_z - T_{\text{liq}}|_z)}{\Gamma c_{\text{liq}}} + \frac{\varphi_{\text{con}}}{\Gamma c_{\text{liq}}}, \quad (\text{E.5})$$

and the second derivative is estimated as

$$\begin{aligned} \frac{d^2}{dz^2} T_{\text{liq}} &= \frac{\frac{d}{dz} T_{\text{liq}}|_{z+\Delta z} - \frac{d}{dz} T_{\text{liq}}|_z}{\Delta z} \\ &= \frac{h_c|_z (T_{\text{rod}}|_{z+\Delta z} - T_{\text{liq}}|_{z+\Delta z}) - h_c|_z (T_{\text{rod}}|_z - T_{\text{liq}}|_z)}{\Delta z \Gamma}. \end{aligned} \quad (\text{E.6})$$

For the approximating calculation of Eq. E.6, the liquid temperature is estimated as

$$T_{\text{liq}}|_{z+\Delta z} = T_{\text{liq}}|_z + \frac{d}{dz} T_{\text{liq}}|_z \Delta z. \quad (\text{E.7})$$

The following summarizes the numerical method used to obtain the one-dimensional temperature profiles:

1. h_c is found as shown in Ch. V for a given set of T_{rod} , T_{liq} , and Γ .
2. $T_{\text{rod}}|_{z+\Delta z}$ is found by means of Eq. E.3.
3. $T_{\text{liq}}|_{z+\Delta z}$ is initially estimated by use of Eq. E.7.
4. $d^2/dz^2 T_{\text{liq}}|_z$ is found by means of Eq. E.6.
5. $d/dz T_{\text{liq}}|_z$ is found by means of Eq. E.5.
6. $T_{\text{liq}}|_{z+\Delta z}$ is found by use of Eq. E.4.

The initial conditions required for those calculations were measured from the data: initial rod temperature, rod temperature gradient, and liquid temperature. For the next iteration, the rod temperature gradient is updated:

$$\frac{d}{dz} T_{\text{rod}}|_{z+\Delta z} = \frac{d}{dz} T_{\text{rod}}|_z + \frac{d^2}{dz^2} T_{\text{rod}}|_z \Delta z. \quad (\text{E.8})$$

After sufficient steps to pass through the sputtering front (~4500), the rod and liquid temperature profiles were operated upon by a two-dimensional relaxation program. The two-dimensional array used for calculating the rod-temperature field was 450 by 8. Each element represented a one radian sector of an axisymmetric shell 0.005 in. long and a thickness such that the cross-sectional area was $(1/16)\pi$ of the total rod cross-sectional area. It was found that this choice of node structure and the simultaneous solution of the eight radial nodes and water node enhanced convergence. Even with this approach, slow convergence was a problem, so a very good initial guess was needed. The one-dimensional model results were used as a starting condition for a two-node two-dimensional model which calculates the centerline and surface temperature. This two-node model used a 2 by 450-element array for the rod and a 450-element array for the water. The array was relaxed 1000 times, and

these calculations were then used for the 8-node model. The starting condition of the two-dimensional eight-node array had centerline and surface temperatures as calculated by the two-node model, and intermediate radial nodes were obtained by linear interpolation.

In addition to a steady state, the two-dimensional model assumes:

1. The rod has constant properties.
2. The rod has centerline symmetry; the heat transfer at a given axial location is constant around the entire periphery.

In steady state, the net thermal energy entering any differential element is zero; therefore, the two-dimensional finite-element energy equation of the rod nodes 2 to 7 (see Figs. 13 and E.1) is

$$\begin{aligned}
 & -k_{\text{rod}}A_i \frac{T_i - T_a}{\Delta r_i} - k_{\text{rod}}A_z \frac{T_i - T_b}{\Delta z} - k_{\text{rod}}A_{i+1} \frac{T_i - T_c}{\Delta r_{i+1}} \\
 & - k_{\text{rod}}A_z \frac{T_i - T_d}{\Delta z} = 0,
 \end{aligned} \tag{E.9}$$

where i is the node number, and

$$A_i = \sqrt{i-1} D_{\text{rod}} \Delta z / 4;$$

$$\Delta r_i = \frac{(\sqrt{2i-1} - \sqrt{2i-3}) D_{\text{rod}}}{8};$$

$$A_z = \frac{1}{64} D_{\text{rod}}^2 \left(\frac{1}{16\pi} \text{ cross-sectional area} \right);$$

$$\Delta z = \text{axial interval (0.005 in. for two-dimensional calculations);}$$

$$A_{i+1} = \sqrt{i} D_{\text{rod}} \Delta z / 4;$$

$$\Delta r_{i+1} = \frac{(\sqrt{2i+1} - \sqrt{2i-1}) D_{\text{rod}}}{8},$$

and T_a , T_b , T_c , and T_d are the adjacent node temperatures to the left, bottom, right, and top of the central node, respectively. The node temperature is found by solving Eq. E.9 for T_i :

$$T_i = \frac{\frac{A_i}{\Delta r_i} T_a + \frac{A_z}{\Delta z} T_b + \frac{A_{i+1}}{\Delta r_{i+1}} T_c + \frac{A_z}{\Delta z} T_d}{\frac{A_i}{\Delta r_i} + \frac{A_z}{\Delta z} + \frac{A_{i+1}}{\Delta r_{i+1}} + \frac{A_z}{\Delta z}}. \tag{E.10}$$

The centerline node temperature, $i = 1$, is found from Eq. E.10 with $A_i/\Delta r_i = 0$ and $A_{i+1}/\Delta r_{i+1} = 4\Delta z/(\sqrt{8}(\sqrt{3} - 1))$. Likewise, the surface node temperature, $i = 8$, is found from Eq. E.10 with $A_{i+1}/\Delta r_{i+1} = D_{rod}\Delta z/2h_c/k_{rod}$ and $T_c = T_{liq}$. Equation E.10 was solved for each node in the 8×450 array for 1000 iterations.

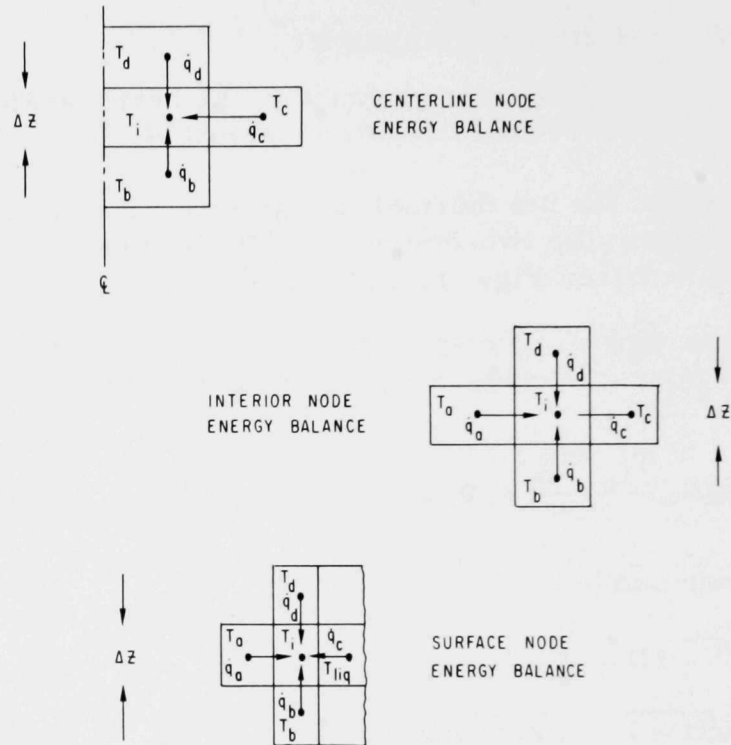


Fig. E.1. Two-dimensional Temperature Grid.
ANL Neg. No. 900-75-907.

APPENDIX F

Statistical Definitions and Methods

Because of the random nature of experimental error, statistical methods were used to infer information from the data in a quantitative manner. The surface temperature profiles were subject to errors in both position and temperature. The statistical analysis of data is greatly simplified if one of the parameters, the probe position, were considered accurate while the other was subject to error. For example, if the probe were mispositioned by 0.040 in. where a temperature gradient of 1000°F/in. existed, the error would be considered 40°F and not 0.040 in. These methods are best explained graphically, and this approach will be taken here with run 8A and run 8B done as examples.

1. Linear Least-squares Regression Line

A straight line,

$$T_{\text{est}} = T_0 + \bar{T}_1 z, \quad (\text{F.1})$$

was fitted through the data in a least-squares sense (see Fig. F.1). Both T_0 and \bar{T}_1 are chosen to minimize the summation of the deviations squared from the fitted line to the data in the vertical direction. T_0 and \bar{T}_1 are found by setting the derivative equal to zero and inserting $(z, T(z))$ from each of the N data points and solving for T_0 and \bar{T}_1 as follows:

$$\begin{aligned} \frac{\partial}{\partial T_0} \sum (\text{deviations}) &= 0 = \frac{\partial}{\partial T_0} \sum [T_0 + \bar{T}_1(z) - T_{\text{mea}}(z)]^2 \\ &= 2 \sum [T_0 + \bar{T}_1(z) - T_{\text{mea}}(z)] \end{aligned} \quad (\text{F.2})$$

and

$$\begin{aligned} \frac{\partial}{\partial \bar{T}_1} \sum (\text{deviations}) &= 0 = \frac{\partial}{\partial \bar{T}_1} \sum [T_0 + \bar{T}_1(z) - T_{\text{mea}}(z)]^2 \\ &= 2 \sum \{[T_0 + \bar{T}_1(z) - T_{\text{mea}}(z)](z)\}. \end{aligned} \quad (\text{F.3})$$

When T_0 and \bar{T}_1 are obtained in this manner, Eq. F.1 is a linear line of regression of T on z .

2. Standard Error of Estimate

The standard error of estimate of T on z is defined as

$$s_{t,z} = \sqrt{\frac{\sum (T_{\text{mea}} - T_{\text{est}})^2}{N}} \sqrt{\frac{N}{N-2}}, \quad (\text{F.4})$$

where T_{est} is obtained from Eq. F.1 for each of the N data points. The second factor on the right-hand side of Eq. F.4 increases the standard error of estimate as N decreases. The quantity $s_{t,z}$ should more precisely be called the standard error of estimate of small samples. Two parallel lines, one line $s_{t,z}$ above the regression line and the other $s_{t,z}$ below the regression line, bound 68% of the data. For a 95% confidence band, these lines are $2s_{t,z}$ above and below the regression line (see Fig. F.1).

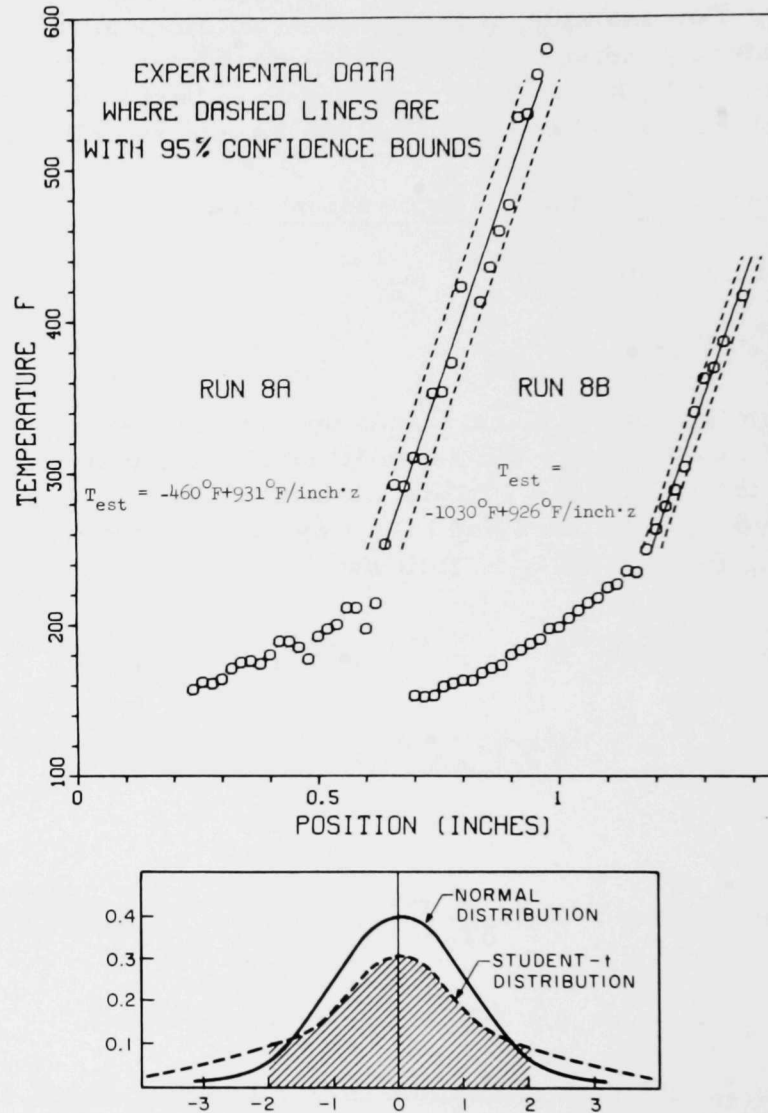


Fig. F.1. Statistical Methods. ANL Neg. No. 900-75-908 Rev. 1.

3. Coefficient of Correlation

The square root of the explained variation squared divided by the total squared is known as coefficient of correlation:

$$r = \pm \sqrt{\frac{(\text{explained variation})^2}{(\text{total variation})^2}} = \pm \sqrt{\frac{\sum (T_{est} - \bar{T})^2}{\sum T^2 - \frac{(\sum T)^2}{N}}} \quad (F.5)$$

Explained variation is defined as the sum of the squares of the variations of the calculated and measured average temperature for each of the data points within 68% confidence bounds. The coefficient of correlation is positive if the measured temperature and the estimated temperature both have the same trends; it is negative if one increases while the other decreases. For a linear regression line, given by Eq. F.1, the coefficient of correlation can be obtained by the product momentum method as

$$r = \frac{\sum (z_{\text{act}} - \bar{z})(T_{\text{act}} - \bar{T})}{\sqrt{\sum (z_{\text{act}} - \bar{z})^2 \sum (T_{\text{act}} - \bar{T})^2}} \quad (\text{F.6})$$

The quantity r varies from -1 to +1 and is a quantitative measure of how well the line of regression correlates the data. Values of r close to one indicate that the line of regression closely matches the data. For the example considered, a linear temperature gradient is indicated and, hence, no significant surface heat flux in that region.

A range for \bar{T}_1 where a 95% confidence can be obtained is determined as

$$\bar{T}_1 \pm \frac{t|_{0.95}}{\sqrt{N-2}} \frac{s_{t,z}}{s_z} = \bar{T} \pm \frac{t|_{0.95}}{\sqrt{N-2}} \frac{s_{t,z}}{\sqrt{\sum \frac{z^2}{N}}} \quad (\text{F.7})$$

where $t|_{0.95}$ is the two-tailed student-t distribution for $N-2$ degrees of freedom at 95% significance. For a graphical explanation refer to Fig. F.1. The total area under a student-t distribution curve is unity; the shaded area of Fig. F.1 is 0.95 or 95%, and the area under each tail is 2.5%. The number of degrees of freedom is the sample size minus the number of parameters needed to describe the line of regression, namely, $N-2$. As N increases the student-t distribution approaches the normal distribution curve. Consider the N data points to be a small sample from a large population of possible data points. By examining the N data points and calculating $s_{t,x}$ and s_z , we can infer characteristics of the large population. The value of t can be obtained from a student-t distribution table for a given value of confidence and degree of freedom. Equation F.7 is then used to calculate the range of T_1 for a given confidence level. For example, runs 8A and 8B, with 95% of the samples of N data points taken at random, will have a temperature gradient between 926-936°F/in. and 921-931°F/in., respectively.

95% confidence band for T of run 8A

$$= \bar{T}_1 \pm \frac{t|_{0.95}}{\sqrt{N-2}} \frac{s_{t,z}}{s_z} = 931 \pm \frac{2.14}{\sqrt{16-2}} \frac{16.79}{59.33} = 931 \pm 5.2^\circ\text{F/in.}$$

95% confidence band for T_1 of run 8B

$$= 926 \pm \frac{2.57}{\sqrt{7-2}} \frac{8.83}{25.9} = 926 \pm 5.3^\circ\text{F/in.}$$

These statistical calculations were done for all the data of Appendix B and are tabulated in Table I.

APPENDIX G

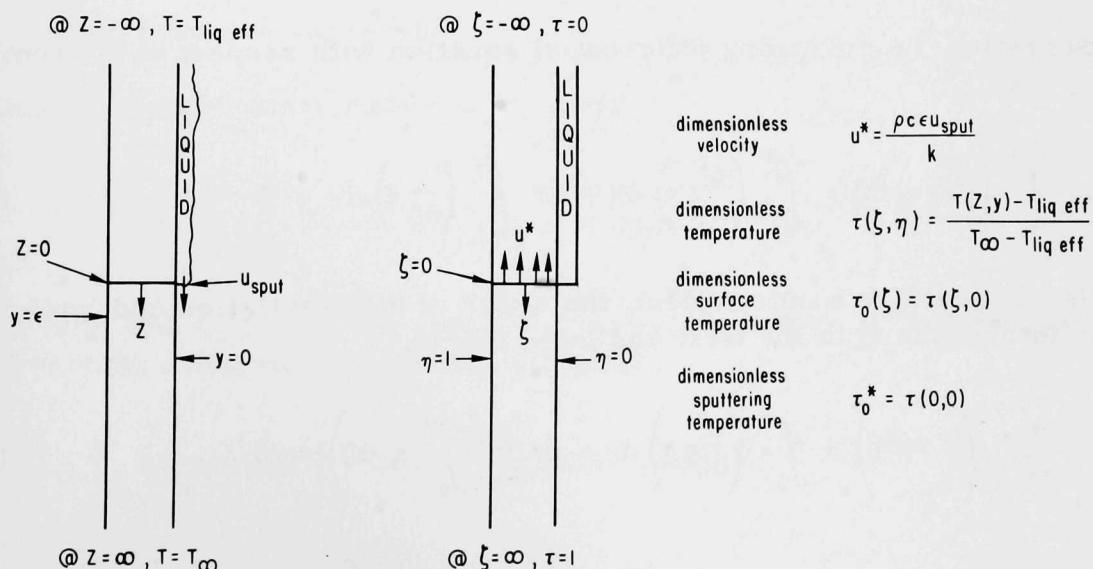
Two-dimensional Analysis of a Moving Sputtering Front

Much of the reported rewetting data have been obtained on surfaces where thermal conductivity is fairly low. Typically stainless steel ($k = 10 \text{ Btu/hr-ft-}^\circ\text{F}$ [$17.3 \text{ W/m-}^\circ\text{C}$]) or similar materials have been used because of their chemical stability at elevated temperatures. It was shown in Ch. V that heat-transfer coefficients of the order of $10,000 \text{ Btu/hr-ft}^2$ ($5.6 \text{ W/cm}^2\text{-}^\circ\text{C}$) can be associated with the boiling of water and hence with sputtering. The sputtering Biot number ($h_c \epsilon / k$) for tubes of wall thicknesses of about 0.040 in. (1 mm) range from 2 to 5, which indicates two-dimensional effects dominate the heat-transfer process. To model such a process, the following assumptions are made:

1. The rewetting velocity is constant.
2. The dry zone is adiabatic.
3. The effective liquid temperature is constant.
4. Heat transfer in the wetted zone can be characterized with a constant heat-transfer coefficient.
5. The tube-wall thickness is small compared to the tube diameter; hence, a rectangular coordinate system can be used.

By letting the origin move with the sputtering front, this transient heat-transfer problem is transformed into a steady-state problem. With the coordinate system and dimensionless variables as shown in Fig. G.1, the dimensionless governing differential equation becomes

$$\frac{\partial^2}{\partial \zeta^2} \tau + \frac{\partial^2}{\partial \eta^2} \tau + u^* \frac{\partial}{\partial \zeta} \tau = 0. \quad (\text{G.1})$$



The solution is found by considering two regions: $\zeta > 0$ and $\zeta < 0$, and joining the solutions at $\zeta = 0$. Let the variables Q^+ and Q^- , which are functions of ζ only, be defined as

$$Q^+ = \int_0^1 \tau \, d\eta, \quad \zeta \geq 0 \quad (\text{G.2})$$

and

$$Q^- = \int_0^1 \tau \, d\eta, \quad \zeta \leq 0. \quad (\text{G.3})$$

At $\zeta = 0$, the regions are joined under the constraints that

$$Q^-|_0 = Q^+|_0 \quad (\text{G.4})$$

and

$$\frac{\partial}{\partial \zeta} Q^-|_0 = \frac{\partial}{\partial \zeta} Q^+|_0. \quad (\text{G.5})$$

The dimensionless boundary conditions for the dry region, $\zeta > 0$, are

$$\text{B.C. 1 at } \eta = 0: \frac{\partial}{\partial \eta} \tau = 0;$$

$$\text{B.C. 2 at } \eta = 1: \frac{\partial}{\partial \eta} \tau = 0;$$

$$\text{B.C. 3 as } \zeta \rightarrow \infty: \tau \rightarrow 1.$$

By integrating the governing differential equation with respect to η from 0 to 1 for $\zeta > 0$,

$$\int_0^1 \left(\frac{\partial^2}{\partial \zeta^2} \tau \right) d\eta + \int_0^1 \left(\frac{\partial^2}{\partial \eta^2} \tau \right) d\eta + u^* \int_0^1 \left(\frac{\partial}{\partial \zeta} \tau \right) d\eta = 0. \quad (\text{G.6})$$

Because ζ and η are independent, the order of differentiation and integration can be interchanged in the first and third terms:

$$\frac{\partial^2}{\partial \zeta^2} \left(\int_0^1 \tau \, d\eta \right) + \int_0^1 \left(\frac{\partial^2}{\partial \eta^2} \tau \right) d\eta + u^* \frac{\partial}{\partial \zeta} \left(\int_0^1 \tau \, d\eta \right) = 0. \quad (\text{G.7})$$

Evaluating the second term and applying B.C. 1 and B.C. 2 give

$$\int_0^1 \left(\frac{\partial^2}{\partial \eta^2} \tau \right) d\eta = \frac{\partial}{\partial \eta} \tau \Big|_1 - \frac{\partial}{\partial \eta} \tau \Big|_0 = 0. \quad (\text{G.8})$$

Therefore,

$$\frac{\partial^2}{\partial \zeta^2} Q^+ + u^* \frac{\partial}{\partial \zeta} Q^+ = 0, \quad (\text{G.9})$$

and the solution of Q^+ is

$$Q^+ = C_1 - C_2 e^{-u^* \zeta}. \quad (\text{G.10})$$

From B.C. 3, $C = 1$; therefore,

$$Q^+ = 1 - C_2 e^{-u^* \zeta}. \quad (\text{G.11})$$

A similar approach is taken for the wetted zone, where the dimensionless boundary conditions are

$$\text{B.C. 4 at } \eta = 0: \frac{\partial}{\partial \eta} \tau = \text{Biot } \tau(\zeta, 0)$$

or

$$\frac{\partial}{\partial \eta} \tau = \text{Biot } \tau_0;$$

$$\text{B.C. 5 at } \eta = 1: \frac{\partial}{\partial \eta} \tau = 0;$$

$$\text{B.C. 6 as } \zeta \rightarrow -\infty: \tau \rightarrow 0.$$

Assume the temperature field has the form

$$\tau = \tau_0(\zeta) + \sum_{n=1}^{\infty} a_n(\zeta) \eta^n, \quad (\text{G.12})$$

where $\tau_0(\zeta)$ and $a_n(\zeta)$ are functions of ζ only. By inserting this form of τ into the governing differential equation, we obtain

$$\frac{\partial^2}{\partial \zeta^2} \tau_0(\zeta) + \sum_{n=1}^{\infty} \left[\frac{\partial^2}{\partial \zeta^2} a_n(\zeta) \eta^n \right] + 2a_2(\zeta) + \sum_{n=3}^{\infty} [n(n-1)a_n(\zeta) \eta^{n-2}] + u^* \frac{\partial}{\partial \zeta} \tau_0(\zeta) \quad (\text{G.13})$$

$$+ u^* \sum_{n=1}^{\infty} \left[\frac{\partial}{\partial \zeta} a_n(\zeta) \eta^n \right] = 0.$$

Since ζ and η are independent variables, an infinite number of equations result;

$$\frac{\partial^2}{\partial \zeta^2} a_n(\zeta) + u^* \frac{\partial}{\partial \zeta} a_n(\zeta) + (n+2)(n+1)a_{n+2}(\zeta) = 0; \quad n = 1, \infty. \quad (\text{G.14})$$

From B.C. 4, and noting that

$$\frac{\partial}{\partial \eta} \tau = a_1(\zeta) + \sum_{n=1}^{\infty} (n+1)a_{n+1}(\zeta)\eta^n, \quad (\text{G.15})$$

we have

$$\text{Biot } \tau_0(\zeta) = a_1(\zeta). \quad (\text{G.16})$$

Consider the first four terms of the temperature field:

$$\tau = \tau_0(\zeta) + a_1(\zeta)\eta + a_2(\zeta)\eta^2 + a_3(\zeta)\eta^3 \quad (\text{G.17})$$

$$= \tau_0(\zeta) + \text{Biot } \tau_0(\zeta)\eta + a_2(\zeta)\eta^2 + a_3(\zeta)\eta. \quad (\text{G.18})$$

From Eq. G.14 with $n = 1$ and $a_1(\zeta) = \text{Biot } \tau_0(\zeta)$,

$$\frac{\partial^2}{\partial \zeta^2} \tau_0(\zeta) + u^* \frac{\partial}{\partial \zeta} \tau_0(\zeta) + \frac{6a_3(\zeta)}{\text{Biot}} = 0. \quad (\text{G.19})$$

Therefore, from Eq. G.13,

$$2a_2(\zeta) = \frac{6a_3(\zeta)}{\text{Biot}}. \quad (\text{G.20})$$

After using B.C. 5 and solving for $a_2(\zeta)$ and $a_3(\zeta)$, Q^- can be found as

$$Q^- = \tau_0(\zeta) + \frac{\text{Biot } \tau_0(\zeta)}{2} - \frac{\text{Biot } \tau_0(\zeta)}{6 + 3 \text{ Biot}} - \frac{\text{Biot}^2 \tau_0(\zeta)}{24 + 12 \text{ Biot}}, \quad (\text{G.21})$$

with

$$\tau_0(\zeta) = \frac{(24 + 12 \text{ Biot})Q^-}{24 + 20 \text{ Biot} + 5 \text{ Biot}^2}. \quad (\text{G.22})$$

Integrating the governing differential Eq. G.1 with respect to η from 0 to 1 in the wetted region gives

$$\frac{\partial^2}{\partial \zeta^2} Q^- + u^* \frac{\partial}{\partial \zeta} Q^- - \text{Biot } \tau_0(\zeta) = 0. \quad (\text{G.23})$$

The last term on the left-hand side is derived as

$$\frac{\partial^2}{\partial \eta^2} \left(\int_0^1 \tau \, d\eta \right) = \frac{\partial}{\partial \eta} \tau(\zeta, 1) - \frac{\partial}{\partial \eta} \tau(\zeta, 0) = -\text{Biot} \, \tau_0(\zeta).$$

From Eqs. G.22 and G.23, we obtain

$$\frac{\partial^2}{\partial \zeta^2} Q^- + u^* \frac{\partial}{\partial \zeta} Q^- - \frac{24 \text{ Biot} + 12 \text{ Biot}^2}{24 + 20 \text{ Biot} + 5 \text{ Biot}^2} Q^- = 0. \quad (\text{G.24})$$

The quantity Q^- is a second-order differential equation whose solution is

$$Q^- = C_1 e^{m_1 \zeta} + C_2 e^{m_2 \zeta}, \quad (\text{G.25})$$

where m_1 and m_2 are the positive and negative roots, respectively, of

$$m_{1,2} = \frac{-u^*}{2} \pm \sqrt{\left(\frac{u^*}{2}\right)^2 + \frac{24 \text{ Biot} + 12 \text{ Biot}^2}{24 + 20 \text{ Biot} + 5 \text{ Biot}^2}}. \quad (\text{G.26})$$

Since Q^- is zero at $\zeta = -\infty$, we have $C_2 = 0$ and

$$Q^- = C_1 e^{m_1 \zeta}. \quad (\text{G.27})$$

We must match Q^+ and Q^- at $\zeta = 0$:

$$Q^+|_0 = Q^-|_0. \quad (\text{G.28})$$

Accordingly,

$$1 - C_2 e^{-u^*(0)} = C_1 e^{m_1(0)}, \quad (\text{G.29})$$

$$1 - C_2 = C_1, \quad (\text{G.30})$$

$$\frac{\partial}{\partial \zeta} Q^+|_0 = \frac{\partial}{\partial \zeta} Q^-|_0, \quad (\text{G.31})$$

$$u^* C_2 = m_1 C_1, \quad (\text{G.32})$$

and

$$Q^- = \frac{u^*}{u^* + m_1} e^{m_1 \zeta}. \quad (\text{G.33})$$

Therefore

$$\tau_0(\zeta) = \frac{24 + 12 \text{ Biot}}{24 + 20 \text{ Biot} + 5 \text{ Biot}^2} \frac{u^* e^{m_1 \zeta}}{u^* + m_1}, \quad (\text{G.34})$$

and the dimensionless sputtering temperature is

$$\tau_0^* = \frac{(24 + 12 \text{ Biot})u^*}{(24 + 20 \text{ Biot} + 5 \text{ Biot}^2)(u^* + m_1)}. \quad (\text{G.35})$$

The two-dimensional heat-transfer equation has been solved, however, in order to apply the final results, Eq. G.35, to moving-sputtering-front data. There are two complications. The first problem is that the governing differential equation yields τ_0^* as a function of u^* and Biot number. Normally, the opposite is desired, namely, τ_0^* and Biot number are known and u^* is desired. This obstacle can be overcome by solving Eq. G.35 for a wide variety of ($u^* - \text{Biot}$) combinations and interpolating. The second problem is in the definition of τ_0^* , which from Fig. G.1 is

$$\tau_0 = \frac{T_{\text{sput}} - T_{\text{liq eff}}}{T_{\infty} - T_{\text{liq eff}}}. \quad (\text{G.36})$$

As the falling liquid film cools the tube, heat transfer between the tube and liquid film will increase the liquid temperature. The effective liquid temperature is estimated by a one-dimensional energy balance as

$$T_{\text{liq eff}} = T_{\text{liq initial}} + \frac{u^* k_t (T_{\text{sput}} - T_{\text{liq initial}})}{\Gamma_{\text{cliq}}}. \quad (\text{G.37})$$

This complication requires an iterative solution in which $T_{\text{liq eff}}$ is initially estimated: $T_{\text{liq initial}}$, and a value of u^* is found. This u^* is then used in Eq. G.37 to obtain a better estimate of $T_{\text{liq eff}}$. This iterative process is then repeated as many times as required for the latest value of u^* equal the previous u^* .

ACKNOWLEDGMENTS

I would like to express my appreciation to my co-advisors Dr. M. A. Grolmes and Dr. J. H. Linehan for giving freely of their time and advice during this project.

This research was performed under the auspices of the U. S. Energy Research and Development Administration, Reactor Analysis and Safety Division, Argonne National Laboratory, through support of the Argonne Universities Association.

REFERENCES

1. K. J. Baumeister, R. C. Hendricks, and T. D. Hamill, *Metastable Leidenfrost States*, NASA TN D-3226 (Apr 1966).
2. K. J. Baumeister and F. F. Simon, *Leidenfrost Temperature--Its Correlation for Liquid Metals, Cryogens, Hydrocarbons, and Water*, J. Heat Transfer 95, 166 (May 1973).
3. Theodore Baumeister, Ed., *Marks' Standard Handbook for Mechanical Engineers*, McGraw-Hill Book Company, New York, N. Y., pp. 4-101 (1967).
4. G. S. Bays, W. H. McAdams, and T. B. Drew, Trans. ASME 62, 627 (1940).
5. A. W. Bennett, G. F. Hewitt, H. A. Kearsley, and R. K. F. Keeys, *The Wetting of Hot Surfaces by Water in a Steam Environment at High Pressures*, AERE-R-5146 (1966).
6. P. J. Berenson, *Experiments on Pool Boiling Heat Transfer*, Int. J. Heat Mass Transfer 5, 985-999 (1962).
7. A. E. Bergles and W. M. Rohsenow, *The Determination of Forced-convection Surface-boiling Heat Transfer*, Trans. ASME, Paper No. 63-HT-22 (1963).
8. R. B. Bird, W. E. Stewart, and E. N. Lightfoot, *Transport Phenomena*, John Wiley and Sons, Inc., New York, N. Y., p. 41 (1960).
9. D. B. Bukur and H. S. Isbin, *Numerical Solution of the Yamanouchi Model for Core Spray Cooling*, Nucl. Eng. Design 23, 195-197 (1972).
10. F. F. Cadek, D. P. Dominicis, and R. H. Leyse, *PWR FLECHT Final Report*, WCAP 7665 (1971).
11. Y. P. Chang, *An Analysis of the Critical Conditions and Burnout in Boiling Heat Transfer*, TID-14004 (1961).
12. K. R. Chun and R. A. Seban, *Heat Transfer to Evaporating Liquid Films*, Trans. ASME 93, 391 (Nov 1971).
13. M. T. Cichelli and C. F. Bonilla, Trans. Am. Inst. Chem. Eng. 41, 755 (1945).
14. J. G. Collier, *Convective Boiling and Condensation*, McGraw-Hill Book Company, New York, N. Y., p. 238 (1972).
15. Commonwealth Edison, *Final Safety Analysis Report*, Volume VI, Quad-Cities Unit Number I, Docket 50-254 (1970).
16. Commonwealth Edison, *Final Safety Analysis Report*, Volume VI, Zion Station, Docket 50-295-21 (1970).
17. W. B. Cottrell, *Plant Safety Features: The ECCS Rule-making Hearing*, Nucl. Safety 15, 30 (1974).
18. R. B. Duffey and D. T. C. Porthouse, *The Physics of Rewetting in Water Reactor Emergency Core Cooling*, Nucl. Eng. Design 25, 379-394 (1973).
19. R. B. Duffey and D. T. C. Porthouse, *Experiments on the Cooling of High Temperature Surfaces by Water Jets and Drops*, Crest Specialist Meeting on ECCS for LWR, Munich, Paper II-2 (Oct 1972).
20. J. D. Duncan and J. E. Leonard, *Heat Transfer in a Simulated BWR Fuel Bundle Cooled by Spray Under Loss-of-coolant Conditions*, GEAP-13086 (June 1970).

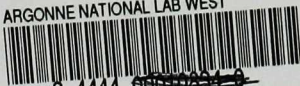
21. J. D. Duncan and J. E. Leonard, *BWR Standby Cooling Heat Transfer Performance Under Simulated Loss-of-coolant Conditions Between 15 and 300 psia*, GEAP-13190 (May 1971).
22. Herbert Bristol Dwight, *Tables of Integrals and Other Mathematical Data*, MacMillan Company, Toronto, Ontario, p. 151 (1961).
23. Kurt Engelberg-Forster and R. Greif, *Heat Transfer to a Boiling Liquid--Mechanism and Correlations*, Trans. ASME, J. Heat Transfer 81, 43-53 (Feb 1959).
24. R. F. Gaertner, *Photographic Study of Nucleate Pool Boiling on a Horizontal Surface*, Trans. ASME, J. Heat Transfer 87, 17-29 (Feb 1965).
25. Peter Griffith, *Bubble Growth Rates in Boiling*, Trans. ASME 80, 721 (1958).
26. D. C. Groeneveld, *Post-Dryout Heat Transfer at Reactor Operating Conditions*, Topical Meeting on Water-reactor Safety, pp. 321-350 (Mar 1973).
27. M. A. Grolmes, G. A. Lambert, and H. K. Fauske, "Flooding in Vertical Tubes," *Multi-phase Flow Systems Symposium*, Inst. Chem. Eng. Symp. Series No. 38 (1974).
28. W. E. Grove, *Brief Numerical Methods*, Prentice-Hall, Inc., Englewood Cliffs, N. J., p. 99 (1966).
29. H. N. Guerrero and P. A. Lowe, *Exploratory Single Tube, Top Flooding, Gravity Feed Heat Transfer Tests*, American Nuclear Society, 20th Annual Meeting, Philadelphia, Pa. (June 23-27, 1974).
30. F. C. Gunther, *Photographic Study of Surface-boiling Heat Transfer to Water with Forced Convection*, Trans. ASME 73, 115-123 (Feb 1951).
31. J. E. Hench, *Consequences of a Steam Line Break in a General Electric Boiling Water Reactor*, NEDO-10045 (July 1969).
32. R. E. Henry, *A Correlation for the Minimum Film Boiling Temperature*, 14th National Heat Transfer Conference, AIChE-ASME, Atlanta, Georgia (Aug 5-8, 1973).
33. G. F. Hewitt and N. S. Hall Taylor, *Annular Two-phase Flow*, Pergamon Press, New York, N. Y., p. 219 (1970).
34. Y. Y. Hsu, *On the Size Range of Active Nucleation Cavities on a Heating Surface*, Trans. ASME, J. Heat Transfer 84, 207 (1962).
35. H. J. Ivey and J. D. Morris, *On the Relevance of the Vapor-liquid Exchange Mechanism for Subcooled Boiling Heat Transfer at High Pressure*, AEEW-R 137 (1962).
36. W. H. Jens and P. A. Lottes, *Analysis of Heat Transfer Burnout, Pressure Drop, and Density Data for High-pressure Water*, ANL-4627 (1951).
37. R. L. Judd and H. Merte, Jr., *Evaluation of Nucleate Boiling Heat Flux Predictions at Varying Levels of Subcooling and Acceleration*, Int. J. Heat and Mass Transfer 15, 1075-1096 (1972).
38. J. H. Keenan and F. G. Keyes, *Thermodynamic Properties of Steam Including Data for the Liquid and Solid Phases*, John Wiley and Sons, Inc., New York, N. Y., p. 76 (1936).
39. F. Kreith, *Principles of Heat Transfer*, International Textbook Company, Scranton, Pa., p. 96 (1966).

40. H. M. Kurihara, Ph.D. thesis, Purdue University, Lafayette, Ind. (1956).
41. S. S. Kutateladze and L. L. Schneidermann, *Experimental Study of the Influence of the Temperature of a Liquid on the Change of the Rate of Boiling*, AEC Translation 3405 (1953).
42. S. Levy, E. Jannen, E. E. Polomik, E. P. Quinn, and F. E. Tippets, "Two-phase Flow Problems," *Proc. Meet. Working Group Heat Transfer*, Brussels (Oct 29-31, 1962).
43. S. Levy, J. Batch, and J. Casterline, "Critical Heat Flux Considerations in the Thermal and Hydraulic Design of Water-cooled Nuclear Reactors," *Proceedings of the Third International Conference on the Peaceful Uses of Atomic Power* 8, 114-125 (1964).
44. S. Levy, *Prediction of the Critical Heat Flux in Forced Convection Flow*, GEAP-3961 (June 20, 1962).
45. S. Levy, *Forced Convection Subcooled Boiling--Prediction of the Vapor Volumetric Fraction*, *Int. J. Heat Mass Transfer* 10, 951-965 (1967).
46. S. Levy, *Generalized Correlation of Boiling Heat Transfer*, *Trans. ASME, J. Heat Transfer* 81, 37-42 (Feb 1959).
47. D. J. Liffengren, *Effects of Cladding Temperature and Material on ECCS Performance*, NEDO-10179 (June 1970).
48. W. H. McAdams, W. E. Kennel, C. S. Minden, Rudolf Carl, P. M. Picornell, and J. E. Dew, *Heat Transfer at High Rates to Water with Surface Boiling*, *Ind. Eng. Chem.* 41, 1945-1955 (Sept 1949).
49. A. F. Mills and D. K. Chung, *Heat Transfer Across Turbulent Falling Films*, *Int. J. Heat Mass Transfer* 16, 694-696 (1973).
50. W. S. Norman and V. McIntyre, *Heat Transfer to a Liquid Film on a Vertical Surface*, *Trans. Ins. Chem. Eng.* 38, 301-307 (1960).
51. S. Nukujama, *Maximum and Minimum Values of Heat Transmitted from Metal to Boiling Water Under Atmospheric Pressure*, *J. Soc. Mech. Eng. Japan* 37(206), 367-374 and 553-554 (1934).
52. W. Nusselt, *Z. Ver. Dtsch Ing.* 54, 1154 (1910).
53. E. F. Obert and R. A. Gaglioli, *Thermodynamics*, McGraw-Hill Book Company, New York, N. Y., p. 73 (1963).
54. H. Ogasawara, S. Kashiwa, M. Naitoh, and A. Yamanouchi, *Cooling Mechanism of the Low-pressure Coolant Injection System of Boiling Water Reactors and Studies of the Loss-of-coolant Accident Phenomena*, *Topical Meeting on Water-reactor Safety*, pp. 351-370 (Mar 1973).
55. W. C. Peterson and M. G. Zaalouk, *Boiling Curve Measurements from a Controlled Heat Transfer Process*, *Trans. ASME, J. Heat Transfer* 93, 401-12 (1971).
56. J. C. Purcupile and S. William Gouse, Jr., *Reynolds Flux Model of Critical Heat Flux in Subcooled Forced Convection Boiling*, *AIChE-ASME Heat Transfer Conference*, Denver, Colorado (Aug 6-9, 1972).
57. A. E. Rogers and J. E. Leonard, *An Analytical Model of the Transient Reactor Core Spray Cooling Process*, *Chem. Eng. Prog. Symp. Series* 67, 14-26 (1971).

58. W. M. Rohsenow, *A Method of Correlating Heat Transfer Data for Surface Boiling of Liquids*, Trans. ASME 74, 338-351 (1952).
59. W. M. Rohsenow and H. Y. Choi, *Heat, Mass, and Momentum Transfer*, Prentice-Hall, Inc., Englewood Cliffs, N. J., p. 148 (1961).
60. W. M. Rohsenow, *Nucleation with Boiling Heat Transfer*, Heat Transfer Division of the American Society of Mechanical Engineers for presentation at the Fluids Engineering, Heat Transfer, and Lubrication Conference, Detroit, Mich., 70-HT-18 (May 24-27, 1970).
61. G. L. Shires, A. R. Pickering, and P. T. Blacker, *Film Cooling of Vertical Fuel Rods*, Reactor Development Division, Atomic Energy Establishment, Winfrith, Dorchester, Dorset AEEW-R-343 (1964).
62. B. J. Stock, *Observations on Transition Boiling Heat Transfer Phenomena*, ANL-6175 (June 1960).
63. K. H. Sun, G. E. Dix, and C. L. Tien, *Cooling of a Very Hot Vertical Surface by a Falling Liquid Film*, Trans. ASME, J. Heat Transfer 96, 126-131 (May 1974).
64. T. S. Thompson, *An Analysis of the Wet-side Heat-transfer Coefficient during Rewetting of a Hot Dry Patch*, Nucl. Eng. Design 22, 212-224 (1972).
65. F. E. Tippets, *Critical Heat Fluxes and Flow Patterns in High-pressure Boiling Water Flows*, Trans. ASME 86, 12-23 (1964).
66. V. I. Tolubinskiy, D. M. Kostanchuk, and Yu N. Ostrovskiy, *Internal Characteristics of the Boiling Process and Rate of Boiling Heat Transfer*, Heat Transfer--Soviet Research 5(2), 92 (Mar-Apr 1973).
67. V. I. Tolubinskiy and D. M. Kostanchuk, *Correlation of Experimental Data on the Rate of Heat Transfer in Boiling of Subcooled Water*, Heat Transfer--Soviet Research 5(3), 82 (May-June 1973).
68. L. S. Tong, *Boiling Heat Transfer and Two-Phase Flow*, John Wiley and Sons, Inc., New York, N. Y., p. 3 (1965).
69. K. Torikai and M. Akiyama, *Analysis of the Second Burnout*, Bull. JSME 13(61), 951-955 (1970).
70. A. M. Trommelen, *Heat Transfer to Falling Liquid Films*, Chem. Eng. Sci. 22, 1152-1154 (1967).
71. *Emergency Core Cooling, Report of Advisory Task Force on Power Reactor Emergency Cooling*, TID-24226 (1967).
72. R. I. Vachon, G. H. Nix, and G. E. Tanger, *Evaluation of Constants for the Rohsenow Pool-boiling Correlation*, Trans. ASME, J. Heat Transfer 90, 239-247 (May 1968).
73. G. C. Vliet and G. Leppert, *Critical Heat Flux for Subcooled Water Flowing Normal to a Cylinder*, Trans. ASME 86, 68 (Feb 1964).
74. J. H. Vohr and T. Chiang, *A Review of the Criteria for Predicting Incipient Nucleation in Liquid Metals and Ordinary Fluids*, MTI-69TR45 (1969).
75. WASH-1400, *An Assessment of Accident Risks in U. S. Commercial Nuclear Power Plants*, (Aug 1974).
76. R. J. Weatherhead, *Nuclear Boiling Characteristics and the Critical Heat Flux Occurrence in Subcooled Axial-flow Water Systems*, ANL-6675 (Mar 1963).

77. R. J. Weatherhead, *Heat Transfer, Flow Instability, and Critical Heat Flux for Water in a Small Tube at 200 psia*, ANL-6715 (June 1963).
78. S. Whitaker, *Effect of Surface Active Agents on the Stability of Falling Liquid Films*, I&EC Fundamentals 3, 132 (1964).
79. W. Wilke, *Wärmeübergang an Rieselfilme*, VDI Forsch Hft, p. 490 (1962).
80. A. Yamanouchi, *Effects of Core Spray Cooling at Stationary State after Loss-of-coolant Accident*, J. Nucl. Sci. Tech. 5, 498-508 (1968).
81. A. Yamanouchi, *Effect of Core Spray Cooling in Transient State after Loss-of-coolant Accident*, J. Nucl. Sci. Tech. 5, 547-558 (1968).
82. K. Yoshioka and S. Hasegawa, *A Correlation in Displacement Velocity of Liquid Film Boundary formed on a Heated Vertical Surface in Emergency Cooling*, J. Nucl. Sci. Tech. 7, 418-425 (1970).
83. K. Yoshioka, S. Matsumoto, and S. Hasegawa, *Displacement Velocity of Calfaction Paint in Emergency Cooling for Reactor Fuel Elements*, Memoirs of the Faculty of Engineering Kyushu University 29(3) (Mar 1970).
84. N. Zuber, *On the Stability of Boiling Heat Transfer*, Trans. ASME, J. Heat Transfer 80, 711 (1958).

ARGONNE NATIONAL LAB WEST



3 4444 00010034 0

